

Surface properties of epitaxially grown crystals

Dissertation zur Erlangung des
naturwissenschaftlichen Doktorgrades
der Bayerischen Julius-Maximilians-Universität
Würzburg

vorgelegt von

Martin Ahr

aus Griesbach i. Rottal

Würzburg 2002

Eingereicht am: 18. April 2002

bei der Fakultät für Physik und Astronomie

1. Gutachter: Privatdozent Dr. Michael Biehl

2. Gutachter: Professor Dr. Wolfgang Kinzel
der Dissertation

1. Prüfer: Privatdozent Dr. Michael Biehl

2. Prüfer: Professor Dr. Eberhard Umbach
der mündlichen Prüfung

Tag der mündlichen Prüfung: 27. Juni 2002

Doktorurkunde ausgehändigt am:

Abstract

In this PhD thesis, we develop models of surfaces of epitaxially grown crystals. In the introductory chapter 1, we introduce the most important physical processes which occur on crystal surfaces in a molecular beam epitaxy (MBE) environment. In the first part of this work (chapters 2–4) we model the (001) surface of the II-VI semiconductors CdTe and ZnSe, our main focus being on CdTe. In the second part (chapters 5 and 6), we study generic features of epitaxial growth which are not specific to one particular material. These are kinetic roughening and the formation of mounds. Both effects can be investigated only after the deposition of a thick film on the substrate. Therefore, we must restrict ourselves to simple models which can be simulated with moderate computational effort.

In chapter 2, we introduce a lattice gas model of flat (001) surfaces of CdTe and ZnSe in thermal equilibrium. Both the arrangement of metal atoms in vacancy structures and the dimerization of nonmetal atoms are considered. The surface is represented by a two-dimensional square lattice. We introduce anisotropic interactions between nearest and next nearest neighbour sites which reflect the known properties of the surface. The phase diagram of this model is determined by means of transfer matrix calculations and Monte Carlo simulations. The phases of the model are identified with different reconstructions which have been observed in experiments. In particular, the transition between a Cd terminated $c(2 \times 2)$ reconstruction at low temperature and a Cd terminated (2×1) reconstruction at high temperature which occurs on the CdTe surface can be explained as an encompassing effect of an order-disorder phase transition. Here, the small energy difference between both reconstructions plays an important role.

Crystal surfaces in an MBE environment are not in thermal equilibrium. Instead, non-equilibrium processes like growth and sublimation occur. Are the essential features of our equilibrium model preserved under these conditions or are there completely different, nonequilibrium effects? To answer this question, we need to extend our two-dimensional lattice gas to a model of a three-dimensional crystal which can be used to simulate growth and sublimation. The basic idea is that there is an isotropic attraction between particles in the bulk of the crystal while particles on the surface interact with the anisotropic interactions of the lattice gas.

Such a model which, however, contains several simplifications compared to a realistic model of CdTe, is investigated in chapter 3. We neglect the dimerization of surface Te atoms and simulate a simple cubic lattice instead of the zinc-blende lattice of CdTe. In spite of these simplifications, many effects which have been observed on sublimating CdTe(001) surfaces in vacuum and under an external flux of pure Cd or pure Te can be reproduced. Additionally, the behaviour of this model agrees qualitatively with that of a simplified version of our lattice gas where the dimerization of Te atoms is neglected. Thus, we have shown that the investigation of two-dimensional lattice gas models in thermal equilibrium is an appropriate tool to obtain insight into the behaviour of reconstructed surfaces in an MBE environment. On the other hand, the non-equilibrium conditions of sublimation induce characteristic deviations from the behaviour of the equilibrium model which should be considered in precise investigations.

Starting from this result, we develop a model of the CdTe(001) surface which is closer to reality. It is introduced in section 4. We simulate a zinc-blende lattice instead of a simple

cubic lattice. However, we still neglect the dimerization of Te atoms. An appropriate choice of the parameter set yields a rough quantitative agreement with experimental results. This indicates, that an extension towards a truly realistic model of CdTe(001) should be possible as soon as experimental data are available which allow for an adaptation of the model. We perform simulations of atomic layer epitaxy (ALE). Although this process is widely used in technological applications and basic research, to our knowledge it has never been investigated by means of Monte Carlo simulations before. We find a growth rate of one half monolayer per cycle and an alternation between a rough and a flat surface in subsequent cycles. Both effects have also been observed in experiments.

In chapter 5, we investigate the fractal properties of kinetically roughened surfaces. We consider a model of an unreconstructed surface of a simple cubic crystal during MBE growth at low temperature. This model yields self-similar, fractal surfaces. We apply the WTMM method to obtain the first complete singularity spectra of such surfaces. The statistical properties of growing surfaces are invariant under dynamic scaling. We identify the dynamic exponent α with the Hölder exponent which maximizes the singularity spectrum. This scaling behaviour is a generalization of the well-known Family-Vicsek scaling. However, we measure a strong dependency of the scaling exponents on the desorption rate which indicates that they are non-universal.

Finally, in chapter 6 we consider the coarsening of mounded surfaces which are created during growth if the diffusion of particles across steps is suppressed by a strong Schwoebel barrier. A continuum model of this process which was studied first by Siegert et. al. predicts a dependency of the dynamic exponents on the symmetry of the surface. To test this prediction, we simulate growth in the presence of an infinite Schwoebel barrier on different lattice structures. We use an efficient simulation algorithm which traces the motion of a single particle from deposition until it has reached a state where it is strongly bound. We find, contrary to the results of the continuum theory, that the scaling exponents are independent of the surface symmetry. Instead, the exponents depend on the speed of the diffusion of particles along step edges. The exponents which are measured in the limit of strong step edge diffusion can be explained by means of a simple consideration.

In the two appendices we explain the techniques which we have used to investigate the models which are considered in this thesis. These are the transfer matrix method and continuous time Monte Carlo simulations.

Zusammenfassung

In dieser Doktorarbeit werden Modelle für die Oberflächen epitaktisch gewachsener Kristalle entwickelt. Im Einleitungskapitel 1 werden die wichtigsten Prozesse auf Kristalloberflächen in einer für die Molekularstrahlepitaxie (MBE) typischen Umgebung vorgestellt. Im ersten Teil der Arbeit (Kapitel 2 – 4) präsentieren wir Modelle für die (001)-Oberflächen der II-VI Halbleiter CdTe und ZnSe. Hauptsächlich beschäftigen wir uns dabei mit CdTe. Im zweiten Teil (Kapitel 5 und 6) werden allgemeine Eigenschaften des Wachstumsprozesses untersucht, die nicht an ein spezielles Material gebunden sind. Dies sind das kinetische Aufräumen wachsender Oberflächen und das Hügelwachstum. Da beide Effekte nur nach dem Aufdampfen dicker Schichten beobachtet werden können, müssen wir uns bei ihrer Untersuchung auf einfache Modelle beschränken, die mit relativ wenig Rechenaufwand simuliert werden können.

In Kapitel 2 stellen wir ein Gittergasmodell für flache CdTe(001)- und ZnSe(001)-Oberflächen im thermischen Gleichgewicht vor. Sowohl die Anordnung der Metallatome in Leerstellenstrukturen als auch die Dimerisierung der Nichtmetallatome werden berücksichtigt. Die Oberfläche wird durch ein zweidimensionales Quadratgitter dargestellt. Wir führen anisotrope Wechselwirkungen zwischen nächsten und übernächsten Nachbarplätzen ein, in denen die bekannten Eigenschaften der Oberfläche berücksichtigt werden. Das Phasendiagramm des Modells wird mit Transfermatrixrechnungen und Monte Carlo Simulationen bestimmt. Die einzelnen Phasen werden mit verschiedenen experimentell untersuchten Rekonstruktionen identifiziert. Insbesondere kann der Übergang von einer Cd-terminierten $c(2 \times 2)$ -Rekonstruktion bei tiefen Temperaturen zu einer ebenfalls Cd-terminierten (2×1) -Rekonstruktion bei hohen Temperaturen, der auf CdTe-Oberflächen beobachtet wurde, als Folge eines Ordnungs-Unordnungs-Phasenübergangs erklärt werden. Dabei spielt der kleine Energieunterschied zwischen den beiden Rekonstruktionen eine wesentliche Rolle.

Kristalloberflächen in einer MBE-Anlage befinden sich nicht im thermischen Gleichgewicht. Stattdessen finden Nichtgleichgewichtsprozesse wie Wachstum und Sublimation statt. Bleiben die wesentlichen Eigenschaften unseres Gleichgewichtsmodells unter diesen Bedingungen erhalten oder treten vollkommen neue Effekte auf? Um diese Frage zu beantworten, müssen wir unser zweidimensionales Gittergas zu einem Modell eines dreidimensionalen Kristalls erweitern, mit dem Wachstum und Sublimation simuliert werden können. Die grundlegende Idee dabei ist, dass sich Atome im Inneren des Kristalls isotrop anziehen, während zwischen Teilchen an der Oberfläche die anisotropen Wechselwirkungen des Gittergases wirken.

Ein solches Modell, das im Vergleich zu einer realistischen Simulation des CdTe allerdings stark vereinfacht ist, betrachten wir in Kapitel 3. Wir vernachlässigen die Dimerisierung von Te-Atomen an der Oberfläche und simulieren ein einfach kubisches Gitter anstelle des Zinkblendengitters des CdTe. Trotz dieser Vereinfachungen können mit diesem Modell viele Effekte reproduziert werden, die auf sublimierenden CdTe(001)-Oberflächen im Vakuum und unter einem externen Fluss aus reinem Cd oder reinem Te beobachtet wurden. Weiterhin stimmt das Verhalten des Modells qualitativ mit dem einer vereinfachten Version unseres Gittergases überein, in dem die Dimerisierung von Te-Atomen nicht berücksichtigt wird. Damit ist gezeigt, dass die Untersuchung zweidimensionaler Gittergasmodelle im thermischen Gleichgewicht prinzipiell ein geeignetes Werkzeug zum Verständnis rekonstruierter Oberflächen unter

MBE-Bedingungen ist. Andererseits verursachen die Nichtgleichgewichtsbedingungen der Sublimation aber auch charakteristische Abweichungen vom Verhalten des Gleichgewichtsmodells, die in genauen Untersuchungen berücksichtigt werden sollten.

Ausgehend von diesem Ergebnis entwickeln wir ein realitätsnäheres Modell der CdTe(001)-Oberfläche, das in Kapitel 4 vorgestellt wird. Wir simulieren das Zinkblendengitter anstelle eines einfach kubischen Gitters. Die Dimerisierung von Te-Atomen wird aber weiterhin vernachlässigt. Durch Wahl eines geeigneten Parametersatzes können experimentelle Ergebnisse nicht nur rein qualitativ, sondern auch grob quantitativ reproduziert werden. Das deutet darauf hin, dass eine Erweiterung zu einem wirklich realistischen Modell möglich sein sollte, sobald geeignete experimentelle Daten zur Anpassung vorliegen. Mit diesem Modell werden Simulationen der Atomlagenepitaxie (ALE) durchgeführt. Obwohl dieser Prozess in Technik und Grundlagenforschung häufig angewendet wird, wurde er unseres Wissens nach noch nie in Monte Carlo Simulationen untersucht. Wir beobachten eine Wachstumsrate von einer halben Monolage pro Zyklus und einen Wechsel zwischen rauen und glatten Oberflächen in aufeinanderfolgenden Zyklen. Beide Effekte wurden auch in Experimenten beobachtet.

In Kapitel 5 werden die fraktalen Eigenschaften kinetisch aufgerauter Oberflächen untersucht. Wir betrachten ein Modell einer unrekonstruierten Oberfläche eines einfach kubischen Kristalls während des MBE-Wachstums bei niedriger Temperatur. Dabei entstehen selbstähnliche Oberflächen, deren multifraktale Spektren mit Hilfe der WTMM-Methode erstmals vollständig bestimmt werden konnten. Die statistischen Eigenschaften wachsender Oberflächen sind invariant unter der dynamischen Skalentransformation. Wir identifizieren den dynamischen Exponenten α mit demjenigen Hölder-Exponenten, der das multifraktale Spektrum maximiert. Dieses Skalenverhalten stellt eine Verallgemeinerung der aus der Literatur bekannten Family-Vicsek-Skaleninvarianz dar. Allerdings messen wir eine starke Abhängigkeit der Skalenexponenten von der Desorptionsrate, was darauf hindeutet dass diese nicht universell sind.

Abschließend untersuchen wir in Kapitel 6 die Vergrößerungsdynamik hügeliger Oberflächen, wie sie während des Wachstums entstehen, wenn die Teilchendiffusion über Stufen hinweg durch eine starke Schwöbelbarriere unterdrückt wird. Ein Kontinuumsmodell dieses Vorgangs, das zuerst von Siegert et. al. untersucht wurde, sagt eine Abhängigkeit der dynamischen Skalenexponenten von der Symmetrie der Oberfläche voraus. Um diese Vorhersage zu überprüfen, simulieren wir das Wachstum mit unendlich hoher Schwöbelbarriere auf verschiedenen Gitterstrukturen. Dabei wird ein effizienter Simulationsalgorithmus verwendet, in dem jeweils die Bewegungen eines einzelnen Teilchens von der Deposition bis zum Erreichen eines fest gebundenen Endzustands verfolgt werden. Wir stellen fest, dass die Skalenexponenten, anders als von der Kontinuumstheorie vorhergesagt, nicht von der Oberflächensymmetrie abhängen. Stattdessen beobachten wir eine Abhängigkeit der Exponenten von der Geschwindigkeit der Diffusion entlang von Stufenkanten. Die bei starker Kantendiffusion gemessenen Skalenexponenten können mit einer einfachen Abschätzung erklärt werden.

In den beiden Anhängen werden die Techniken, mit denen die in dieser Arbeit betrachteten Modelle untersucht wurden, also die Transfermatrixmethode und die Monte Carlo Simulation mit kontinuierlicher Zeit, vorgestellt.

Contents

1	The physics of crystal surfaces in an MBE environment	9
1.1	Surface reconstruction	10
1.2	The roughening transition	12
1.3	Strained overlayers	12
1.4	Motion of atoms on crystal surfaces	13
1.4.1	Deposition	14
1.4.2	Diffusion	14
1.4.3	Desorption	16
1.5	Epitaxial crystal growth	16
1.5.1	Kinetic roughening	17
1.5.2	Unstable growth	18
1.5.3	Dynamic scaling	19
1.6	Atomic layer epitaxy	21
1.7	Sublimation	21
2	Flat (001) surfaces of II-VI semiconductors: A lattice gas model	23
2.1	Surface reconstructions of CdTe and ZnSe	24
2.2	The lattice gas model	26
2.2.1	Interactions of atoms and dimers	27
2.2.2	Characterization of the surface configuration	28
2.2.3	Methods of investigation	28
2.2.4	Simplified model without Te dimerization	29
2.2.5	Results of the model with Te dimerization	31
2.3	Comparison with experimental results	38
3	Reconstructions on non-equilibrium crystal surfaces	40
3.1	The model	40
3.2	Characterization of the surface	43
3.3	Layer-by-layer sublimation	43
3.4	Step-flow sublimation	44
3.5	The surface under an external particle flux	48
3.6	Conclusions	50
4	Simulation of CdTe	51
4.1	The zinc-blende lattice	51
4.1.1	Desorption and adsorption	53
4.1.2	Diffusion	53
4.2	The Hamiltonian of the solid-on-solid model	54
4.2.1	The Cd-Te bond	54
4.2.2	Interactions with lateral neighbours	54
4.3	Beyond the solid-on-solid condition	55
4.4	The dynamics of adatoms	58

4.5	Characterization of the surface	59
4.6	Sublimation	60
4.7	Surfaces under an external particle flux	62
4.8	Atomic layer epitaxy	65
4.9	Summary and discussion	68
5	Singularity spectra and dynamic scale invariance of kinetically rough surfaces	70
5.1	Anomalous scaling and multiscaling	71
5.2	The wavelet approach to multifractality	72
5.3	Results	73
5.3.1	Singularity spectra	74
5.3.2	The relation between static and dynamic scaling properties	75
5.4	Conclusions	77
6	The influence of the crystal lattice on coarsening in unstable epitaxial growth	79
6.1	Effective single particle simulations	79
6.2	Surface morphologies	81
6.3	Diffusion currents	84
6.4	Theoretical estimation of scaling exponents	85
6.5	Measurement of scaling exponents	86
6.5.1	The wavelet method	86
6.5.2	Results	87
6.6	Conclusions	89
A	Transfer matrices and finite size scaling	90
A.1	The transfer matrix method	90
A.1.1	Thermal averages	91
A.1.2	The correlation length	92
A.1.3	Symmetries of the Hamiltonian and vanishing matrix elements	93
A.1.4	Application to two-dimensional lattice systems	94
A.2	Finite size scaling	96
A.2.1	Continuous phase transitions	97
A.2.2	First order phase transitions	98
B	Continuous time Monte Carlo simulations	104
B.1	Fundamental algorithms	105
B.2	Application to lattice gases in thermal equilibrium	109
B.3	Application to kinetical Monte Carlo simulations	110

Chapter 1

The physics of crystal surfaces in an MBE environment

In the fabrication of modern semiconductor devices like computer chips or laser diodes one frequently is interested in depositing thin films on a monocrystalline substrate. Important techniques to achieve this goal are molecular beam epitaxy (MBE) and related methods [44]. A sketch of an MBE chamber is shown in figure 1.1. The whole process is performed in ultra high vacuum (UHV) to avoid the intrinsic instabilities of crystal growth in a liquid or gassy medium which result from diffusive and convective processes [82]. Material is evaporated in an effusion cell and creates an atomic or molecular beam which is directed towards the substrate. The mean free path of the particles in the beam is large compared to the distance between the effusion cell and the substrate such that the particles move on straight lines. Thus, the whole surface is exposed to an even material flux. The success of MBE depends on the ability to control the physical processes which occur on the surface of the substrate itself. This might be done e.g. by a regulation of temperature and particle flux.

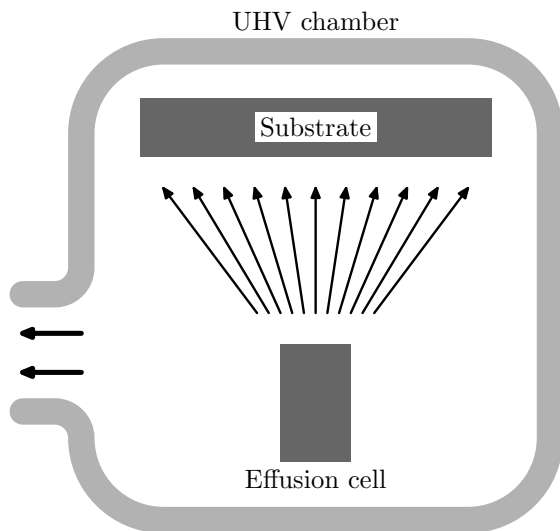


Figure 1.1: Schematical sketch of an MBE growth system. In an UHV chamber, material which is evaporated in an effusion cell creates an atomic or molecular beam. Particles from the beam are attached to the substrate and create a film.

MBE growth leads to the formation of a rich variety of surface morphologies - to the regret of many practicians who are interested in smooth films. From the theoretical point of view, these phenomena pose a challenge to our understanding. First, the physics of crystal surfaces

is determined by a complex interplay of various effects like surface reconstruction and the adsorption, diffusion and desorption of adatoms. Second, a crystal under MBE conditions is in a state far from thermal equilibrium. In this case, no general theoretical framework like equilibrium statistical mechanics is available. Instead, the behaviour of the system might be determined by the details of microscopic processes which occur on atomic lengthscales and short timescales of 10^{-12} s. However, large surface formations like mounds have extensions of up to $1\mu\text{m}$ and their formation takes several minutes to hours. This wide range of relevant length- and timescales has inspired a variety of approaches which range from first principles methods based on quantum mechanics to macroscopic differential equations. In this thesis, we study lattice gas models which build a bridge between a purely microscopic and a purely macroscopic point of view. In contrast to differential equations, they consider the atomistic nature of matter. On the other hand, their conceptual simplicity permits the investigation of large systems on long timescales, which is not possible by means of molecular dynamics or density functional methods. A large fraction of our work is devoted to II-VI semiconductors, in particular CdTe and ZnSe. However, we also investigate more abstract models which aim at an understanding of general, material-independent features.

In the description of a non-equilibrium process like growth or sublimation of a crystal, two different aspects have to be considered. On the one hand, systems which are not in thermal equilibrium tend to approach to it. Therefore, an understanding of the evolution of such a system requires an understanding of its equilibrium configuration. In this thesis, we present the results of models of pure surfaces, i.e. surfaces without adsorbates. Here, we have to consider surface reconstructions and the roughening transition. On the other hand, the way the system evolves depends on the kinetics of processes which occur on the surface like deposition, diffusion and desorption of atoms and molecules.

1.1 Surface reconstruction

In the groundstate, i.e. at temperature $T = 0$, atoms in a crystal arrange in such a way that the energy of the system is minimized. This principle determines the material-specific lattice structure. Atoms at the surface of the crystal have a smaller number of binding partners than atoms in the bulk. Therefore, it is frequently energetically favourable if the surface atoms arrange in a structure which has a lower degree of symmetry than a planar section of the bulk. This phenomenon is called *surface reconstruction*.

Reconstructions have been observed in various materials. In II-VI semiconductors, a variety of reconstructions consisting of vacancy structures, dimers and trimers has been found [21]. These will be discussed in detail in chapters 2–4 where we present models of reconstructed (001) surfaces of CdTe and ZnSe.

In general, a theoretical prediction whether a surface of a particular material reconstructs and which reconstructions can be found is a hard problem even at $T = 0$. It requires an investigation of the properties of the chemical bonds in the crystal. For this purpose, molecular statics using empirical potentials [99] and density functional theory (DFT) [37, 40, 79] have been employed. The computational burden of these methods is comparatively high, which restricts their practical applicability to systems consisting of only a few atoms. Due to the periodicity of crystal surfaces this is not a severe restriction if one is interested in ground state properties.

In the case of polar semiconductors like III-V and II-VI compounds, there is a simple

consideration which allows to *exclude* energetically unfavourable surface configurations [43, 80]. Consider the electronic structure of a compound semiconductor. A schematical sketch of the energy levels in ZnSe is shown in figure 1.2. Other compound semiconductors like GaAs and CdTe show a similar behaviour. From the s - and p -orbitals of the valence electrons sp^3 hybrids are created which have an energy ε_{hyb} . The energy bands of the crystal are obtained from linear combinations of these atomic orbitals. The bonding combinations yield the valence band, the antibonding ones the conduction band. At $T = 0$, the valence band is fully occupied and the conduction band is empty.

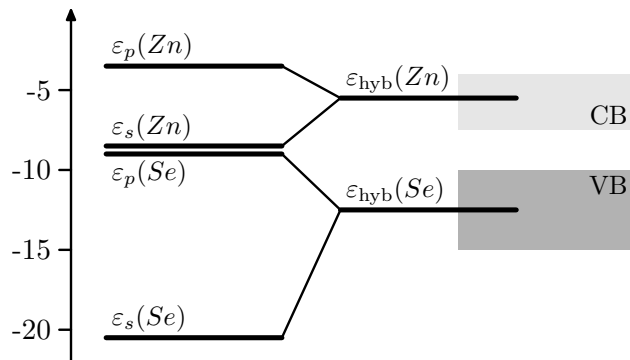


Figure 1.2: Electronic states in ZnSe according to [80]. All energy levels are given in eV. ε_s and ε_p are the energies of the s - and p -orbitals, respectively. These hybridize to form sp^3 orbitals which have an energy ε_{hyb} . The dangling bond energy of anions is inside the valence band, that of cations is in the conduction band.

In the bulk of the crystal, the four sp^3 orbitals of each atom overlap with orbitals of neighbours and create chemical bonds. Each bond is occupied by two electrons. Due to the different electronegativities of the elements the metal atoms carry positive charge (cations) and the atoms of the nonmetallic elements are negatively charged (anions). Atoms at the surface have a smaller number of nearest neighbours such that some of their orbitals are directed out of the crystal. These are denoted as *dangling bonds*. Cation dangling bonds are empty since their energy level is in the conduction band. On the contrary, the binding energy of electrons in the anion dangling bonds is below the valence band maximum such that each of these orbitals is occupied by two electrons. The total charge of each atom is the sum of its valence nuclear charge, the charge of the bonding electrons and the charge of the electrons in the dangling bonds. In general, it is nonzero.

In the majority of all conceivable arrangements of atoms in the terminating layer of the crystal there is a net charge of the surface which creates an electric field in the bulk. Energetically, this is extremely unfavourable [43]. Consequently, in nature only surface reconstructions without a net charge are realized. This condition is fulfilled if the number of electrons is just sufficient to fill the chemical bonds and the anion dangling bonds. In the literature, this law is known as *electron counting rule* [80].

At higher temperature, the properties of the surface are influenced by thermodynamic effects. Frequently, phase transitions between different reconstructions are observed. Strictly speaking, phase transitions exist only in the thermodynamic limit of an infinite number of degrees of freedom. Therefore, their theoretical investigation requires the study of systems with a large number of atoms which is beyond the scope of first principles methods or molecular dynamics simulations using realistic empirical potentials. In this case, effective models which neglect several details but preserve the relevant features of the atomic interactions are required. The models of CdTe and ZnSe which we present in chapters 2–4 belong to this class.

1.2 The roughening transition

In thermal equilibrium at low temperature, surfaces of homogeneous crystals which are oriented in a high symmetry direction are essentially flat apart from the pattern of a possible reconstruction. Since atoms on the surface are bound more weakly than atoms in the bulk, the system minimizes its energy by reducing the area of the surface. The most frequent thermal excitations are single atoms or small groups of atoms diffusing around on the surface and the vacancies they have left when jumping out of the terrace.

The creation of a step of atomic height and length l costs an energy $\varepsilon_{\text{step}}l$. In good approximation, the step energy per unit length $\varepsilon_{\text{step}}$ is independent of temperature. Since atoms at the step edge have a smaller number of binding partners than atoms which are incorporated in a terrace, $\varepsilon_{\text{step}}$ is positive. However, at the creation of the step an entropy $s_{\text{step}}l$ is gained since there are many step configurations with equal energy. Consequently, the free energy per unit length, $\gamma = \varepsilon_{\text{step}} - Ts_{\text{step}}$ decreases with increasing temperature. γ is denoted as *line tension of steps*. At a critical temperature T_R , there is a Kosterlitz-Thouless phase transition [30, 82]. At higher temperature, we have $\gamma = 0$. Then, steps are created spontaneously by thermal fluctuations and the surface becomes rough. This phase transition is called *roughening transition*.

A quantitative measure of the roughness of a surface is the height-height correlation function $G(\vec{l})$. Consider a system of cartesian coordinates (x, y, z) the z -axis of which is perpendicular to the surface. In the remainder of this thesis we will use this orientation of the coordinate system. We define the *height* of the surface $h(\vec{x})$ as function of the vectors \vec{x} in the two-dimensional (x, y) space which returns the z -coordinate of the surface at \vec{x} . Then, $G(\vec{l})$ is defined as

$$G(\vec{l}) := \left\langle \left(h(\vec{x}) - h(\vec{x} + \vec{l}) \right)^2 \right\rangle_{\vec{x}}. \quad (1.1)$$

Below T_R , one finds that $G(\vec{l})$ remains finite in the limit of an infinite distance $|\vec{l}|$. This expresses the fact that the surface is essentially flat. On the contrary, at $T > T_R$ we have $G(\vec{l}) \sim \ln(|\vec{l}|)$. This logarithmic divergence corresponds to a surface with strong fluctuations.

Usually, molecular beam epitaxy is performed at temperatures far below the roughening transition. This is also the case in the growth models which are investigated in this thesis. Consequently, surfaces of homogeneous crystals in thermal equilibrium should be flat at typical MBE temperatures.

1.3 Strained overlayers

In *heteroepitaxy*, the deposited film consists of a different material than the substrate. If substrate and adsorbate have different lattice constants a_s and a_a , equilibrium configurations where the surface is not flat can be found even at low temperature. At the adsorbate-substrate interface, the interaction of the adsorbate particles with the substrate forces the adatoms to adapt to the substrate lattice constant a_s . However, the adatom-adatom interaction favours a distance a_a between adsorbate particles. This induces strain in the adsorbate. The equilibrium configuration depends on the relative strength of the competing forces and the relative lattice mismatch $(a_a - a_s)/a_s$.

Three different growth modes have been observed [82, 86]. If the attraction between adsorbate particles is much stronger than the adsorbate-substrate interaction and/or the

lattice mismatch is large, one obtains small droplets of the adsorbate. This is called the *Volmer-Weber* growth mode. Conversely, if the binding of the adsorbate atoms to the substrate is stronger than the adsorbate-adsorbate bond, small amounts of the adsorbate form a flat layer. The behaviour of a thicker adsorbate layer depends on whether the adsorbate-adsorbate interaction is strong enough to outweigh the elastic energy of the strain. If this is the case, thick layers are flat. This is the *Frank-van der Merwe* mode. Otherwise, in the *Stranski-Krastanov* mode, adsorbate islands are formed on top of a thin wetting layer. In very thick films, dislocations are created. Their creation costs energy, however, they permit the adsorbate to adapt to its own lattice constant a_a . Recently, specialized simulation techniques have been developed which allow for the simulation of strained heteroepitaxial growth [70, 71, 99]. They are computationally expensive, which restricts their practical applicability to 1+1-dimensional models.

In the remainder of this thesis we restrict ourselves to *homoepitaxial* growth where substrate and adsorbate particles are identical.

1.4 Motion of atoms on crystal surfaces

Simulations of surfaces in an MBE environment are based on rules which describe the motion of atoms. In growth models, the atomic nuclei are treated as classical particles the motion of which is, in principle, described by Newton's laws. Of course, the forces which act between the particles are determined by the electronic structure which follows quantum-mechanical laws. In *molecular dynamics* (MD) simulations, the equation of motion of the particles is solved numerically. The forces are calculated by means of empirical potentials or DFT.

In the energy landscape of a large number of atoms in phase space, there are many local minima. These correspond to configurations where the atoms arrange e.g. in a regular crystal lattice. If the heights of the barriers between the minima are noticeably higher than kT , most of the time the actual state of the system will fluctuate around one of them. These are the thermally excited lattice vibrations of the crystal. Very rarely, the system leaves a minimum and jumps into a neighbouring one. These are processes where the arrangement of atoms changes like e.g. a diffusion jump of an adatom on the surface. In a MD simulation, the lattice vibrations are considered explicitly. This is the reason why this method is computationally extremely expensive. On modern computers, the motion of several thousand atoms can be traced for at most some nanoseconds, which is by far too short to investigate MBE.

In Monte Carlo simulations, we investigate the system on a coarse grained scale. Only changes of the arrangement of atoms are considered explicitly, while the chaotic motion of atoms due to lattice vibrations is considered implicitly in a statistical manner. It determines the rate ρ of events where the atomic arrangement changes. One can show quite generally [88] that for thermally excited events ρ is given in good approximation by an Arrhenius law [9]

$$\rho = \nu \exp\left(-\frac{E}{kT}\right). \quad (1.2)$$

E is the height of the energy barrier which must be overcome to change from the initial to the final minimum. ν is an attempt frequency which is on the order of magnitude of the Debye frequency of the crystal. In general, it is reasonable to assume that it is identical for all processes which occur on the surface. Compared to MD, the Monte Carlo technique reduces

the computational effort by many orders of magnitude and makes it feasible to consider the typical timescales of MBE.

Frequently, the position of the atoms in the relevant local energy minima can be assigned to sites in a (potentially distorted) crystal lattice. In this case, *lattice gas* models are appropriate. We consider a fixed crystal lattice. Each lattice site is either occupied by an atom or empty. At the deposition of an atom, the state of one site changes from empty to occupied. If an atom is desorbed, its site is switched from occupied to empty. At the diffusion of an atom, the states of two sites are exchanged. In the presence of surface reconstructions, the topology of the lattice at the surface might be different from that in the bulk. It is possible to extend a lattice gas model to include this effect by adding additional discrete degrees of freedom. Examples are the formation of Si dimers on Si(001) in the simulations of Rockett et. al. [13, 94] and the dimerization of Te atoms in our model of the CdTe(001) surface which will be presented in section 2.

In addition to the application in Monte Carlo simulations, lattice gases and Arrhenius activated processes are the basis of most theories which consider the dynamics of processes which occur at crystal surfaces. Examples include nucleation theory [122, 128] and BCF theory [82, 83].

1.4.1 Deposition

Atoms impinge on the substrate with a kinetic energy $\sim kT_{\text{eff}}$, where T_{eff} is the temperature of the effusion cell. Typically, T_{eff} is higher than the substrate temperature. Additional energy is gained from the formation of chemical bonds to the surface. Consequently, the energy of the newly arriving particles is considerably higher than that of particles on the surface which are already thermalized at substrate temperature. This leads to an increased mobility of adatoms until the excess energy is dissipated. The particles get trapped at energetically favourable sites with high coordination number. Clearly, such sites will be found preferentially in layers close to the substrate. Therefore, the motion of the adatoms is biased in the “downhill” direction. The momentum of the particles in the beam which is directed towards the substrate enhances this bias. In the literature [38, 130] results of molecular dynamics simulations have been reported which confirm these qualitative considerations.

In our simulations, we consider this effect by means of effective rules termed *incorporation* and *downhill funneling*. In incorporation, a particle moves to the lattice site at the lowest height within an *incorporation radius* r_i around the position where it hits the surface [103]. The simulations presented in [38, 130] suggest that reasonable values of r_i should be on the order of magnitude of a few lattice constants. In downhill funneling [32, 33], adatoms perform a biased random walk to nearest neighbour sites lying lower than the current site. The particle stops when the height of all neighbour sites is equal to or greater than the current height.

At the deposition of particles, *precursor states* can play an important role. Particles which land on the surface first enter a state where they are only weakly bound to the surface. Later, a strong chemical bond is formed. Meanwhile, they may diffuse over a considerable distance. In chapter 4, we investigate a model where such weakly bound states play an important role.

1.4.2 Diffusion

To understand the properties of diffusion, the concept of the *potential energy surface* (PES) or *surface energy map* is employed. It is assumed that the energy barriers at zero temperature

are a reasonable approximation for the energy barriers at growth temperature. Consider an atom close to a surface. We fix its position in the x - and y -direction at $\vec{x} = (x, y)$. There is no constraint in the z -coordinate of this test atom and the positions of the atoms in the crystal. We determine the equilibrium configuration at $T = 0$ by minimizing the total energy with respect to these remaining degrees of freedom. Measuring the total energy of the system as a function of \vec{x} , we obtain the PES of an adatom. Local minima of the PES correspond to sites where adatoms are stable with respect to small perturbations e.g. from lattice vibrations.

In the investigation of the hopping of adatoms by means of Monte Carlo simulations, we consider processes where atoms move between these sites. The energy barrier that a single atom must overcome to hop to a neighbouring site equals the difference between the energy of the initial configuration and the saddle point of the PES which lies between the initial and the final site. This information is sufficient to calculate the ratios between the rates of various diffusion processes which occur on the surface from the Arrhenius law (equation 1.2). Interactions between atoms are short-ranged. Consequently, the rates of diffusion processes depend only on the local environment of the diffusing atom within a range of a few lattice constants such that it is sufficient to consider a limited number of typical configurations.

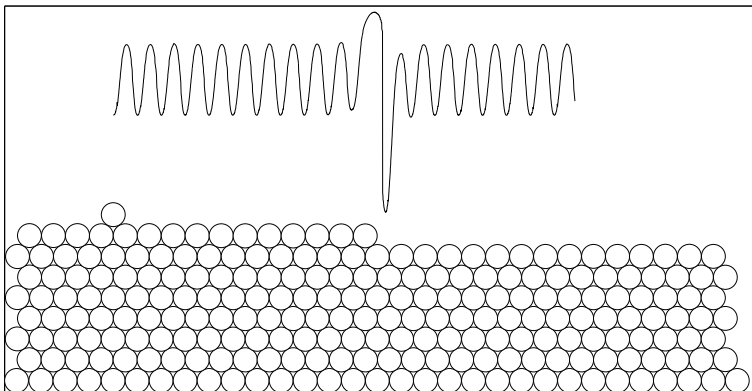


Figure 1.3: Potential energy of a test atom on the surface of a two-dimensional Lennard-Jones crystal at zero temperature as a function of its position. By courtesy of F. Much.

At typical MBE growth temperatures, bulk diffusion can be neglected. The dominant mechanism of material transport is *surface diffusion*. We discuss some important effects in the simplified case of the surface of a two-dimensional crystal of Lennard-Jones particles [70, 71]. This is an example of a system without surface reconstruction. Its PES is shown in figure 1.3. As expected, the potential energy of the test particle has local minima at lattice sites. Therefore, at the deposition of atoms the crystal grows in its own lattice structure such that a lattice gas modelling of this system would be appropriate. At a step edge, where it is surrounded by a large number of neighbours an atom is bound stronger than on a flat surface. Consequently, there is a high energy barrier for the detachment of an atom from the step edge. Similarly, adatoms are bound to other adatoms.

An adatom which crosses a step edge from above must overcome a greater energy barrier than that for diffusion on a flat terrace. This so-called *Schwoebel effect* [106, 107] originates from the fact that a particle at the rim of the step has only a small number of binding partners. Therefore, hopping down a step is suppressed significantly compared to terrace diffusion.

The same effects are found in the physically relevant case of the surface of a three-dimensional crystal. Additionally, we have to consider the diffusion of atoms along step edges. In many materials, *step edge diffusion* at straight steps is as fast as diffusion on a flat

terrace or even faster. Atoms in kinks of an edge have a high coordination number. Consequently, particles get trapped at these *kink sites*. Similar to the Schwoebel effect, energy barriers which suppress step edge diffusion around corners are possible.

In addition to the hopping of atoms, diffusion can take place via exchange processes. An adatom pushes another atom out of the surface and occupies its site. The atom pushed out becomes an adatom at a neighbouring site. From the viewpoint of Monte Carlo simulations of homoepitaxy both processes are equivalent, since initial and final state of hopping and exchange diffusion are identical. However, the energy barriers and therefore the rates of both processes are different. Whether diffusion occurs preferentially via hopping or exchange is material dependent.

The PES of a reconstructed surface has the symmetry of the reconstruction. This may lead to strong anisotropies in the diffusion rates.

In the literature, PES and diffusion barriers for various materials have been published which have been calculated by means of empirical potentials [47, 97, 99, 127] and density functional theory [36, 54, 55, 115]. However, currently no such data are available for the materials which we investigate in this thesis. Therefore, in our models we will use parameterizations of energy barriers which consider the effects which have been discussed in this section.

1.4.3 Desorption

Similar to diffusion, the desorption of atoms from the surface is a thermally activated process the rate of which is given by an Arrhenius law. In general, the higher the coordination number of an atom, the greater is the energy barrier for desorption. Consequently, the desorption of single adatoms which diffuse on a flat terrace occurs at the highest rate, while atoms which are attached to step edges or incorporated in a flat surface are much more stable. In most cases it is reasonable to assume that the energy barrier which must be overcome to remove an atom from the surface equals the difference between the energy of the surface without the adatom and a single atom in vacuum and the energy of the crystal with the adatom at the surface.

1.5 Epitaxial crystal growth

In the following, we measure lengthscales in appropriate units such that the rate at which particles are deposited at one site equals the particle flux F , while diffusion constants of adatoms are identical to hopping rates. This can be done by setting the unit length to a small multiple of the lattice constant of the substrate which depends on the geometry of the crystal lattice. The average time an atom stays on the surface before it is incorporated into the crystal is $1/F$. Diffusion and desorption processes which occur on much longer timescales can be neglected. Typically, this is the case for the detachment of particles from step edges and for the decay of islands which consist of more than i^* atoms. The *critical nucleus size* i^* is small at typical MBE temperatures. Frequently, even pairs of adatoms are stable such that $i^* = 1$. Adatoms which are deposited on the surface diffuse around until they stick to a step edge or collide with more than i^* other adatoms and form a stable island. The latter process is called *nucleation*. Once an island is formed, it captures more and more adatoms and grows. Thereby, the adatom density in the vicinity of the island is reduced which suppresses further nucleation events. Thus, islands keep a typical distance l_i to their neighbours.

Nucleation theory [122, 128] states that the minimal value of l_i which is obtained during the deposition of the first monolayer on a perfectly flat surface has a powerlaw dependence on the ratio of the adatom diffusion constant D and F :

$$l_i \propto \left(\frac{D}{F}\right)^\kappa \quad (1.3)$$

The value of κ depends on various parameters like i^* , the fractal dimension of islands, the mobility of small clusters of adatoms and on whether a significant fraction of adatoms is desorbed. In the simplest case of $i^* = 1$, compact islands and vanishing desorption, we have $\kappa = 1/6$. We refer the reader to refs. [122, 128] for a discussion of this subject. In the late phase of this *submonolayer regime*, neighbouring islands coalesce and l_i increases again.

A perfectly flat surface is never realized in experiments although it is the equilibrium configuration at growth temperature. On the one hand, this is due to the fact that preparation techniques yield an intrinsic surface morphology and thermal smoothing is extremely slow. On the other hand, steps are created during growth by kinetic roughening and the Schwoebel instability which will be discussed in sections 1.5.1 and 1.5.2. As long as the average distance l_s between steps is much greater than l_i , the influence of the steps is weak and growth proceeds essentially the same way as on a flat surface. However, if $l_s \ll l_i$ all adatoms are captured by the steps and no islands nucleate. In this case, growth proceeds in *step flow mode*. The influence of steps on growth can be investigated particularly well on a *vicinal surface* which consists of flat terraces separated by regularly spaced straight steps which are parallel to each other. Experimentally, vicinal surfaces can be created by cleaving a crystal in a small *miscut angle* to a high symmetry surface.

1.5.1 Kinetic roughening

Clearly, the deposition of material on a substrate in an MBE chamber is a stochastic process. Adatoms impinge on random positions. There are random time intervals between successive deposition events at one site. This randomness tends to create rough surfaces with a strongly fluctuating height function $h(\vec{x})$ [112, 113]. On the other hand, diffusion tends to smooth the surface. In the following, we assume that growth starts at time $t = 0$. Since particles diffuse at a finite speed, diffusion can level out fluctuations only at lengthscales smaller than the *correlation length* $\xi(t)$ which increases with time. Properties of regions which are separated by a greater distance are uncorrelated. In particular, there is a random height difference between points at great distance. Consequently, growing surfaces are always rough at large lengthscales. This phenomenon is denoted as *kinetic roughening*, since it is induced by the kinetics of diffusing adatoms. In contrast to the roughening of surfaces in thermal equilibrium which occurs at high temperature, kinetic roughening is most effective at low temperature where diffusion is slow.

The appearance of growing surfaces on small lengthscales depends on the properties of the diffusion process. In the *absence* of a Schwoebel barrier, surfaces with fractal properties can be found. In the modelling of these surfaces, frequently the concept of statistically *self-affine* surfaces is employed [12]. Mathematically, a self-affine surface is defined as a single-valued height function $h(\vec{x})$ the properties of which are invariant under a simultaneous rescaling $\vec{x} \rightarrow b\vec{x}$ and $h \rightarrow h_b(h)$ [105]. Here, b is an arbitrary real number. Clearly, an iterated transformation of the rescaled system with a scaling factor b' should yield the same result as a rescaling of the original system with a factor bb' . This *group property* implies that

$h_{b'}(h_b(h)) = h_{bb'}(h)$, which is fulfilled for $h_b(h) = b^H h$. Thus, the general form of the scale transformation is

$$\vec{x} \rightarrow b\vec{x}; \quad h \rightarrow b^H h. \quad (1.4)$$

The exponent H is denoted as *Hurst exponent*. In the special case $H = 1$, the surface is invariant under an isotropic rescaling of lateral extension and height. This property is denoted as *self-similarity*.

In *statistically self-affine* surfaces, invariance under rescaling is not fulfilled for $h(\vec{x})$ itself. Instead, we assume that there is a stochastic process which creates surfaces such that scale invariance is fulfilled for measurements averaged over an ensemble of independent realizations.

Scale invariance implies conditions for the functional form of various quantities which can be used to measure the Hurst exponent. If \vec{x} is scaled by a factor b , the height-height correlation $G(\vec{l})$ which was defined in equation 1.1 behaves like the square of the surface height such that $G(b\vec{l}) = b^{2H} G(\vec{l})$. This is fulfilled if and only if

$$G(\vec{l}) = g\left(\frac{\vec{l}}{l}\right) l^{2H} \quad (1.5)$$

where we have introduced $l = |\vec{l}|$. Additionally, we consider the standard deviation of the surface height in a square of size $L \times L$,

$$w(L) = \left[\frac{1}{L^2} \int_0^L dx \int_0^L dy (h(\vec{x}) - \langle h(\vec{x}) \rangle)^2 \right]^{\frac{1}{2}}. \quad (1.6)$$

Under the scale transformation 1.4, a square of size L is transformed into a square of size bL . $w(L)$ scales like the height function such that $w(bL) = b^H w(L)$, which implies

$$w(L) = w_0 L^H. \quad (1.7)$$

Physical crystal surfaces are never statistically self-affine in the strict mathematical sense. First, there cannot be any structures which are smaller than the lattice constant a . This *lower cutoff* implies that invariance under the transformation 1.4 breaks down for too large b . Additionally, there is an *upper cutoff* due to the finite correlation length $\xi(t)$. At greater lengthscales, surface heights are uncorrelated which implies that $w(L) = w_\infty = \text{const.}$ for $L \gg \xi(t)$ and $G(\vec{l}) = 2w_\infty^2$ for $l \gg \xi(t)$. However, at late time where $\xi(t)$ is large, in several growth models there is a wide range of lengthscales $a \ll l, L \ll \xi(t)$ where equations 1.5 and 1.7 are fulfilled in good approximation. Surfaces with these properties are denoted as *physical fractals*. However, to fulfil symmetry properties like equation 1.4, the mean surface height must be subtracted. Therefore, we consider the *reduced surface height* $f(\vec{x}) := h(\vec{x}) - \langle h(\vec{x}) \rangle$ instead of $h(\vec{x})$ itself in the investigation of symmetry properties of growing surfaces.

Careful investigations have shown, that some growth models yield surfaces with more complicated fractal properties which are denoted as *multifractal* [11, 23, 24, 57]. In chapter 5, we will investigate such a model.

1.5.2 Unstable growth

On materials with a Schwoebel barrier, epitaxially grown surfaces have a mounded morphology. In the submonolayer regime, islands are formed at a typical distance l_i . Adatoms which

land on top of one of these islands diffuse around. Due to the Schwoebel barrier there is only a small probability that they cross the island edge and are incorporated in the layer below. Instead, they stay on top of the island until they either desorb or meet other adatoms and nucleate. This process creates islands in the second layer before the first layer is completed. Then, islands in the third layer nucleate on top of these islands and so on. Thus, in the course of time mounds build up. Their initial perimeter equals the distance between islands in the submonolayer regime.

At the flank of a mound, there is a train of steps similar to a vicinal surface. Adatoms which approach a step edge from below are captured by the step. The attachment of atoms to steps from above is hindered by the Schwoebel effect. Nucleation on terraces can be neglected since the terrace width is necessarily smaller than l_i . Thus, the majority of the adatoms on a terrace is attached to the upper step. This yields a *Schwoebel current* in the uphill direction which tends to further increase the slope. However, processes like incorporation and downhill funneling keep the mounds from steepening infinitely. In these nonthermal processes, adatoms which impinge close to a step edge move in the downhill direction. This downhill current compensates the Schwoebel current at a *magic slope* m_0 at which the steepening of mounds stops. Frequently, neighbouring mounds coalesce such that the average perimeter of the mounds increases with time. This process is denoted as *coarsening*.

We consider the initial phase of mound formation where the slope m is much smaller than m_0 in the case $l_i \gg 1$. Then, there are large terraces such that the influence of incorporation or downhill funneling can be neglected. In a simplifying manner we assume that the Schwoebel barrier is infinite such that there is no interlayer diffusion. In the first layer, $F\sigma$ particles per unit time and unit area are deposited, where σ is the fraction of the substrate which is not covered by the adsorbate. These particles cover the substrate such that

$$\frac{d\sigma}{dt} = -F\sigma \implies \sigma(t) = \exp(-Ft). \quad (1.8)$$

Consequently, the first layer is not completed as long as $m \ll m_0$. This is the so-called *Zeno effect* [31]. The mounds are separated by deep grooves and there is no coarsening. In case of a finite Schwoebel barrier, there is an initial coarsening regime. However, coarsening stops at a critical mound size and deep grooves between the mounds are formed. Such a behaviour was predicted from continuous differential equations [85, 87] and Monte Carlo simulations [25, 48]. Experimentally, it has been observed in homoepitaxial growth on Pt(111) [48].

When m approaches m_0 , incorporation processes become important. Then, the grooves are filled up and the flanks of the mounds assume their stable slope. Simultaneously, coarsening starts. In chapter 6, we will investigate this process.

1.5.3 Dynamic scaling

In the investigation of crystal growth, one frequently finds that surface snapshots are similar to rescaled surface snapshots taken at different time. In the growth of fractal surfaces, the correlation length $\xi(t)$ increases with time while the fractal properties do not change (figure 5.1). In the coarsening process of mounded surfaces, the size of the mounds grows but their shape remains the same (figure 6.1). Therefore, it is plausible to assume that the statistical properties of the surface are invariant under a simultaneous transformation of spatial extension \vec{x} , time t and the reduced surface height $f(\vec{x}, t)$ [12]:

$$\vec{x} \rightarrow b\vec{x}; \quad t \rightarrow b^z t; \quad f \rightarrow b^\alpha f. \quad (1.9)$$

The powerlaw dependence of the scaling factors for t and f on b is due to the group property of the transformation. This symmetry property is denoted as *dynamic scaling*. It is *independent* of the scale invariance 1.4 of self-affine surfaces. In many models of growth on an initially flat surface, it is valid after a transient phase like e.g. the initial formation of mounds in unstable growth. It is widely believed that the dynamic exponents α and z are *universal*. That means, that α and z are independent of “details” of the model, in particular the numerical values of parameters. Then, the values of α and z determine the *universality class* of a model.

Dynamic scaling implies conditions for the time dependence of the *surface width* $W(t) := \sqrt{\langle f(\vec{x}, t)^2 \rangle}$ and the correlation length $\xi(t)$. Under the transformation 1.9, the correlation length scales like \vec{x} such that $\xi \rightarrow b\xi$. The surface width scales like f such that $W \rightarrow b^z W$. These conditions are fulfilled if W and ξ have a powerlaw dependence on time:

$$\xi(t) = \xi_0 t^{\frac{1}{z}} \quad (1.10)$$

$$W(t) = W_0 t^\beta \quad \text{where } \beta = \frac{\alpha}{z}. \quad (1.11)$$

Similarly, on mounded surfaces the average perimeter of the mounds increases $\propto t^{1/z}$, while their height is $\propto t^\beta$. If the growth process selects one particular slope m_0 , the ratio of height and perimeter of the mounds is constant, which implies $1/z = \beta = \alpha/z \Rightarrow \alpha = 1$.

Additionally, there are conditions for the functional form of the height-height correlation. Since dynamic scaling links properties of the surface at different times, we will use the notation $G(\vec{l}, t)$ for the height-height correlation at time t in the following. Since $G(\vec{l}, t)$ scales like the square of f , we have $G(b\vec{l}, b^z t) = b^{2\alpha} G(\vec{l}, t)$. This is fulfilled if

$$G(\vec{l}, t) = l^{2\alpha} u\left(\frac{\vec{l}}{t^{1/z}}\right). \quad (1.12)$$

Since surface heights at distances greater than $\xi(t)$ are uncorrelated, $G(\vec{l}, t)$ saturates at large distance l . Consequently, $u(\vec{x}) \sim |\vec{x}|^{-2\alpha}$ for large $|\vec{x}|$.

Similarly, the standard deviation $w(L, t)$ of $f(\vec{x}, t)$ in a square of size $L \times L$ must fulfil

$$w(L, t) = L^\alpha v\left(\frac{t}{L^z}\right). \quad (1.13)$$

For small t and large L where $\xi(t) \ll L$, the finiteness of L is irrelevant such that $w(L, t) = W(t)$. This implies that $v(x) \sim x^\beta$ for small x . On the other hand, for $\xi(t) \gg L$, we expect $w(L, t)$ to saturate such that $v(x) \sim \text{const.}$ for large x . Then, $w(L, t)$ assumes an asymptotic value

$$w_{\text{late}}(L) \propto L^\alpha. \quad (1.14)$$

In Monte Carlo simulations, only systems of finite size can be considered. In a square system of size $N \times N$, the deviations from the physically relevant case of an infinite system are small as long as $\xi(t) \ll N$. As soon as the correlation length is comparable to N , finite size effects become relevant. In general, the properties of a finite system are similar to those of a section of an infinite system. Thus, the surface width of a finite system resembles the properties of $w(N, t)$.

So far, no assumptions on the morphology of the surface have been made. If we assume that the surface has self-affine properties on lengthscales smaller than $\xi(t)$, additional conclusions on the scaling behaviour can be drawn. Comparing equations 1.7 and 1.14, we find that the

exponent α and the Hurst exponent H must be identical. Additionally, from equation 1.5 we expect the height-height correlation $G(\vec{l}, t)$ to increase $\sim l^{2\alpha}$ for small l . Consequently, we have $u(\vec{x}) \sim \text{const.}$ for small $|\vec{x}|$. In the literature, the dynamic scaling properties of self-affine surfaces are known as *Family-Vicsek scaling* [34]. For historical reasons, deviations from this behaviour are denoted as *anomalous scaling* [60, 62, 63, 91].

1.6 Atomic layer epitaxy

Kinetic roughening and unstable growth make it difficult to grow perfectly flat layers by means of MBE. There is an alternative called *atomic layer epitaxy* (ALE) which, however, requires specific material properties [44]. ALE works for a binary compound AB which consists of alternating layers of A and B atoms which are parallel to the surface. The chemical bond between A and B atoms must be considerably stronger than A - A and B - B bonds. These conditions are fulfilled e.g. for (001) surfaces of II-VI semiconductors.

In contrast to MBE of a compound material where the constituents are deposited simultaneously, in ALE the surface is exposed to alternating pulses of pure A and B . Between the A and B phases, there is a *dead time* t_d without any particle flux. We start with the deposition of A on a flat B -terminated substrate. Particle flux F and pulse time t_p are chosen such that the amount of deposited material is sufficient for more than one layer of A . A -atoms in the first layer are bound via the strong A - B bond. Atoms in the second or a higher layer have only weak A - A bonds. Temperature and dead time are chosen such that these surplus particles desorb, while atoms bound to the substrate remain on the surface. Since the rate at which atoms with A - B bonds desorb is much smaller than the desorption rate of atoms with A - A bonds only, no fine-tuning of the parameters F , t_p and t_d is required for that purpose. Instead, we obtain the deposition of exactly one layer of A in a self-regulated manner. In the following B -phase and the subsequent dead time, the same process repeats with the roles of A and B interchanged. At the end of the cycle, one monolayer of AB has been deposited. The whole procedure may be repeated an arbitrary number of times to obtain a film of the desired thickness.

This behaviour might be complicated by the presence of surface reconstructions. In many compound semiconductors a surface terminated with a complete layer of one particle species is unstable. In particular, cation terminated surfaces of II-VI semiconductors like CdTe are characterized by vacancy structures with submonolayer coverage. Such effects may lead to ALE growth at rates $\neq 1$ ML/cycle. This feature has been used to investigate the stoichiometry of CdTe(001) and ZnTe(001) surfaces in experiments [27, 35, 123]. In chapter 4, we will simulate ALE of reconstructed surfaces within the framework of our model of CdTe.

1.7 Sublimation

Occasionally, atoms at the surface of a crystal desorb. At a solid in thermal equilibrium with its vapour, this loss of material is compensated by the adsorption of an equal number of particles. In ultra high vacuum, this is not the case such that the crystal shrinks in the course of time. This non-equilibrium process is denoted as *sublimation*.

The *sublimation rate* r_{sub} is defined as the number of monolayers which desorb per unit time. If r_{sub} is measured as a function of T , one finds that in a wide temperature range $r_{\text{sub}}(T)$ is described well by an Arrhenius law (equation 1.2) with attempt frequency ν_{sub} and

activation energy E_{sub} . Monte Carlo simulations [100, 102] have shown, that the *macroscopic* parameters ν_{sub} and E_{sub} are not equal to the corresponding parameters of some rate limiting *microscopic* process like e.g. the desorption of a single adatom. Instead, they are functions of all model parameters. Consequently, to understand sublimation we have to consider the interplay of various physical processes on the surface similar to the investigation of crystal growth.

At moderate temperature, the desorption rate of atoms bound to steps and islands can be neglected compared to that of single adatoms. Adatoms diffuse over a typical distance l_{des} , the *desorption length* before they are desorbed. An adatom is created when an atom detaches from a step edge or when an atom jumps out of a closed layer. In general, the activation energy of the first process is smaller. At the latter process, a vacancy is created simultaneously. An atom at a neighbouring site in the same layer which diffuses into the vacancy leaves a new vacancy behind at the site where it came from. Conversely, one might say that the original vacancy has moved. Therefore, this process is called *vacancy diffusion*.

Vacancies diffuse around until they are either filled by an adatom, are captured by a step edge or meet other vacancies and nucleate a *vacancy island*. This is a hole in the terminating layer of the crystal which exceeds some critical size such that it is unlikely to be closed again. Similar to the typical island distance l_i in submonolayer growth, in the sublimation of a flat surface there is a typical distance l_v between neighbouring vacancy islands. Vacancy islands grow as they capture vacancies diffusing around and adatoms detach from their edges and desorb. Finally, they coalesce with their neighbours and one layer of the crystal is gone. This process is denoted as *layer-by-layer* sublimation.

Similar to crystal growth, sublimation is influenced strongly by the presence of steps on a vicinal surface. If the terrace width l_s is smaller than l_v , the creation of vacancy islands is unlikely since vacancies are captured by the steps. Instead, sublimation proceeds in *step-flow* mode where the steps move back at a speed v_{step} . At the desorption of one monolayer, the steps move over a distance l_s such that $r_{\text{sub}} = v_{\text{step}}/l_s$. Pimpinelli and Villain [83] have investigated step-flow sublimation by means of BCF theory.

If the spacing between steps is large compared to the desorption length, it is unlikely that an adatom which detaches from a step reaches a neighbouring step. Consequently, the interaction between steps is weak and v_{step} is independent of l_s . This case is denoted as *free step-flow*. In *hindered step-flow*, we have $l_s < l_{\text{des}}$. Then, there is a high probability that adatoms which detach from a step are captured by another step instead of being desorbed. Consequently, at small interstep spacing, v_{step} decreases if l_s is reduced.

Vicinal surfaces where the width of all terraces is equal sublimate either in layer-by-layer mode or in step-flow mode. However, techniques of surface preparation frequently yield a wide distribution of terrace widths. In this case, there might be a temperature range where l_v is greater than the width of small terraces, but there are also large terraces which are wider than l_v . Then, small terraces sublimate in step-flow mode. Simultaneously, there is layer-by-layer sublimation on large terraces. This effect has been observed experimentally on (001) surfaces of CdTe [73].

In general, E_{sub} depends on the mode of sublimation. Additionally, different surface reconstructions yield different values of E_{sub} . This problem will be addressed in chapters 3 and 4.

Chapter 2

Flat (001) surfaces of II-VI semiconductors: A lattice gas model

Within the last years, potential technological applications of electronic devices based on II-VI semiconductors [116] have inspired basic research concerning surfaces of these materials. In this context, various studies have addressed the properties of surface reconstructions. Experimental studies have investigated which reconstructions are present [74, 75, 119] and how the reconstruction of the surface is influenced by parameters like temperature and particle flux in an MBE environment [27, 123, 129]. The majority of this work has been devoted to CdTe and ZnSe, where a fairly complete qualitative overview over the phase diagram has been gained. An overview over the properties of CdTe can be found in [21]. On the other hand, there have been theoretical investigations of the reconstructions of CdTe [40] and ZnSe [37, 39, 79] using density functional theory. In these studies, knowledge about the chemical bonding of surface atoms and ground state energies of various reconstructions has been gained.

In this and the following two chapters, we present models which aim at a theoretical understanding of the reconstructed (001) surface of CdTe and ZnSe under typical MBE conditions. As explained in section 1.1, to study thermodynamic effects like phase transitions we need to consider systems with a large number of atoms. On the other hand, the numerical effort should not exceed the capabilities of today's computers. Therefore, efficient representations of atomic interactions are required. In many cases, two-dimensional lattice gases have been used successfully to model atoms adsorbed on a singular crystal surface or the terminating layer of such a crystal [16, 52, 59, 98]. In spite of the conceptual simplicity of such models the interplay of attractive and repulsive short range interactions can result in highly nontrivial critical behaviour and complex phase diagrams. In this chapter, we will follow this approach to model flat (001) surfaces of CdTe and ZnSe in thermal equilibrium, our main focus being on CdTe. In the following two chapters, we will extend this model to consider three-dimensional crystals in nonequilibrium situations like growth and sublimation.

The outline of this chapter is as follows: In section 2.1, we review the known facts about (001) surfaces of CdTe and ZnSe. In section 2.2, we introduce a lattice gas model which considers the occupation of Cd sites and the dimerization of Te atoms and discuss its phase diagram. We conclude with a comparison of the features of our model with experimental results in section 2.3.

2.1 Surface reconstructions of CdTe and ZnSe

Both CdTe and ZnSe crystallize in the zinc-blende lattice. A sketch of the unit cell is shown in figure 2.1. This lattice is equivalent to a diamond lattice apart from the fact that the lattice sites are occupied alternately with the two elements. Each atom is surrounded by four nearest neighbours of the other species the nuclei of which lie on a tetrahedron. The zinc-blende lattice can be decomposed into two intersecting fcc lattices the sites of which are occupied with particles of one species. Thus, it is composed of alternating half-layers of metal atoms (cations) and nonmetal atoms (anions) which are parallel to the (001) surface. Consequently, an ideal (001) surface would be terminated by a complete layer of one particle species. The positions of the atoms in one layer lie on a regular square lattice the axes of which are oriented in the $[110]$ direction and the $[\bar{1}\bar{1}0]$ direction. The lattice constant of this square lattice is $a/\sqrt{2}$, where a is the lattice constant of the zinc-blende lattice itself.

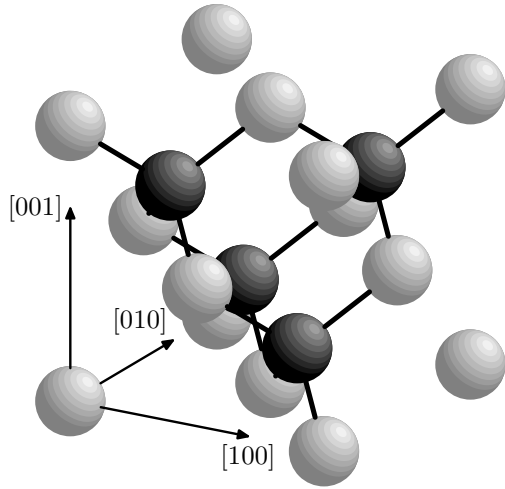


Figure 2.1: Unit cell of the zinc-blende lattice. Anions are shown in light grey, cations in dark grey.

The orientation of the bonds of the atoms in one layer breaks the four-fold symmetry of the surface. Each surface atom is bound to two atoms of the opposite species in the half-layer below. In cations, these bonds point in the $[\bar{1}\bar{1}0]$ direction. Conversely, surface anions have bonds in the $[110]$ direction. Therefore, the symmetry of the (001) surface of the zinc-blende lattice is two-fold.

The stability of the surface reconstructions can be understood from the electron counting rule [43, 80] which was introduced in section 1.1. Each metal atom provides two electrons. In each bond to a bulk atom, $1/2$ electron is engaged. A nonmetal atom brings six electrons, $3/2$ of which are engaged in each bond to an atom in the bulk. The electron counting rule states that the remaining electrons must be sufficient to fill each anion dangling bond and every bond of a surface dimer with two electrons, whereas the cation bonds must remain empty. In particular, a surface terminated with a complete layer of undimerized atoms is unstable.

Under vacuum, the (001) surface of CdTe is Cd terminated. The surface is characterized by vacancy structures where less than one half of the potential Cd sites in the top layer are occupied [27, 123]. At low temperature, one finds a $c(2 \times 2)_{\text{Cd}}$ reconstruction [21, 119], where Cd atoms and vacancies arrange in a checkerboard pattern (figure 2.2a). Frequently, a contribution of a $(2 \times 1)_{\text{Cd}}$ arrangement can be found. In the $(2 \times 1)_{\text{Cd}}$ structure, the Cd atoms arrange in rows along the $[110]$ direction which alternate with rows of vacancies (figure 2.2b). Density functional calculations [40] have shown that the surface energies of the two competing

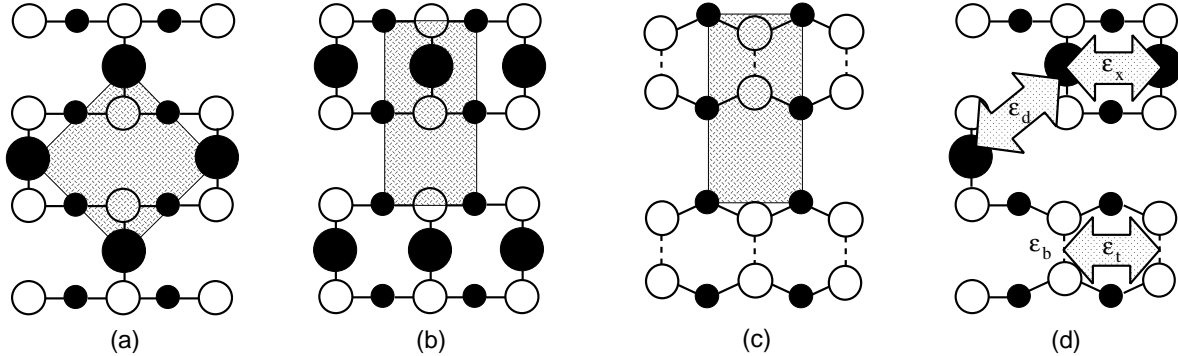


Figure 2.2: Panels (a),(b),(c): Sketches of the reconstructions of CdTe(001) which are discussed in this work. Larger and smaller filled circles denote Cd atoms in the first and third layer, open circles represent Te atoms in the second layer. The grey rectangles show the surface unit cells. The $[110]$ axis is aligned horizontally. (a), (b): Cd terminated reconstructions. Panel (a) shows the $c(2 \times 2)_{\text{Cd}}$ reconstruction, panel (b) the $(2 \times 1)_{\text{Cd}}$ reconstruction. Panel (c) shows the $(2 \times 1)_{\text{Te}}$ reconstruction of surfaces terminated with a complete monolayer of Te. Panel (d) shows the attractive couplings in our model.

reconstructions are nearly degenerate and differ only by a small amount $\Delta E \approx 0.008 \text{ eV}$ per (1×1) surface unit cell¹. At a temperature $T \approx 570 \text{ K}$, there is a phase transition [119] above which the $(2 \times 1)_{\text{Cd}}$ arrangement of the Cd atoms dominates the surface. An analysis of high resolution low energy electron diffraction (HRLEED) peaks [74, 75] has shown, that there is a high degree of disorder in this high temperature phase. One finds elongated domains with a large correlation length of $\approx 375 \text{ \AA}$ in the $[1\bar{1}0]$ direction and a domain width as small as 22 \AA in the $[110]$ direction.

If CdTe is exposed to an external Cd flux in an MBE chamber, the $c(2 \times 2)_{\text{Cd}}$ reconstruction is stabilized at temperatures above the transition in vacuum. Under a Te flux, the surface is Te terminated with a $(2 \times 1)_{\text{Te}}$ reconstruction. At small Te fluxes, the surface is terminated by a complete monolayer of Te. The Te atoms on the surface form dimers which arrange in rows (figure 2.2c). At high Te flux and low temperature, one additional Te atom is incorporated into each dimer, such that the Te coverage of the surface is 1.5. The symmetry of this reconstruction is still (2×1) , since the Te trimers tend to arrange in rows. A schematical phase diagram of the surface following [21] is shown in figure 2.3.

Qualitatively, the properties of the reconstructions of ZnSe [22, 129] are quite similar to those of CdTe, where the Zn atoms are the counterparts of the Cd atoms and the Se atoms those of Te, respectively. There is one important exception: to date, no $(2 \times 1)_{\text{Zn}}$ reconstructed surface has been found at high temperature. Density functional calculations [37, 39, 79] yield a higher energy difference $\Delta E \approx 0.03 \text{ eV}$ per (1×1) surface unit cell between ideal $c(2 \times 2)$ and (2×1) reconstructed surfaces, which is approximately twice the value calculated for CdTe. As we will show, this greater energy difference might explain the different behaviour of CdTe and ZnSe.

¹In [40] a greater value of $\Delta E = 0.016 \text{ eV}$ is given. However, ΔE is rather sensitive to some approximations. We use the unpublished result of a more precise calculation by S. Gundel.

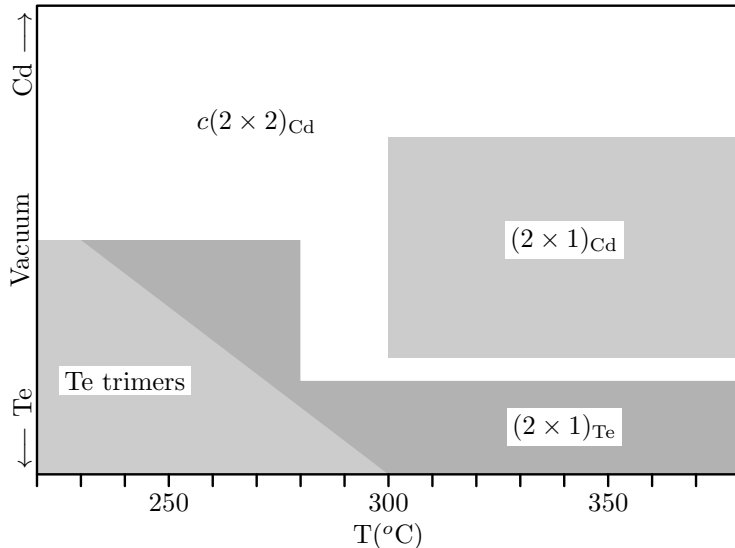


Figure 2.3: Schematic surface phase diagram of CdTe in an MBE environment according to [21]. Shown is the predominant reconstruction as a function of temperature and particle flux. The properties of the surface in vacuum are shown in the middle. The upper part displays the reconstruction under a Cd flux, the lower part shows the features of the surface under a Te flux.

2.2 The lattice gas model

The basic structure of our model of (001) surfaces is the same for different II-VI semiconductors. The differences between the materials are represented by the numerical values of parameters. In the following, for simplicity we will loosely speak of Cd and Te atoms instead of “cations” and “anions” without restricting ourselves to a modelling of CdTe only.

We present a lattice gas model with effective interactions which include effects of surface strain and, at elevated temperature, lattice vibrations. Therefore, there is no simple mapping between ground state energies of the lattice gas model and surface energies determined from density functional theory.

We model a flat (001) surface of CdTe, i.e. we neglect the influence of steps on the reconstruction. This is a reasonable approximation if the typical distance between steps is much greater than the size of the unit cell of the reconstruction. In thermal equilibrium, this is fulfilled at temperatures well below the roughening transition. In this case, in the absence of bulk vacancies or other defects the crystal is uniquely described by the state of the topmost monolayer which consists of one Cd half-layer and a Te half-layer. In our model, we consider such a monolayer with the Cd atoms on top. For simplicity, we assume the Te layer to be fully occupied. This is not a severe restriction, since the removal of Te atoms will uncover Cd atoms in the layer below. Within the limit of a model of a flat surface, we simply do not distinguish whether a Cd terminated surface has been created by removing a Te layer or by depositing additional Cd atoms onto an intact Te layer.

We use cartesian coordinates where the x -axis points in the $[110]$ direction, the y -axis points in the $[1\bar{1}0]$ direction and the z -axis points in the $[001]$ direction. The origin of the coordinate system is at the centre of a Cd atom. Since we consider a flat surface, the z -coordinate of all atoms of one species is identical and will be omitted in the following. Measuring the lattice constant in appropriate units, the Cd atoms are at positions (x, y) with integer x, y . The Te atoms are at positions $(x, y + 1/2)$, where $x, y \in \mathbb{Z}$. Tellurium dimers are created by the formation of a chemical bond between neighbouring Te atoms in y -direction ($[1\bar{1}0]$). Since this is also the direction of the bonds of a surface Cd atom, a Te dimer is formed by a pair of atoms which might also be the binding partners of a Cd atom above them. This suggests a

simple lattice gas representation both of the occupation of Cd sites and Te dimerization: We consider a rectangular array x of integers $\{x_{i,j}\}_{i,j=1}^{L,N}$. $x_{i,j} = 1$ represents a Cd atom at site (i, j) which is bound to the Te atoms at sites $(i, j - 1/2)$ and $(i, j + 1/2)$. $x_{i,j} = 2$ corresponds to a dimerization of Te atoms $(i, j - 1/2)$ and $(i, j + 1/2)$. Otherwise, $x_{i,j} = 0$.

In principle, one might also consider the formation of Te trimers by introducing a fourth state $x_{i,j} = 3$. This corresponds to a trimer which consists of the Te atoms at $(i, j - 1/2)$ and $(i, j + 1/2)$ and an additional Te atom at (i, j) . However, the formation of Te trimers plays a role only if the surface is exposed to a strong flux of pure Te at comparatively low temperature. Therefore, we have neglected this effect to reduce the number of parameters of our model and the numerical effort of its investigation.

2.2.1 Interactions of atoms and dimers

The detailed representation of the surface energies of a II-VI compound certainly would require long-range interactions and terms which depend on the simultaneous occupation of three or more sites. However, it is plausible to assume that the dominant contribution to the surface energy stems from pairwise interactions of atoms at short distances. In this section, we introduce a Hamiltonian which considers pairwise interactions between $x_{i,j}$ on nearest neighbour sites and diagonal neighbour sites. These reflect the known properties of the reconstructions of CdTe and ZnSe.

Due to the electron counting rule, surfaces with Cd coverages greater than $1/2$ are unstable while both a $c(2 \times 2)_{\text{Cd}}$ reconstruction and a $(2 \times 1)_{\text{Cd}}$ reconstruction are permitted. This feature can be captured by introducing a hardcore repulsion between Cd atoms on neighbouring sites in the y -direction. In the x -direction, an attractive interaction favours the occupation of nearest neighbour pairs the strength of which is denoted by $\varepsilon_x < 0$. An attractive interaction $\varepsilon_d < 0$ between diagonal neighbours stabilizes the $c(2 \times 2)_{\text{Cd}}$ reconstruction. The parameters ε_x and ε_d are chosen such that the energy difference $\Delta E = |2\varepsilon_d - \varepsilon_x|/2$ between these two reconstructions is small compared to the total surface energy per site.

The electron counting rule favours Te dimerization, but forbids the formation of additional bonds of dimerized Te atoms. Therefore, we forbid the simultaneous occupation of neighbour sites in the y -direction with dimers (formation of chains of Te-Te-bonds) and Cd atoms next to a dimer. These rules permit both a $(2 \times 1)_{\text{Te}}$ reconstruction, where the dimers arrange in rows and a $c(2 \times 2)_{\text{Te}}$ reconstruction, where they arrange in a checkerboard pattern. Density functional calculations [40] have shown that the surface energy of $(2 \times 1)_{\text{Te}}$ is significantly lower than that of a $c(2 \times 2)_{\text{Te}}$ reconstruction. This may be understood from the more efficient relaxation of surface strain in $(2 \times 1)_{\text{Te}}$: Since the lattice is deformed in the same direction by dimers on neighbouring sites in x -direction, such an arrangement will be energetically favourable. We consider this fact by an attractive nearest neighbour interaction ε_t between dimers in x -direction. Additionally, a dimer contributes a binding energy ε_b to the surface energy. Apart from the hardcore repulsion, we consider no interaction between Cd atoms and dimers. An overview over the couplings in our model can be found in figure 2.2d.

This yields the Hamiltonian

$$H = \sum_{i,j=1}^{L,N} \varepsilon_x c_{i,j} c_{i+1,j} + \varepsilon_d c_{i,j} (c_{i+1,j+1} + c_{i+1,j-1}) + \varepsilon_t d_{i,j} d_{i+1,j} + \varepsilon_b d_{i,j} - \mu c_{i,j}, \quad (2.1)$$

where we have introduced $c_{i,j} = \delta_{x_{i,j},1}$ and $d_{i,j} = \delta_{x_{i,j},2}$. The boundary conditions are assumed to be periodic. $c_{i,j}$ represents the occupation of lattice sites with Cd atoms: $c_{i,j} = 1$ at the

positions of Cd atoms and zero otherwise. Similarly, the positions of dimers are given by $d_{i,j} = 1$. μ is the effective Cadmium chemical potential, which includes the binding energy of surface Cd atoms to the substrate. The groundstate of the system at $T = 0$ is determined by the chemical potential μ . For $\mu > \mu_0 = 2\varepsilon_d - \varepsilon_t - \varepsilon_b$, the surface configuration with minimal energy is $c(2 \times 2)_{\text{Cd}}$. For $\mu < \mu_0$ the groundstate is $(2 \times 1)_{\text{Te}}$.

In the following, we measure energy in dimensionless units which have been adjusted such that $\varepsilon_d = -1$. Additionally, we set Boltzmann's constant $k = 1$ such that temperature is measured in units of $|\varepsilon_d|$.

2.2.2 Characterization of the surface configuration

To characterize the surface reconstruction quantitatively, we evaluate the mean Cd coverage $\rho_{\text{Cd}} = \langle c_{i,j} \rangle_{i,j}$ and the correlations

$$C_{\text{Cd}}^d = \frac{1}{2} \langle c_{i,j} (c_{i+1,j+1} + c_{i+1,j-1}) \rangle_{i,j} \quad (2.2)$$

$$C_{\text{Cd}}^x = \langle c_{i,j} c_{i+1,j} \rangle_{i,j}. \quad (2.3)$$

C_{Cd}^d measures the probability to find two diagonal neighbour sites which are simultaneously occupied by Cd atoms. This is a measure for the fraction of the surface which is covered by regions with a *local* $c(2 \times 2)_{\text{Cd}}$ order. Similarly, C_{Cd}^x measures the contribution of locally $(2 \times 1)_{\text{Cd}}$ reconstructed regions in the system.

The *long range order* of the Cd atoms is measured by the order parameters

$$M_{\text{Cd}}^{(2 \times 2)} = \frac{1}{LN} \sum_{i,j=1}^{L,N} c_{i,j} \cos(\pi(i+j)) \quad (2.4)$$

$$M_{\text{Cd}}^{(2 \times 1)} = \frac{1}{LN} \sum_{i,j=1}^{L,N} c_{i,j} \cos(\pi j). \quad (2.5)$$

$M_{\text{Cd}}^{(2 \times 2)}$ is the staggered magnetization of a system of Ising variables $\{s_{i,j}\}_{i,j=1}^{L,N}$, where $s_{i,j} = 1$ if $c_{i,j} = 1$ and -1 otherwise. Large absolute values indicate a long range order of the $c(2 \times 2)_{\text{Cd}}$ reconstruction. Its counterpart $M_{\text{Cd}}^{(2 \times 1)}$ measures the long range order of $(2 \times 1)_{\text{Cd}}$.

Further, we introduce the mean Tellurium dimerization $\rho_D := \langle d_{i,j} \rangle_{i,j}$ and the dimer correlation $C_D^x := \langle d_{i,j} d_{i+1,j} \rangle_{i,j}$, which characterizes the number of dimers which are incorporated in *locally* (2×1) ordered areas. Their long range order is characterized by

$$M_D^{(2 \times 1)} = \frac{1}{LN} \sum_{i,j=1}^{L,N} d_{i,j} \cos(\pi j). \quad (2.6)$$

2.2.3 Methods of investigation

We have investigated this model by means of the transfer matrix method and Monte Carlo simulations. An introduction to the transfer matrix technique is presented in appendix A. This method allows for a numerical calculation of the free energy of lattice systems with short-range interactions. In general, the system size must be finite in all directions but one. In our investigations, we choose the y -direction as the infinite direction. Since the computational

effort increases exponentially fast with the system size L in the x -direction, only comparatively small L are feasible. However, this is sufficient to investigate the phase transitions of the system in the limit $L \rightarrow \infty$ via finite size scaling techniques. To this end, we have applied the method discussed in section A.2.2 to determine the loci of first order phase transitions and to compute coverage discontinuities. Continuous transitions have been investigated by means of phenomenological renormalization group theory, which will be introduced in section A.2.1. Coverage and correlations can be obtained from proper derivatives of the free energy or directly from the relevant eigenvector of the transfer matrix. We have refrained from calculating order parameters by means of the transfer matrix. This would require the introduction of staggered fields in the Hamiltonian 2.1. A system with this modified energy function is numerically intractable for reasonable values of L .

Additionally, we have performed Monte Carlo simulations of our model. To obtain a reasonably fast equilibration, we have applied continuous time algorithms which will be discussed in more detail in appendix B. We have simulated both the grand-canonical ensemble where ρ_{Cd} is controlled by μ and the canonical ensemble where the number of Cd atoms in the system is fixed. In general, the results of the transfer matrix calculations and the Monte Carlo simulations are in good agreement (figures 2.4 and 2.6).

2.2.4 Simplified model without Te dimerization

In this section we present a simplified version of our model where we do not consider the dimerization of Te atoms, i.e. the possible values of the $x_{i,j}$ are constrained to the values 0 and 1. Then, the state of the system is uniquely described by $\{c_{i,j}\}_{i,j=1}^{L,N}$. The Hamiltonian of the simplified model is

$$H_s = \sum_{i,j=1}^{L,N} \varepsilon_x c_{i,j} c_{i+1,j} + \varepsilon_d c_{i,j} (c_{i+1,j+1} + c_{i+1,j-1}) - \mu c_{i,j}. \quad (2.7)$$

For $\mu > -2$, the groundstate is a $c(2 \times 2)_{Cd}$ reconstruction, whereas for $\mu < -2$, the system is empty at zero temperature. Figure 2.4 shows the temperature dependent behaviour of the correlations and order parameters of this model with the parameter set $\varepsilon_d = -1$, $\varepsilon_x = -1.96$ in the grand canonical ensemble at a chemical potential $\mu = -1.96$. In the Monte Carlo simulations, the system was initialized with a perfect $c(2 \times 2)_{Cd}$ reconstruction at all investigated temperatures. At low temperature, we obtain values of $M_{Cd}^{(2 \times 2)}$ and C_{Cd}^d close to 0.5. C_{Cd}^x is small and $M_{Cd}^{(2 \times 1)}$ is zero apart from small fluctuations which are finite size effects. This is the signature of a long-range ordered $c(2 \times 2)_{Cd}$ reconstructed phase. At $T \approx 0.3$, the system loses its long-range order such that at high temperature we have $M_{Cd}^{(2 \times 2)} \approx M_{Cd}^{(2 \times 1)} \approx 0$. Simultaneously, the Cd coverage jumps to a smaller value. These features indicate a first order transition from the $c(2 \times 2)_{Cd}$ phase at low T to a disordered regime at high temperature.

At the phase transition, C_{Cd}^d decreases rapidly. Conversely, C_{Cd}^x displays a sudden increase such that $C_{Cd}^x > C_{Cd}^d$ in the high temperature regime. Consequently, in the vicinity of the phase transition not only the long range order, but also the *local arrangement* of the Cd atoms changes. In the disordered phase they prefer to arrange in rows which are characteristic of the $(2 \times 1)_{Cd}$ reconstruction.

In figure 2.5, we show phase diagrams of the simplified model at $\varepsilon_x = -1.6$ (figure 2.5a) and $\varepsilon_x = -1.9$ (figure 2.5b) in the ρ_{Cd} - T plane. In addition to the transfer matrix extrapolation,

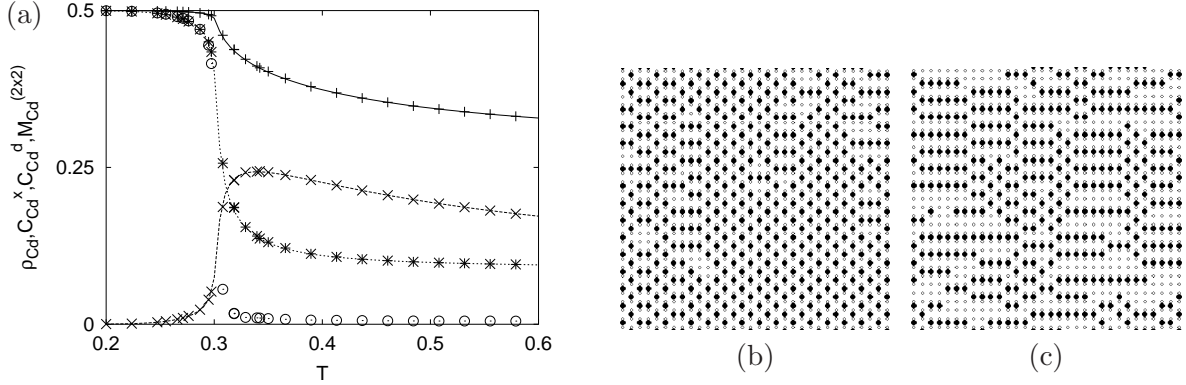


Figure 2.4: Temperature dependent behaviour of the simplified model at $\varepsilon_d = -1$, $\varepsilon_x = \mu = -1.96$. Panel (a): Cd coverage ρ_{Cd} (+), correlations C_{Cd}^x (×), C_{Cd}^d (※) and mean absolute of the order parameter $M_{Cd}^{(2 \times 2)}$ (⊙). The symbols show results of Monte Carlo simulations of a 128×128 system. $10^4 \cdot LN$ events have been performed both for equilibration and for measurement. The lines show results of a transfer matrix calculation at a strip width $L = 18$. Panels (b), (c) show sections of $16\sqrt{2} \times 16\sqrt{2}$ zinc-blende lattice constants of the surface at the end of the simulation run at $T = 0.29$ (b) and $T = 0.33$ (c).

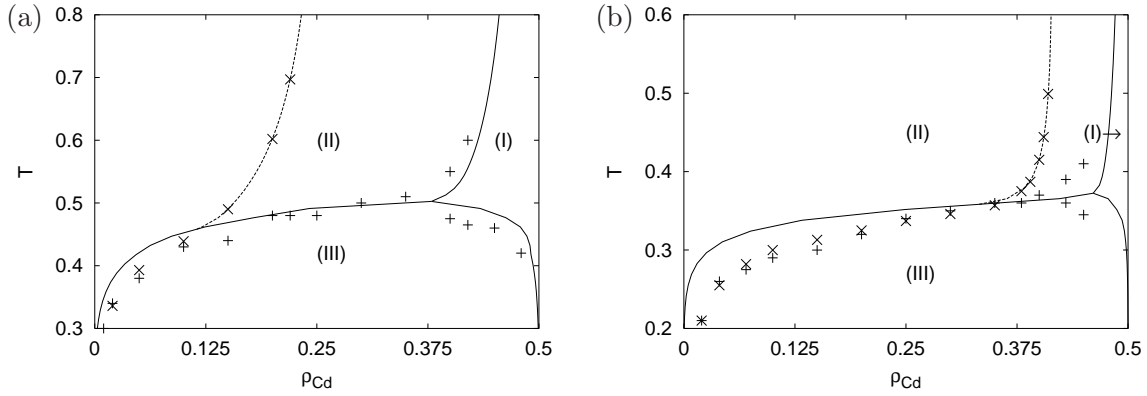


Figure 2.5: Phase diagrams of the simplified model without Te dimerization in the ρ_{Cd} - T plane at $\varepsilon_x = -1.6$ (panel (a)) and $\varepsilon_x = -1.9$ (panel (b)). In both figures we have $\varepsilon_d = -1$. The solid lines show the phase boundaries which have been extrapolated from transfer matrix calculations with strip widths $L = 14, 16$ and 18 . The crosses show results of Monte Carlo simulations of a 128×128 system at fixed ρ_{Cd} . Phase (I) is homogeneously ordered with a $c(2 \times 2)_{Cd}$ reconstruction whereas phase (II) is disorderd. In region (III), phases (I) and (II) coexist. At the dashed line, we have $C_{Cd}^x = C_{Cd}^d$. The symbols (×) show the respective results of the Monte Carlo simulations. Statistical errors of the simulation data are on the order of 0.05.

we obtain a rough estimate of the phase diagram from canonical Monte Carlo simulations at constant Cd coverage². For this purpose, a non-local algorithm which exchanges empty and occupied sites according to Kawasaki rates [76, 126] is applied. A rapid decrease of $M_{Cd}^{(2 \times 2)}$ with T indicates the transition into the disordered phase. A search for a pronounced maximum in the fluctuation of the order parameters yields results which are identical within errorbars. The symbols in figure 2.5 show the results for $N = L = 128$ which are in reasonable agreement with the transfer matrix prediction.

At low temperature and high ρ_{Cd} , the system is in the homogeneously ordered phase (I). The disordered phase (II) is found at extremely low Cd coverage. In the regime (III) at intermediate Cd coverages, the phases (I) and (II) coexist. ρ_{Cd} in both phases is given by the right and the left boundary of region (III), respectively. The coexistence regime (III) disappears at a tricritical point. At high temperature the system is either homogeneously ordered or disordered, depending on coverage. The transition between these regimes is continuous in terms of $M_{Cd}^{(2 \times 2)}$ and should belong to the Ising universality class. Our transfer matrix calculations yield a temperature exponent³ $y_T = 1$ which is consistent with this picture. However, a calculation of the exponent y_h is not possible without the introduction of staggered fields. In the limit $T \rightarrow \infty$, the line of the transition between the phases (I) and (II) approaches the line $\rho_{Cd} = 1/2$. This can be understood from the fact that at very high temperature the infinite repulsion between nearest neighbours in y -direction is the only relevant interaction. Then, columns of lattice sites aligned in y -direction decouple such that the system is disordered at arbitrary ρ_{Cd} . This is in contrast to isotropic hard square lattice gases [14, 51] where an extended regime (I) persists for arbitrary temperature.

To characterize the short range order of the Cd atoms, we have determined the line where $C_{Cd}^x = C_{Cd}^d$. Since this is not a line of phase transition, it is not possible to apply finite size scaling theory to extrapolate its position to the limit of an infinite system. However, the results of transfer matrix calculations for various L and the canonical Monte Carlo simulations at $N = L = 128$ agree well such that finite size effects are probably weak. At the right of the dashed line in figure 2.5, the $c(2 \times 2)_{Cd}$ ordering is prevalent. At smaller ρ_{Cd} , the Cd atoms arrange preferentially in a $(2 \times 1)_{Cd}$ order.

Figure 2.4 demonstrates the crucial role that the difference between the surface energies of perfect $c(2 \times 2)_{Cd}$ and $(2 \times 1)_{Cd}$ reconstructions plays for the phase diagram. With increasing ΔE , the tricritical point shifts to smaller coverage and higher temperature. Even more so does the line which separates $c(2 \times 2)_{Cd}$ from $(2 \times 1)_{Cd}$ prevalence.

2.2.5 Results of the model with Te dimerization

To get insight into the typical behaviour of the model, we will first present a detailed investigation using the parameter set $\varepsilon_d = \varepsilon_b = -1$, $\varepsilon_x = \varepsilon_t = -1.9$. The choice $\varepsilon_x = -1.9$ reflects the fact that the energy difference between $c(2 \times 2)_{Cd}$ and $(2 \times 1)_{Cd}$ is small. The choice $\varepsilon_b = -1$ yields low concentrations of Te atoms which are neither dimerized nor bound to Cd atoms. This is consistent with experimental results. For simplicity, we have chosen $\varepsilon_t = \varepsilon_x$ as a typical example of the case where both couplings are of the same order of magnitude. However, since there is no next-nearest neighbour interaction between dimers, there is a significant difference in the surface energies of $(2 \times 1)_{Te}$ and $c(2 \times 2)_{Te}$, which is consistent with

²These simulations have been performed by T. Volkmann. See [126] for additional information.

³The exponents y_T and y_h are defined in appendix A.2.1.

the results of [40].

Below, we discuss the influence of the numerical values of the parameters on the phase diagram. We will show, that a smaller value of ε_t affects the phase diagram qualitatively. In particular, this concerns the high temperature phases.

Grand-canonical ensemble

With the above parameter set, the Cd and the Te terminated groundstates are separated by $\mu_0 = 0.9$. In figure 2.6 the temperature dependent behaviour of the system at constant chemical potential is shown for $\mu = 1$ (figure 2.6a,b) and $\mu = 0.8$ (figure 2.6c,d), which are examples for both cases. At $\mu = 1$, the ordered $c(2 \times 2)_{\text{Cd}}$ phase at low T manifests itself in a high Cd coverage ρ_{Cd} and values of the correlation C_{Cd}^d and the order parameter $M_{\text{Cd}}^{(2 \times 2)}$ close to 0.5. In figure 2.7d a surface snapshot in this phase at $T = 0.71$ is shown. As expected, the Cd atoms arrange preferentially in a checkerboard configuration. At a temperature $T = 0.83$, there is a first order phase transition to a disordered phase. This is indicated by a decrease of the order parameter $M_{\text{Cd}}^{(2 \times 2)}$ and the correlation C_{Cd}^d . Simultaneously, C_{Cd}^x starts to increase. At $T = 1$, both lines cross such that the high temperature behaviour of the system is dominated by a local (2×1) ordering of the Cd atoms. The simulation data shown in figure 2.6a,b have been taken from two independent simulation runs. The system was initialized with a perfect $c(2 \times 2)_{\text{Cd}}$ configuration at the lowest temperature investigated. Then, as successively higher temperatures were imposed, the surface configuration was kept as initial state of the next simulation. This reflects in a small hysteresis effect in $M_{\text{Cd}}^{(2 \times 2)}$ due to the first order nature of the phase transition. Qualitatively, the behaviour of the Cd atoms is quite similar to that found in the simplified model (figure 2.4).

At $\mu = 0.8$, we obtain a completely different behaviour. Since the groundstate is a $(2 \times 1)_{\text{Te}}$ reconstruction, at small T we measure low Cd coverages and values of C_D^x and $M_D^{(2 \times 1)}$ close to 0.5. The most frequent thermal excitations are Cd adatoms, the density ρ_{Cd} of which increases with T . Figure 2.7c shows a surface snapshot at $T = 0.93$. The Cd atoms preferentially arrange in rows such that $C_{\text{Cd}}^x \gg C_{\text{Cd}}^d$. These rows adapt to the structure of the $(2 \times 1)_{\text{Te}}$ reconstruction. This yields nonzero values of the order parameter $M_{\text{Cd}}^{(2 \times 1)}$, which indicate a global ordering of Cd atoms in a (2×1) arrangement. However, the interactions between the Cd atoms themselves are insufficient to stabilize this global order. Instead, it is purely induced by the environment of the Te dimers.

At $T = 1.23$, there is a first order phase transition above which the system is in a disordered phase similar to that found at $\mu = 1$. Remarkably, we observe high $\rho_{\text{Cd}} \approx 0.2$ at temperatures slightly below the phase transition. At the phase transition, ρ_{Cd} jumps to an even higher value. Above the transition it decreases slightly with T .

Phase diagram

Figure 2.7a,b shows the phase diagram of the model, which has been extrapolated from transfer matrix calculations with strip widths L of 6, 8 and 10. In figure 2.7b, the lines of phase transitions in the μ - T plane have been plotted. At low temperature, the system is either in an ordered $(2 \times 1)_{\text{Te}}$ (1) or an ordered $c(2 \times 2)_{\text{Cd}}$ phase (2). The line of phase transition between these phases starts at zero temperature and $\mu = \mu_0$ where the energies of both reconstructions are degenerate. For $0 < T < T_t = 0.84$, it remains at the same chemical potential μ_0 , apart from small numerical uncertainties of extrapolation. In consequence, a

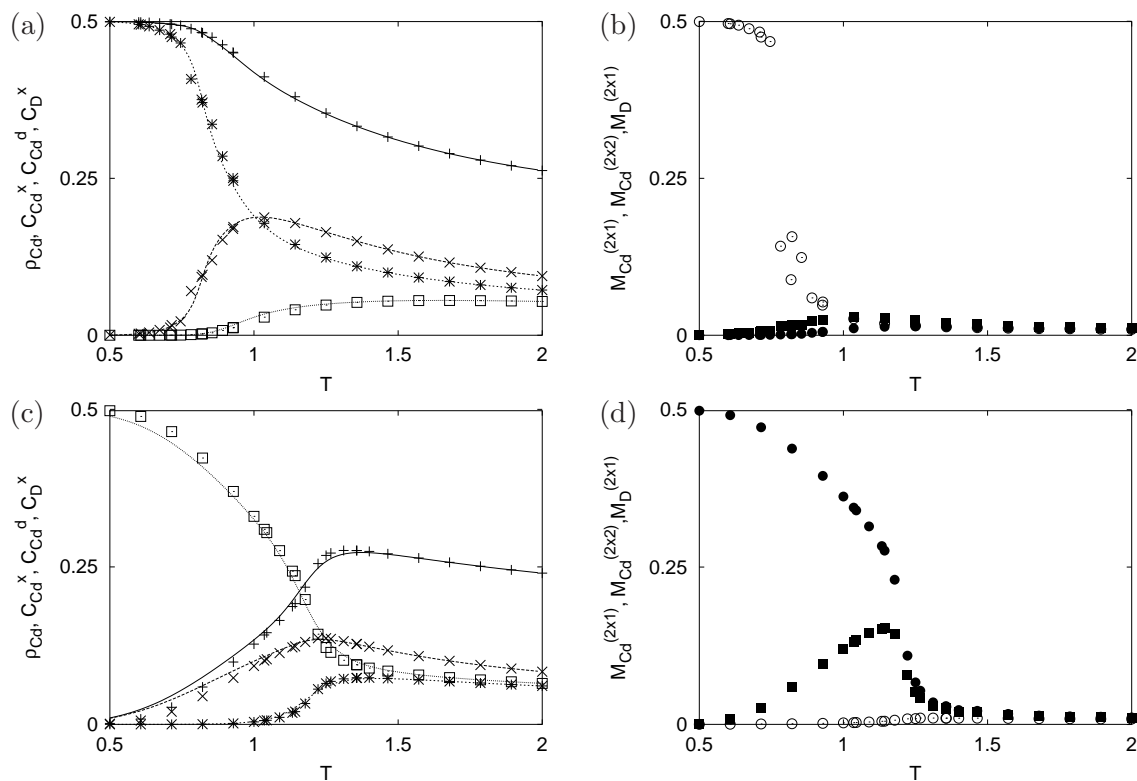


Figure 2.6: Simulations at constant chemical potential. Panels (a), (b) show the behaviour of the system with the couplings $\varepsilon_d = \varepsilon_b = -1$, $\varepsilon_x = \varepsilon_t = -1.9$ and a cadmium chemical potential $\mu = 1$. With these parameters, the ground state of the system is $c(2 \times 2)_{Cd}$. Panel (a) shows the Cd coverage ρ_{Cd} (+) and the correlations C_{Cd}^x (\times), C_{Cd}^d (\ast) and C_d^x (\square). Panel (b) shows the mean absolute of the order parameters $M_{Cd}^{(2 \times 2)}$ (\odot), $M_{Cd}^{(2 \times 1)}$ (\blacksquare) and $M_D^{(2 \times 1)}$ (\bullet). The symbols show data from a simulation run at a system size $L = N = 64$. $4 \cdot 10^4 \cdot LN$ events have been performed both for equilibration and for measurement. The lines have been obtained by means of a transfer matrix calculation at a strip width $L = 10$. The data shown in panels (c), (d) have been obtained at $\mu = 0.8$, where the ground state is $(2 \times 1)_{Te}$. All other parameters are identical to those used in (a), (b). The meaning of the symbols is the same as in panels (a) and (b).

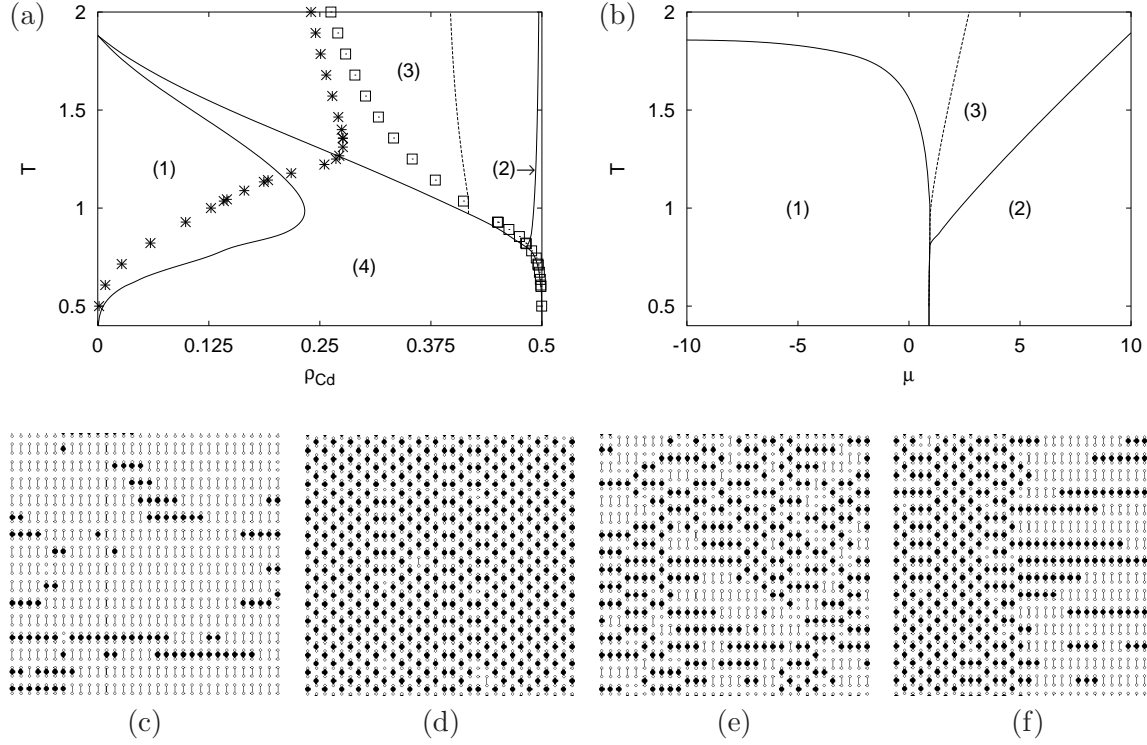


Figure 2.7: Phase diagram with parameters $\varepsilon_d = \varepsilon_b = -1$, $\varepsilon_x = \varepsilon_t = -1.9$. The solid lines in panel (a) show the lines of phase transitions as functions of ρ_{Cd} and T , in panel (b) they are shown in the μ - T plane. Note the offset in the temperature axes. In region (1), the system is in a homogeneously ordered phase with a $(2 \times 1)_{Te}$ reconstruction, in region (2) it is homogeneously ordered and $c(2 \times 2)_{Cd}$ reconstructed. Region (3) is the disordered phase. On the left side of the dashed line, the Cd atoms show preferentially a local (2×1) ordering ($C_{Cd}^x > C_{Cd}^d$), while on its right side a $c(2 \times 2)$ ordering dominates. Due to the coverage discontinuity between (1) and (2),(3), there is a coexistence regime where regions with high and low ρ_{Cd} coexist (4). The symbols show lines of constant $\mu = 0.8$ ($*$) and $\mu = 1$ (\square) (same data as in figure 2.6a,c). Panels (c)-(f) show typical surface snapshots. (c)-(e) correspond to grand-canonical simulations. The snapshots show surface configurations after $8 \cdot 10^4 \cdot LN$ events. (c): $T = 0.93$, $\mu = 0.8$ (phase 1), (d): $T = 0.71$, $\mu = 1$ (phase 2), (e): $T = 1.14$, $\mu = 1$ (phase 3). (f) displays a surface configuration after $2 \cdot 10^4 \cdot LN$ events in a canonical simulation at $T = 0.73$, $\rho_{Cd} = 0.35$ (Region 4, coexistence of phases 1 and 2). All snapshots show sections of $16\sqrt{2} \times 16\sqrt{2}$ zinc-blende lattice constants of systems of size $L = N = 64$.

phase transition between a $c(2 \times 2)_{\text{Cd}}$ and a $(2 \times 1)_{\text{Te}}$ reconstruction cannot be observed at constant chemical potential. The disordered phase (3) exists for $T \geq T_t$. At the point $(T = T_t, \mu = \mu_0)$ five phases coexist: the disordered phase, and $c(2 \times 2)_{\text{Cd}}$ and $(2 \times 1)_{\text{Te}}$ reconstructed phases in two sublattices, corresponding to positive and negative values of the order parameters $M_{\text{Cd}}^{(2 \times 2)}$ and $M_D^{(2 \times 1)}$, respectively. The $(2 \times 1)_{\text{Te}}$ reconstructed phase (1) exists only at temperatures below a critical temperature $T_c^1 \approx |\varepsilon_t|$. At T_c^1 , the line of the phase transition to the disordered phase (3) diverges to $\mu = -\infty$. On the contrary, the $c(2 \times 2)_{\text{Cd}}$ reconstructed phase (2) may exist at arbitrary temperature, if the Cd chemical potential is large enough. The dashed line in figure 2.7b shows the chemical potential at which the correlations C_{Cd}^d and C_{Cd}^x in the disordered phase are equal. For smaller μ , the local ordering of Cd atoms is dominated by a (2×1) arrangement, while for larger μ they prefer a local $c(2 \times 2)$ ordering.

The phase transition from phase (2) to phase (1) occurs at a temperature independent chemical potential μ_0 . At the transition between the phases (2) and (3), ρ_{Cd} varies continuously. Therefore, there is no coverage discontinuity if temperature is varied at a constant chemical potential $\mu > \mu_0$ where the groundstate is a $c(2 \times 2)_{\text{Cd}}$ reconstruction.

Figure 2.7a shows the phase diagram in the $\rho_{\text{Cd}}-T$ plane. There is a coverage discontinuity at the phase transition between the ordered phases (1) and (2) and at the transition between phases (1) and (3). These discontinuities yield a coexistence regime (4). Here, for $T < T_t$, $c(2 \times 2)_{\text{Cd}}$ and $(2 \times 1)_{\text{Te}}$ reconstructed phases coexist, while for $T > T_t$ the $(2 \times 1)_{\text{Te}}$ reconstructed phase coexists with the disordered phase. Figure 2.7f shows a surface snapshot from a simulation which was performed at a constant Cd density $\rho_{\text{Cd}} = 0.35$ and a temperature $T = 0.73$. This is a typical surface configuration in the regime where the ordered phases (1) and (2) coexist. The system is separated in two phases, one with a high ρ_{Cd} and a $c(2 \times 2)_{\text{Cd}}$ reconstruction, and another one with a $(2 \times 1)_{\text{Te}}$ reconstruction and a low concentration of Cd adatoms. The local values of ρ_{Cd} in both regions are given by the left and the right boundary of the coexistence regime. At low temperature one obtains $\rho_{\text{Cd}} \sim 0.5$ in the $c(2 \times 2)_{\text{Cd}}$ phase and $\rho_{\text{Cd}} \sim 0$ in the $(2 \times 1)_{\text{Te}}$ phase. At temperatures $T \gtrsim 0.6$, ρ_{Cd} in the $(2 \times 1)_{\text{Te}}$ phase increases strongly with T and obtains its maximal value 0.23 at $T = 0.98$. At even higher temperature it decreases with T and becomes zero at T_c^1 . On the contrary, ρ_{Cd} in the $c(2 \times 2)_{\text{Cd}}$ phase remains high for $T < T_t$. At $T > T_t$, the Cd-rich phase is disordered. Then, ρ_{Cd} at the right boundary of the coexistence regime decreases with T . At T_c^1 , it becomes zero and the coexistence regime disappears. The dashed line in figure 2.7a marks the values of ρ_{Cd} at which $C_{\text{Cd}}^x = C_{\text{Cd}}^d$. For smaller coverages, $C_{\text{Cd}}^x > C_{\text{Cd}}^d$ such that the local ordering of the Cd atoms is dominated by a (2×1) arrangement, while for greater coverages $C_{\text{Cd}}^x < C_{\text{Cd}}^d$. The values of ρ_{Cd} which have been measured in the simulations shown in figure 2.6 are plotted in the phase diagram as examples of lines of constant chemical potential. The loci of the phase transitions and the point where $C_{\text{Cd}}^x = C_{\text{Cd}}^d$ (at $\mu = 1$) are in good agreement with the results of the transfer matrix extrapolation.

Canonical ensemble

The temperature dependent behaviour of the model at a constant Cd adatom density $\rho_{\text{Cd}} = 0.35$ is shown in figure 2.8. This is an example which shows the typical behaviour of the model under the conditions of phase separation. At low temperature, most of the Cd atoms are concentrated in a Cd rich phase with a $c(2 \times 2)_{\text{Cd}}$ reconstruction. The remaining area of the system is covered with a $(2 \times 1)_{\text{Te}}$ reconstructed phase. Since both phases are long-range

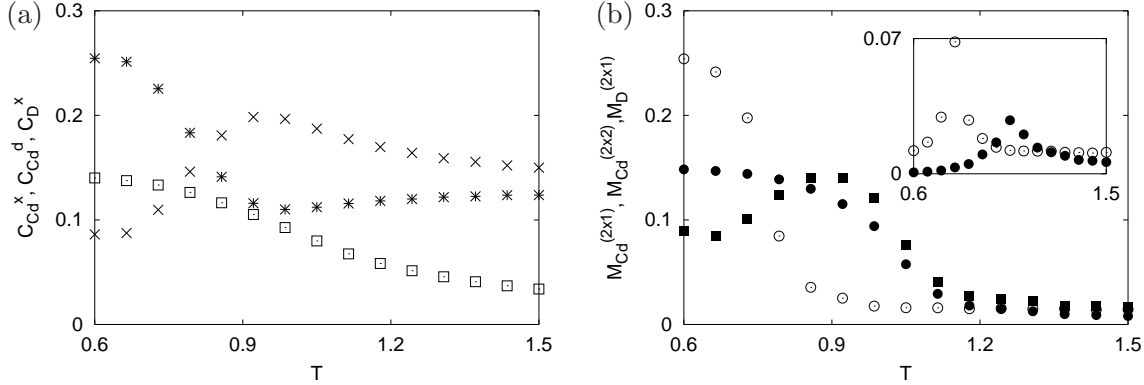


Figure 2.8: Results of a simulation of a 64×64 system at conserved $\rho_{Cd} = 0.35$ and couplings $\varepsilon_d = \varepsilon_b = -1$, $\varepsilon_x = \varepsilon_t = -1.9$. $10^4 \cdot LN$ events have been performed both for equilibration and for data sampling. Panel (a) shows the correlations C_{Cd}^x (\times), C_{Cd}^d ($*$) and C_d^x (\square). Panel (b) shows the mean absolute of the order parameters $M_{Cd}^{(2 \times 2)}$ (\odot), $M_{Cd}^{(2 \times 1)}$ (\blacksquare) and $M_D^{(2 \times 1)}$ (\bullet). The inset shows standard deviations of order parameters. The meaning of the symbols is the same as in the large picture.

ordered, we obtain large values of the order parameters $M_{Cd}^{(2 \times 2)}$, $M_D^{(2 \times 1)}$ and the corresponding correlations. The fraction of Cd atoms which occupy sites in the Te rich phase yields nonzero values of the order parameter $M_{Cd}^{(2 \times 1)}$. As temperature increases, more and more Cd atoms pass into the Te rich phase. This yields an increase in C_{Cd}^x and $M_{Cd}^{(2 \times 1)}$ and a decrease of C_{Cd}^d and $M_{Cd}^{(2 \times 2)}$ due to the (2×1) ordering of the Cd atoms *in the Te rich phase*. At the temperature T_t , the Cd rich phase undergoes the order-disorder transition where $M_{Cd}^{(2 \times 2)}$ drops to zero. At this phase transition, the fraction of Cd atoms which are incorporated in locally (2×1) ordered configurations *in the Cd rich phase* increases. Thus, there are two independent effects which lead to a dominance of C_{Cd}^x over C_{Cd}^d at higher temperature: The specific shape of the left boundary of the coexistence regime and the order-disorder transition of the Cd rich phase. At a temperature T_c^4 , the system is leaving the coexistence region into phase (3). At this phase transition, the separation between a Te rich and a Cd rich phase disappears, such that at high temperature the system is in a homogeneous, disordered state. The order parameters $M_D^{(2 \times 1)}$ and $M_{Cd}^{(2 \times 1)}$ become zero and the local correlation between dimers, $C_D^{(2 \times 1)}$, decreases. In the simulations we have determined the critical temperatures of the phase transitions from the standard deviations of the order parameters $M_{Cd}^{(2 \times 2)}$ and $M_D^{(2 \times 1)}$. $M_{Cd}^{(2 \times 2)}$ is peaked at T_t , where the long range order of the Cd atoms is lost, while $M_D^{(2 \times 1)}$ is peaked at T_c^4 , where the system leaves the coexistence regime and the dimers lose their long range order. We obtain $T_t = 0.79 \pm 0.2$ and $T_c^4 = 1.0 \pm 0.2$, where the uncertainty is due to the temperature spacing between the single simulations. These values are systematically lower than the theoretical results of the transfer matrix extrapolation ($T_t = 0.84$, $T_c^4 = 1.11$). However, the theoretical results are valid in the limit of an infinite system size, where the free energy of the phase boundary can be neglected compared to that of the bulk of the phases. We have verified that the systematic deviation between theory and simulations decreases with the system size.

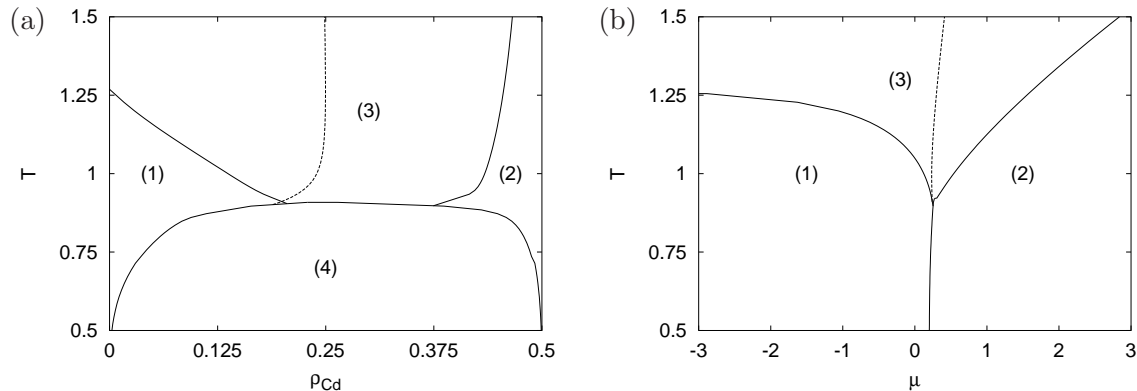


Figure 2.9: Phase diagram with the parameter set $\varepsilon_d = \varepsilon_b = -1$, $\varepsilon_x = -1.6$, $\varepsilon_t = -1.2$. Compared to the phase diagram shown in figure 2.7, the energy difference between the $c(2 \times 2)_{\text{Cd}}$ and the $(2 \times 1)_{\text{Cd}}$ reconstruction is greater and the interaction between dimers is weaker. With these parameters, the transition between phases (1) and (3) is continuous. Panel (a) shows the phase diagram in the $\rho_{\text{Cd}}-T$ plane, in panel (b) it is shown in the $\mu-T$ plane.

The influence of the parameter set on the phase diagram

Finally, we discuss the influence of the parameter set on the phase diagram. The main effect of a variation of the binding energy of the Te dimers ε_b is to shift the chemical potential at which the phase transitions occur. The influence on the shape of the phase diagram is small as long as ε_b is sufficiently large such that the density of Te atoms which are neither dimerized nor bound to Cd atoms is small. Due to the electron counting rule, a state where a large fraction of the Te atoms remains unbound should be irrelevant for CdTe.

A smaller energy difference ΔE between a perfect $c(2 \times 2)_{\text{Cd}}$ and a perfect $(2 \times 1)_{\text{Cd}}$ reconstruction increases the tendency of Cd atoms to arrange in a (2×1) order. If $\varepsilon_x = -1.95$ and all other parameters are identical to our standard parameter set, the dashed line where $C_{\text{Cd}}^x = C_{\text{Cd}}^d$ is shifted to a higher $\rho_{\text{Cd}} \approx 0.45$. Additionally, we obtain a higher value of 0.28 for the maximal Cd coverage in the Te rich phase, which is achieved at a lower temperature $T = 0.9$. The temperature $T_t = 0.7$ above which the disordered phase is stable is also slightly lower. In general, a greater value of $|\varepsilon_x|$ increases both the tendency of the Cd atoms to arrange in a (2×1) order in the disordered phase and the concentration of Cd atoms in the $(2 \times 1)_{\text{Te}}$ reconstructed phase. The temperature of the order-disorder transition in the Cd rich phase is lowered. Conversely, a *greater* energy difference between perfect $c(2 \times 2)_{\text{Cd}}$ and $(2 \times 1)_{\text{Cd}}$ reconstructed phases alters the temperature of this transition and leads to a preferential $c(2 \times 2)$ arrangement of the Cd atoms in the disordered phase.

The main effect of a variation of the interaction ε_t between Te dimers is to change the properties of the transition between the phases (1) and (3). As long as $|\varepsilon_t|$ is sufficiently high, the phase diagram is qualitatively similar to that shown in figure 2.7. In this case, the main effect of a variation of ε_t is to shift the temperature $T_c^1 \approx |\varepsilon_t|$ where the $(2 \times 1)_{\text{Te}}$ phase vanishes. However, at low $|\varepsilon_t|$ this transition becomes a *continuous* phase transition without any coverage discontinuity. As an example, in figure 2.7 a phase diagram with $\varepsilon_t = -1.2$, $\varepsilon_b = \varepsilon_d = -1$ and $\varepsilon_x = -1.6$ is shown. The coexistence regime (4) vanishes at $T_t = 0.9$ such that there is no phase separation between the long-range ordered $(2 \times 1)_{\text{Te}}$ phase and the disordered phase. This parameter set yields a comparatively high ΔE . Therefore,

the line where $C_{Cd}^x = C_{Cd}^d$ is at relatively low Cd coverages. In contrast to the situation at large $|\varepsilon_t|$, the chemical potential at which the transition from phase (1) to phase (2) occurs is not independent of temperature. Instead, the transition is at slightly greater μ at higher temperature. In consequence, there is a small range $0.2 < \mu < 0.27$ where there is a phase transition from phase (2) to phase (1) if T is increased at constant chemical potential. Qualitatively, the phase diagram at small $|\varepsilon_t|$ is reminiscent of that of the simplified model as far as the arrangement of Cd atoms is concerned.

2.3 Comparison with experimental results

The results presented in section 2.2.5 suggest an interpretation of the experimentally observed crossover from a $c(2 \times 2)_{Cd}$ reconstruction to a $(2 \times 1)_{Cd}$ reconstruction as an accompanying effect of an order-disorder phase transition. At low temperature, there is a long-range ordered Cd-rich phase with a $c(2 \times 2)_{Cd}$ reconstruction. At a critical temperature, the Cd atoms lose their long-range order and arrange preferentially in a (2×1) pattern. This picture is consistent with the experimental observation of small domains in the $(2 \times 1)_{Cd}$ reconstruction [74, 75] which indicate a high degree of disorder.

Strictly speaking, a CdTe surface under vacuum is not in thermal equilibrium. At the temperature of the $c(2 \times 2)_{Cd} - (2 \times 1)_{Cd}$ transition, sublimation plays an important role. As we will show in chapter 3, important features of the simplified model which neglects Te dimerization are preserved under the conditions of step-flow sublimation. This is the dominant sublimation mechanism for CdTe (001) [73]. However, the Cd coverage ρ_{Cd} is determined by the sublimation process. Therefore, within the limit of an equilibrium model it is not possible to calculate the path in the phase diagram that CdTe follows.

Auger measurements [74, 75] yield $\rho_{Cd} \approx 0.35$ at the transition temperature in vacuum. This suggests that the system is in the coexistence regime for a wide range of temperatures. Then, the behaviour of CdTe in vacuum should be similar to our results at constant $\rho_{Cd} = 0.35$ (figure 2.8). Electron diffraction techniques investigate large regions on the surface and hence yield averages over all coexisting phases. Consequently, it should be reasonable to compare results of these experiments with quantities which are averaged over the whole system in our canonical simulations. As discussed in section 2.2.5, there are two independent effects which lead to a clear dominance of the arrangement of Cd atoms in rows: the order-disorder transition in the Cd-rich phase and the fact that an increasing fraction of the Cd atoms is dissolved in the Te-rich phase. Electrons are diffracted both from the Cd atoms and the Te dimers which have a (2×1) order. The superposition of both effects should yield the pronounced (2×1) diffraction peaks which have been observed in [74, 75, 119].

In the $c(2 \times 2)_{Cd}$ reconstructed phase, at temperatures well below the phase transition one frequently finds collective thermal excitations of adatoms, where a row of several Cd atoms is shifted by one lattice constant in the y -direction. Due to the repulsion between Cd atoms in this direction, this is possible only if one Cd atom per excitation is missing. An example is shown in figure 2.7d. This effect has been observed experimentally by Seehover et. al. [108] at room temperature using STM microscopy. There is a striking similarity between figure 3 in [108] and figure 2.7d.

The phase diagram of our model explains the properties of the reconstructions of the CdTe (001) surface under an external particle flux. If the Cd coverage of the surface is increased by deposition of Cd, the state of the system moves into regions of the phase diagram where

the Cd atoms arrange preferentially in a $c(2 \times 2)$ pattern. Depending on temperature, this is either the ordered $c(2 \times 2)_{\text{Cd}}$ phase (2) or the region of the disordered phase (3) on the right side of the dashed line where $C_{\text{Cd}}^d > C_{\text{Cd}}^x$. Indeed, experiments [21, 119] have shown that an external Cd flux restores the $c(2 \times 2)_{\text{Cd}}$ reconstruction at high temperatures where a (2×1) order is found under vacuum conditions. Clearly, a strong Te flux induces the formation of a long-range ordered $(2 \times 1)_{\text{Te}}$ phase at temperatures below T_c^1 .

On ZnSe, a Zn terminated (2×1) reconstruction has not been observed yet. Our model offers an explanation of this fact which is consistent with the results of density functional theory [37, 39, 40, 79]. These calculations show, that for ZnSe the difference between the surface energies of perfect cation terminated $c(2 \times 2)$ and (2×1) reconstructions is significantly greater than for CdTe (0.03 eV per (1×1) surface unit cell versus 0.008 eV). In our model, this greater energy difference corresponds to a smaller value of $|\varepsilon_x|$ which shifts the line where $C_{\text{Cd}}^x = C_{\text{Cd}}^d$ to smaller coverages. Consequently, a $c(2 \times 2)_{\text{Zn}}$ arrangement dominates in a much wider range of coverages.

Wolfframm et. al. [129] have measured the locus of the transition between the $c(2 \times 2)_{\text{Zn}}$ reconstruction and the $(2 \times 1)_{\text{Se}}$ reconstruction as a function of temperature and the composition of an external particle flux by means of reflection high energy electron diffraction (RHEED). They find that at higher temperature a greater Se flux is required to obtain a (2×1) diffraction pattern. At temperatures above 450°C no $(2 \times 1)_{\text{Se}}$ reconstruction could be observed even under extremely Se-rich conditions. This is reminiscent of our observation that the anion-rich phase (1) vanishes at a temperature T_c^1 .

Unfortunately, the available experimental data are insufficient for a systematical fit of the model parameters. However, some rough estimates show that at least the orders of magnitude are reasonable. As discussed above, the $c(2 \times 2)_{\text{Cd}} - (2 \times 1)_{\text{Cd}}$ transition of CdTe in vacuum should be at a temperature close to T_t . Identifying this with the experimental value of 570 K, we obtain the value of our energy unit $|\varepsilon_d| \approx 0.06$ eV in physical units. This yields a value $\Delta E \approx 0.003$ eV for the difference in the surface energies of $c(2 \times 2)_{\text{Cd}}$ and $(2 \times 1)_{\text{Cd}}$, which is a bit less than 1/2 of the value of 0.008 eV which has been obtained by means of DFT calculations. This shows at least that the qualitative agreement between experiments and our model has been obtained in a physically reasonable region of the parameter space.

In our model, phase (1) vanishes at a temperature $T_c^1 \approx |\varepsilon_t|$. Identifying this with the value of 450°C which has been measured in experiments on ZnSe, we obtain that $|\varepsilon_t| \approx 0.06$ eV. This is the same order of magnitude as our estimate of $|\varepsilon_d|$ in CdTe.

These considerations suggest that it should be possible to obtain quantitative agreement between experiments and our model both for CdTe and ZnSe with values of the model parameters on the order of magnitude of a few ten meV.

Chapter 3

Reconstructions on non-equilibrium crystal surfaces

In section 2, we have presented a lattice gas model which displays an order-disorder phase transition the properties of which are reminiscent of the $c(2 \times 2)_{\text{Cd}}-(2 \times 1)_{\text{Cd}}$ reordering of the Cd atoms at the CdTe(001) surface. However, a crystal surface in an MBE chamber is not in thermal equilibrium. In the presence of a particle flux, the crystal grows. Under vacuum, there is sublimation (section 1.7).

In the literature, a few models of crystal growth have been presented which take into account the effects of surface reconstructions. On the one hand, there have been models which aim at a detailed understanding of the features of specific materials, in particular Si [13, 94] and GaAs [45, 54, 56]. On the other hand, Chin and den Nijs [20] have investigated a simple model to address the fundamental question whether there might be a reconstruction order on growing surfaces. They find, that a long range order in the strict sense which is present in thermal equilibrium [30] is absent during growth. However, the order of the reconstruction is preserved on small and intermediate lengthscales.

To the best of our knowledge, phase transitions between different reconstructions have not been considered in growth models, so far. Consequently, a theoretical understanding of the interplay of this phenomenon with the dynamics of growing or sublimating surfaces has not yet been achieved. We address this important problem in the context of a model of a compound material that displays a competition of different vacancy structures in the terminating layer similar to the lattice gas model which was introduced in section 2.2.4. In particular, we address the following questions: (1) It has been claimed [74, 75] that the surface layer is in effective thermal equilibrium under the non-equilibrium conditions of sublimation. Is this justified? If not, which features of an equilibrium phase transition are preserved? (2) What is the effect of an external flux of particles of one species on the surface reconstruction? These simulations model situations which are given in experiments where phase diagrams like that shown in figure 2.3 are determined.

3.1 The model

Our model is an extension of the simplified planar lattice gas model introduced in section 2.2.4 to a model of a three-dimensional crystal. In this chapter, we aim at an understanding of fundamental properties of nonequilibrium crystal surfaces rather than a realistic modelling of

CdTe. To this end, we consider a lattice gas model of a compound “ AB ” with a cubic lattice and a comparatively simple potential energy surface. The A (B) atoms correspond to Cd (Te). We impose the constraint that there are no overhangs and dislocations. This *solid-on-solid* condition makes it possible to describe the configuration of the crystal uniquely by a two-dimensional array h of integers $\{h_{i,j}\}_{i,j=1}^N$ which denote the height of the column of atoms at x -coordinate i and y -coordinate j . Thus, we achieve an effectively two-dimensional description of a three-dimensional crystal which reduces the complexity of our model considerably.

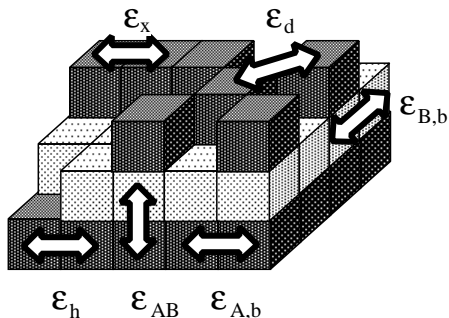


Figure 3.1: Sketch of a surface showing the interactions between the particles. A particles are shown as dark cubes, B particles in light grey. The x -axis points from left to right, the y -axis from front to back.

To model the layered structure of the CdTe crystal, we assign the odd heights to A particles, and the even heights to B particles. In the following, the term monolayer (ML) will denote one AB layer, i.e. the height difference between adjacent monolayers is 2. Inside the bulk of the crystal, there is an attractive interaction between the particles and their nearest neighbours which is isotropic in directions parallel to the surface. While there is no difference in the interaction of B particles between the bulk and the surface, A particles on the surface interact with the anisotropic interactions of the simplified version of our lattice gas model of the CdTe(001) surface introduced in section 2.2.4. The other parameters of the model are defined in Figure 3.1. Thus, the Hamiltonian of the crystal becomes

$$H = \varepsilon_{AB}n_{AB} + \varepsilon_{B,b}n_{B,b} + \varepsilon_{A,b}n_{A,b} + \varepsilon_h n_{A,h} + \varepsilon_d n_{A,d} + \varepsilon_x n_{A,x} \quad (3.1)$$

Here, n_{AB} is the number of A - B bonds between the layers, $n_{B,b}$ is the number of nearest neighbour pairs of B atoms, $n_{A,b}$ the number of A nearest neighbour pairs inside the bulk, $n_{A,h}$ the number of surface A atoms next to a higher column and $n_{A,d}$ ($n_{A,x}$) the number of bonds of surface A atoms to diagonal neighbours (nearest neighbours in x -direction) at the same height. The occupation of neighbouring sites in the y -direction with A -atoms is forbidden, independent of the height difference between both atoms. Additionally, atoms must not stay in the wrong sublattice.

In addition to diffusion to nearest neighbour sites we permit diffusion to diagonal neighbour sites. This process is important to obtain a reasonable mobility of A atoms on a B terminated surface. An example is shown in figure 3.2a. In the absence of diagonal neighbour diffusion, due to the repulsive interaction in y -direction an A atom at the edge of an A -cluster cannot diffuse along the cluster edge. Consequently, an equilibration of the cluster configuration is possible only via the detachment of atoms from the cluster. However, this process has a large activation energy since all bonds in the horizontal direction must be broken.

Additionally, we permit the diffusion of an AB pair with the B atom on top of the A atom, if the diffusion of the B atom alone would end in the wrong sublattice. This process is required to preserve the ergodicity of the system. Consider the surface configuration shown

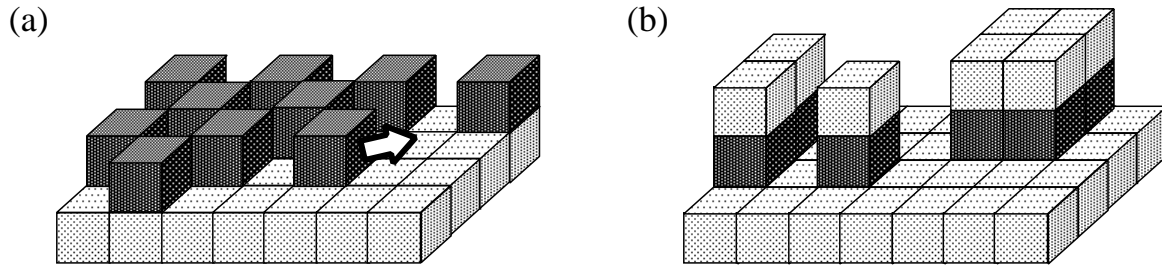


Figure 3.2: Motivation for diffusion to diagonal neighbour sites and diffusion of AB pairs. A atoms are shown as dark cubes, B particles in light grey. The x -axis points from left to right, the y -axis from front to back. Panel (a): Diffusion of A atoms on a B terminated surface. The diffusion of an A atom (arrow) along the edge of a cluster of other A atoms is severely restricted without diffusion to diagonal neighbour sites. Panel (b): Coalescence of islands is impossible without AB diffusion.

in figure 3.2b. Since atoms must not stay in the wrong sublattice the B atoms on top of the islands cannot diffuse across the gap between the islands. Consequently, the energetically favourable coalescence of the islands is suppressed unless AB pairs are allowed to diffuse together. However, it is not necessary to permit also the diffusion of AB pairs with the A atom on top since the vacancy structure of A terminated islands is more flexible than a flat B terminated layer. We have performed some trial simulations where the diffusion of both arrangements of AB pairs was permitted. The results are identical to those of the standard model.

Diffusion is an Arrhenius activated process (equation 1.2). For simplicity, we assume an equal activation energy B_0 for all diffusion processes where the energy of the system does not increase. Then, due to the detailed balance condition B.3 which will be discussed in appendix B, the barrier height for the diffusion of a particle to a site which is energetically unfavourable compared to the initial site is necessarily $B_0 + \Delta H$. Here, ΔH is the energy difference between the initial and the final state of the system. In the literature, a dynamics with these rates is denoted as “Kawasaki dynamics” [76]. The desorption of a particle requires an additional activation energy ε_v . This dynamics does not depend on the parameter ε_{AB} , so it needs not to be specified, and $\varepsilon_{B,b}$ and $\varepsilon_{A,b}$ enter only via the sum $\varepsilon' := \varepsilon_{B,b} + \varepsilon_{A,b}$. The constant prefactor $1/t_0 := \nu \exp(-B_0/kT)$ sets the timescale of the model and needs not to be specified, if we measure time in units of t_0 . Particles from an external source arrive at each lattice site with equal probability. If the adsorption of the particle at this site would lead to a forbidden state, it is reflected.

The simulations are performed using continuous time Monte Carlo techniques. A detailed discussion of the algorithm can be found in appendix B.

For simplicity, we measure energy in units of $|\varepsilon_d|$ and set Boltzmann’s constant to unity. In the following, we use the parameter set $\varepsilon' = \varepsilon_d = -1$, $\varepsilon_h = 0$, $\varepsilon_x = -1.97$, $\varepsilon_v = 1.5$. With these parameters, the difference in the surface energies between perfectly $c(2 \times 2)$ and (2×1) reconstructed surfaces is small compared to the surface energies themselves. This is consistent with our finding in chapter 2 that a small ΔE is an essential feature of the $c(2 \times 2)_{Cd} - (2 \times 1)_{Cd}$ reordering. We have verified that the behaviour of our model remains qualitatively the same for a wide range of parameters, as long as the basic property of a small energy difference between the A terminated reconstructions is preserved.

3.2 Characterization of the surface

The surface width $W := \langle (h_{i,j} - \langle h_{i,j} \rangle)^2 \rangle$ is a measure for the roughness of the surface. To characterize the arrangement of A atoms quantitatively, we investigate correlations and an order parameter similar to the quantities which were defined in section 2.2.2. To this end, we consider an array c of integers $c_{i,j} := h_{i,j} \bmod 2$. $c_{i,j} = 1$ if the column of atoms at (i, j) is terminated by an A atom and zero otherwise. These variables can be used to calculate the A coverage $\rho_A := N^{-2} \sum_{i,j=1}^N c_{i,j}$ and the normalized correlations

$$K_A^d := \frac{1}{2\rho_A N^2} \sum_{i,j=1}^N c_{i,j} (c_{i+1,j+1} + c_{i+1,j-1}) \quad (3.2)$$

$$K_A^x := \frac{1}{\rho_A N^2} \sum_{i,j=1}^N c_{i,j} c_{i+1,j}. \quad (3.3)$$

These definitions are similar to those of C_{Cd}^d and C_{Cd}^x in equations 2.2 and 2.3. We have normalized the correlations with the A coverage such that K_A^d and K_A^x are equal to the fraction of A atoms which are incorporated in locally $c(2 \times 2)$ and (2×1) reconstructed regions of the surface, respectively. The long range order of the A atoms is measured by the order parameter $M_A^{(2 \times 2)}$ the definition of which is identical to that of $M_{Cd}^{(2 \times 2)}$ in equation 2.4.

As we will show, there is no long range order in the strict sense in our model such that $M_A^{(2 \times 2)}$ is zero even at low temperature. However, there might be correlations between A atoms at intermediate distance. These are characterized by means of the autocorrelation function

$$C(\vec{x}) := \langle c_{i,j} c_{i+x,j+y} \rangle - \rho_A^2 \quad (3.4)$$

of c . If the positions of A atoms at a distance $\vec{x} = (x, y)$ are uncorrelated, we have $C(\vec{x}) = 0$. Ornstein-Zernike theory [19] states that in thermal equilibrium the asymptotical behaviour of $|C(\vec{x})|$ for large $|\vec{x}|$ is

$$|C(\vec{x})| \sim C_\infty + \lambda |\vec{x}|^{-(d-1)/2} \exp(-|\vec{x}|/\xi) \quad (3.5)$$

where ξ is the correlation length and d is the dimension of the system. A nonzero value of C_∞ indicates long range order. This equation is not valid at the locus of a phase transition where the correlation length diverges. Note, that in a system with anisotropic interactions the constants C_∞ , λ and ξ may have a directional dependence. If neighbouring sites are correlated, $C(\vec{x})$ is always positive. If the values of $c_{i,j}$ on neighbouring sites are anticorrelated, $C(\vec{x})$ oscillates between positive and negative values. In our model, this is necessarily the case if \vec{x} is parallel to the y -direction since there is a hard repulsion between A atoms on neighbouring sites in this direction. However, if \vec{x} points in the x -direction, the configuration of neighbouring sites is anticorrelated only if the A atoms arrange preferentially in a $c(2 \times 2)$ pattern. On a (2×1) reconstructed surface neighbouring sites in the x -direction are correlated. If $K_A^x \approx K_A^d$, these effects compensate each other. Consequently, on such a surface we expect a very small correlation length in the x -direction.

3.3 Layer-by-layer sublimation

Figure 3.3 shows the evolution of an initially B terminated, flat surface under vacuum at a temperature $T = 0.5$. At the beginning of the simulation, ρ_A increases from zero to an

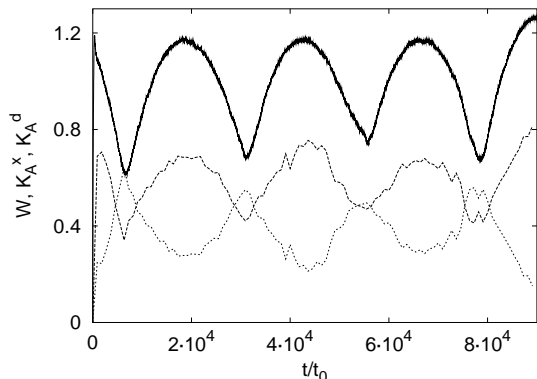


Figure 3.3: Sublimation starting from a flat B terminated surface at $T = 0.5$. The system size is $N = 128$. Solid line: W , dashed: K_A^x , dotted: K_A^d . For clarity of plotting, the last two curves have been smoothed; W shows the natural fluctuations. Each oscillation period corresponds to the desorption of one monolayer.

asymptotic value close to 0.5. Thus, the sublimating surface is A terminated.

We find, that this increase can be fitted with an exponential relaxation, $\rho_A = \rho_A^\infty(1 - \exp(-t/\tau))$. Here, τ is the time constant of the decay of the B terminated surface. The temperature dependence of the corresponding desorption probability $p \propto 1/\tau$ follows an Arrhenius law, $p \propto \exp(-E_{\text{sub}}/T)$, with an activation energy $E_{\text{sub}} = B_0 + 3.0 \pm 0.1$

After this onset, A and B evaporate stoichiometrically, and sublimation proceeds in layer-by-layer mode (see section 1.7). This is reflected by the oscillations of the surface width W (solid line in figure 3.3). Whenever the surface is atomically flat, W is minimal. The maxima of W correspond to a configuration where 50% of the surface are covered with islands of one monolayer thickness. The dependence of the sublimation rate on T follows an Arrhenius law with an activation energy $B_0 + 6.0 \pm 0.2$ which is greater than that found for the decay of the B terminated surface. However, in our model the *microscopic* energy barriers for desorption of A and B are equal. Consequently, the difference in the *macroscopic* activation energies is solely a consequence of the stabilizing effect of the reconstruction of the A terminated surface.

Surprisingly, K_A^d and K_A^x oscillate during layer-by-layer sublimation. Each time a complete AB layer has desorbed and the surface is atomically flat (minima of W) the $c(2 \times 2)$ reconstructed fraction of the surface is maximal. On the contrary, a rough surface with a large number of islands (maxima of W) seems to prefer the (2×1) reconstruction. This can be understood from the fact that the attractive lattice gas interactions are present only between particles in the same layer. Thus, the island edges impose open boundary conditions to the lattice gas of A atoms on the island. In contrast to a $c(2 \times 2)$ reconstructed domain, a (2×1) terminated island can *reduce* the energy of its boundary by elongating in x -direction. Since the ground state energies of both structures are nearly degenerate, the formation of (2×1) may reduce the surface free energy. This picture is confirmed by the fact that islands on sublimating surfaces are indeed elongated (see figure 3.4b).

3.4 Step-flow sublimation

Clearly, an oscillatory behaviour cannot be understood within the framework of equilibrium thermodynamics. However, pure layer-by-layer sublimation is rarely ever observed in experiments. In particular, investigations of CdTe [73] have shown, that step-flow sublimation is the dominant mechanism.

We determine the energy of steps in our model. This is done by calculating the energy which is needed to shift one half of a large crystal by the thickness of one monolayer in the

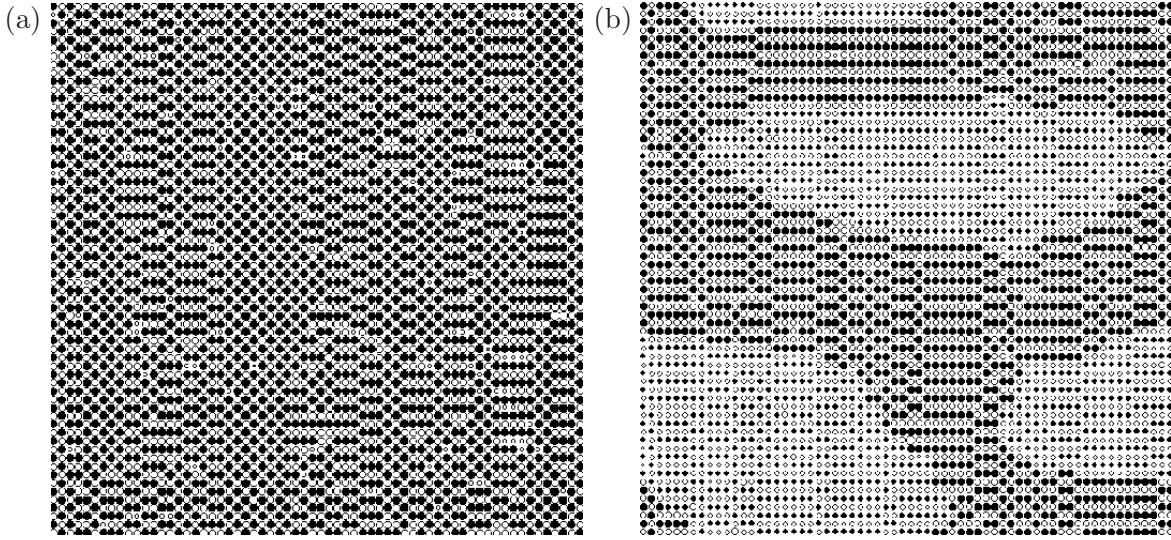


Figure 3.4: Evolution of the surface of a 64×64 system in layer-by-layer sublimation. A atoms are shown as filled circles, B atoms as open circles. Greater symbols denote greater surface heights. Panel (a) shows a surface snapshot at $t = 7000 \cdot t_0$ where the surface roughness is minimal, panel (b) shows the surface at $t = 19000 \cdot t_0$ where the roughness is maximal.

z -direction. In this process, two steps are created: one at the upper side of the crystal and a second one at the lower side. Consequently, the step energy is one half of the total energy costs. Normalizing this with the length of the step, we obtain the step energy per unit length. On perfectly $c(2 \times 2)$ reconstructed surfaces, we find

$$\gamma_{\text{diag}} = \frac{-1}{\sqrt{2}} (\varepsilon_x + \varepsilon') \quad (3.6)$$

for diagonal steps and

$$\gamma_{\text{par}} = -\varepsilon_d - \frac{1}{2}\varepsilon' + \frac{1}{2}\varepsilon_h \quad (3.7)$$

for steps oriented in x - or y -direction. With our standard parameter set, we have $\gamma_{\text{diag}} = \sqrt{2} < \gamma_{\text{par}} = 3/2$. Therefore, at $T = 0$ steps oriented at an angle of 45° to the coordinate axes are favoured energetically. We expect, that this holds also at finite temperature as long as the surface is $c(2 \times 2)$ reconstructed.

Diagonal steps in the simple cubic lattice of our model correspond to steps oriented in the $[100]$ or $[010]$ direction on the zinc-blende lattice. Indeed, investigations of CdTe(001) by means of STM microscopy [67, 68] have shown, that this is the preferential orientation of steps.

In the following, we present the results of simulations of vicinal surfaces with diagonal steps. We find that the oscillations in the correlations disappear for terrace widths smaller than ≈ 50 lattice constants, where sublimation proceeds in step-flow mode. Then, the correlations become stationary apart from statistical fluctuations.

Figure 3.6 shows the T -dependence of ρ_A , K_A^d , K_A^x and the sublimation rate r_{sub} in this stationary state at a step distance of $32\sqrt{2}$ lattice constants. In the investigated temperature range ρ_A decreases only slightly from $\rho_A = 0.498$ at $T = 0.4$ to $\rho_A = 0.41$ at $T = 0.8$. Clearly,

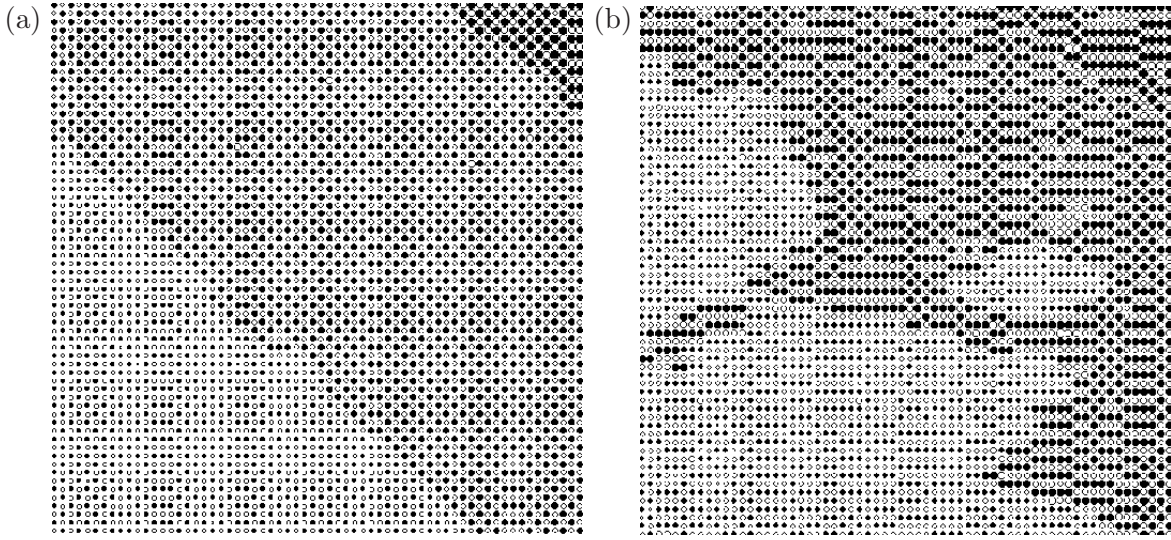


Figure 3.5: Vicinal surfaces sublimating in step flow mode. The images show sections of 64×64 lattice constants of surfaces at the end of the simulation runs shown in figure 3.6. Panel (a): $T = 0.4$ (below the reordering), Panel (b): $T = 0.6$ (above the reordering).

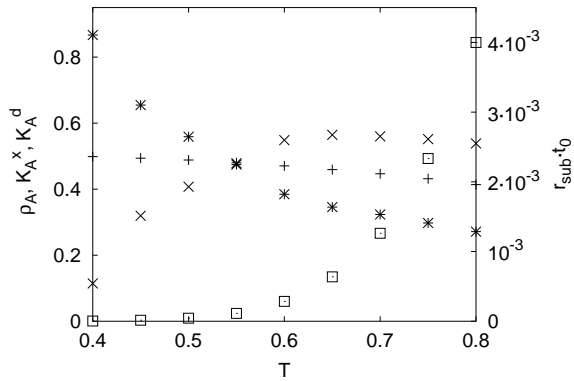


Figure 3.6: A -coverage ρ_A (+), correlations K_A^x (\times), K_A^d (\ast) and sublimation rate r_{sub} (\square) in the stationary state of the sublimation of vicinal surfaces under vacuum. The system size is $N = 128$. The steps are oriented in the diagonal direction, the terrace width is $32\sqrt{2}$ lattice constants. The data points show time averages of the investigated quantities. $3 \cdot 10^4 t_0$ time has been simulated both for relaxation and for measurement.

at $T = 0.55$ there is a transition from a $c(2 \times 2)$ configuration at low temperature to a high temperature regime where the (2×1) ordering dominates. This is reminiscent of the behaviour of the correlations in the vicinity of the order-disorder phase transition of the planar lattice gas (compare with figure 2.4). Figure 3.5 shows typical configurations of the surface at $T = 0.4$ which is below the reordering (figure 3.5a) and at $T = 0.6$ above the reordering (figure 3.5b).

Comparing the results of our simulations of the sublimating surface with the anisotropic lattice gas introduced in section 2.2.4 we can check in how far the properties of the A atoms on the surface can be understood within an equilibrium theory of a flat surface. For simplicity, in the following we denote the planar lattice gas as “2D model” and the solid-on-solid model as “3D model”. We investigate the 2D model at the value of ρ_A which is measured on the surface of the 3D model sublimating in step-flow mode. We perform canonical Monte Carlo simulations where the number of A atoms is fixed. Additionally, we consider results of transfer matrix calculations where the chemical potential μ is adjusted to obtain the desired

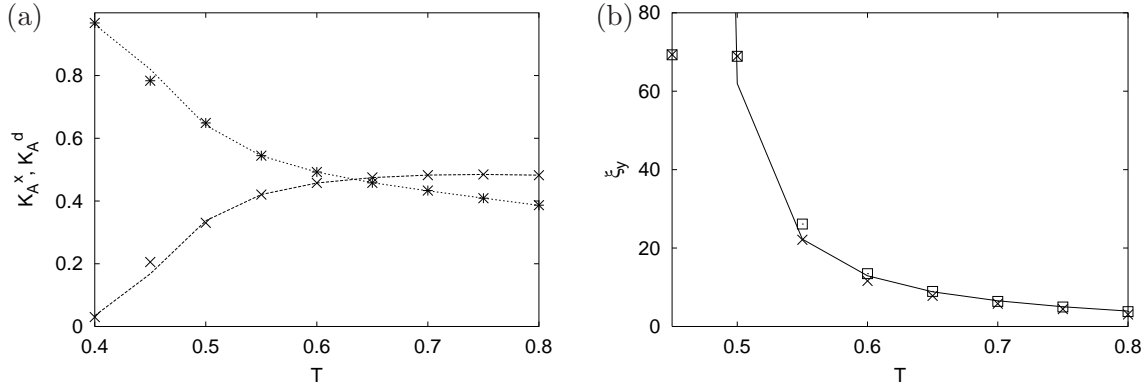


Figure 3.7: Panel (a): Correlations in the planar lattice gas at the value of ρ_A which is found on a sublimating surface. The dashed (dotted) line shows K_A^x (K_A^d) obtained from a transfer matrix calculation at a strip width $L = 16$. Additionally, we show the results of canonical Monte Carlo simulations (\times : K_A^x , \ast : K_A^d). The system size is $N = 128$. $10^4 \cdot N^2$ Monte Carlo steps have been performed both for equilibration and for measurement. Panel (b): Correlation length in the y -direction measured on the sublimating surface (\times) and in an equilibrium Monte Carlo simulation of the planar lattice gas (\square). The solid line shows results of a transfer matrix calculation. These data have been measured in the simulations shown in figure 3.6 and in panel (a).

A coverage. Of course, the values of the parameters $\varepsilon_x = -1.97$ and $\varepsilon_d = -1$ are identical to those used in the 3D model. Figure 3.7 shows the equilibrium values of K_A^x and K_A^d in the 2D model. The simulation results agree well with the results of the transfer matrix calculation. Qualitatively, the behaviour of the 2D model resembles that of the 3D model. There is a crossover between a dominant $c(2 \times 2)$ arrangement at low temperature and a high temperature regime where the A atoms preferentially arrange in rows. However, there is no quantitative agreement. In the 2D model, the reordering occurs at a higher temperature. Additionally, at all investigated temperatures the $c(2 \times 2)$ reconstructed fraction of the surface is greater than in the 3D model.

We determine the temperature T_c at which the 2D model leaves the long range ordered phase (I) and enters the disordered phase (II). Monte Carlo simulations and transfer matrix calculations yield $T_c \approx 0.45$ for the phase transition of the infinite system. However, in our simulations of the 3D model we find that $M_A^{(2 \times 2)} = 0$ apart from statistical fluctuations even at $T = 0.35$. Thus, there is no long range order of the A atoms on the surface of the sublimating crystal.

An inspection of surface snapshots of the 3D model (figure 3.5a) at low temperature shows, that there are several $c(2 \times 2)$ reconstructed domains. In each domain, the A atoms occupy one of the two sublattices which correspond to positive and negative values of $M_A^{(2 \times 2)}$, respectively. Domains of both orientations cover equal areas such that on average $M_A^{(2 \times 2)} = 0$. The domains have an elongated shape where the domain size in the y -direction is much greater than that in the x -direction. Frequently one encounters domains which run through the whole system. Thus, there are long domain walls parallel to the y -direction which consist of a row of pairs of A atoms on neighbouring sites in the x -direction. Of course, these pairs contribute to K_A^x . Consequently, the formation of domain walls on sublimating surfaces explains both

the absence of long range order and the greater values of K_A^x compared to the 2D model.

We investigate correlation lengths in the 2D and in the 3D model. This is done by fitting an Ornstein-Zernike law (equation 3.5) to $C(\vec{x})$ which is measured in the Monte Carlo simulations.

To check whether this method yields correct results we compare the correlation length in the y -direction ξ_y in the 2D model with a transfer matrix calculation where ξ_y is determined from the eigenvalues according to equation A.16. We find, that $C((0, y)^\top)$ follows an Ornstein-Zernike law for distances greater than 15 lattice constants. The results are shown in figure 3.7b. At high temperature, Monte Carlo data and results of the transfer matrix calculation agree well. Clearly, in a finite system with periodic boundary conditions, the correlation length cannot exceed one half of the system size. Therefore, at low temperature where the transfer matrix calculations yield very large ξ_y , the Monte Carlo results saturate at values close to 64. Consequently, our fitting procedure is reasonable for correlation lengths which are small compared to the system size.

We find, that in the 3D model $C((0, y)^\top)$ agrees well with an Ornstein-Zernike law although this is strictly valid only in thermal equilibrium. Interestingly, we find values of ξ_y which agree well with the equilibrium results of the 2D model (figure 3.7b).

Since $C((x, 0)^\top)$ depends strongly on which of K_A^x and K_A^d is greater, we expect a different behaviour of correlations in the x -direction in the 2D and in the 3D model. Indeed, this is the case. In general, correlation lengths ξ_x in the x -direction are small. Consequently, on large lengthscales where a fit to an Ornstein-Zernike law would make sense, $C((x, 0)^\top)$ is indistinguishable from its asymptotical value. Therefore, we present only qualitative results. At all temperatures, ξ_x in the 3D model is significantly greater than in the 2D model. Probably this is a consequence of the rows of A atoms parallel to the x -direction which are characteristic of the (2×1) arrangement.

3.5 The surface under an external particle flux

To get insight into the behaviour of a material in an MBE environment, it is important to understand how the structure of the surface changes if it is exposed to a particle beam. Additionally, these investigations give us insight into the behaviour of the surface at A coverages which differ from the value found under vacuum conditions.

We simulate vicinal surfaces which are exposed to a flux of pure A or B . Panels (a) and (c) of figure 3.8 show the quantities ρ_A , K_A^x and K_A^d as functions of the particle flux F at a temperature $T = 0.45$ which is below the $c(2 \times 2)$ - (2×1) reordering under vacuum, and at $T = 0.57$ which is slightly above the transition.

An A flux increases ρ_A . This leads to an increase of K_A^d such that under a large A flux the A atoms arrange preferentially in a $c(2 \times 2)$ pattern even at temperatures above the reordering under vacuum (figure 3.8c). Applying B fluxes, we can regulate ρ_A to values smaller than those close to 0.5 observed under vacuum. We find, that a decrease of ρ_A makes the remaining A atoms arrange preferentially in the rows of the (2×1) reconstruction.

In figure 3.8b,d we show the correlations K_A^x and K_A^d which are found in the 2D model at the value of ρ_A which is measured in the 3D model. A comparison of these results with the behaviour of the 3D model shows, that the qualitative similarity and the quantitative differences between the 2D model and the 3D model which have been observed under vacuum are preserved in a wide range of A coverages. There is no long range order of the A atoms

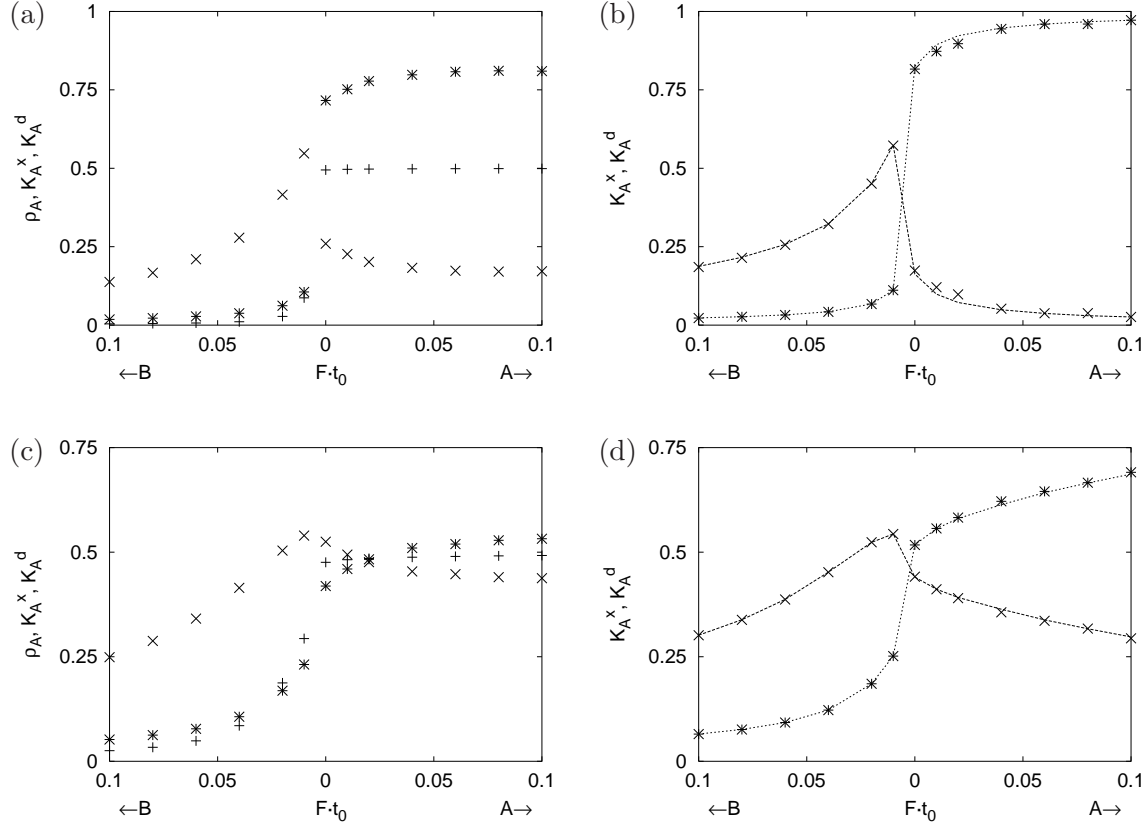


Figure 3.8: A coverage ρ_A (+) and correlations K_A^x (\times), K_A^d (\ast) in the stationary state of vicinal surfaces under an external particle flux and equilibrium values in the planar lattice gas at the A coverage measured on the crystal surface. Panel (a): Behaviour of the 3D model at $T = 0.45$. The steps are oriented in the diagonal direction, the terrace width is $32\sqrt{2}$ lattice constants. Panel (b): Results of the 2D model at the value of ρ_A measured on the sublimating surface at the flux indicated at the x -axis. The symbols denote results of Monte Carlo simulations, the lines show values determined by means of a transfer matrix calculation at a strip width $L = 16$. Panels (c) and (d): 3D model (c) and 2D model (d) at $T = 0.57$. All other parameters are identical to those used in (a) and (b). Note that an A -flux applied to the surface of the 3D model leads to a re-entry into the $c(2 \times 2)$ reconstructed configuration at a temperature above the reordering under vacuum. In all Monte Carlo simulations shown, the system size is 128×128 lattice constants. In the equilibrium simulations, $10^4 \cdot N^2$ Monte Carlo steps have been performed both for equilibration and for measurement. In the majority of the simulations of the sublimating surface, time averages over $3 \cdot 10^4 t_0$, following a time interval of the same length for relaxation have been performed. Since the relaxation of surfaces under an A flux at $T = 0.45$ is very slow, a longer time interval of $10^6 t_0$ has been used in these simulation runs.

even at high A flux and low temperature. Instead, there are domains which are elongated in the y -direction. This yields $M_A^{(2 \times 2)} = 0$ and values of K_A^x which are greater than those found in the 2d model. At low A coverages we find that in the 3D model both K_A^x and K_A^d are slightly smaller than in the 2D model. An investigation of $C(\vec{x})$ at surfaces under a particle flux shows, that correlation lengths in the y -direction in the 2D model and in the 3D model agree quantitatively, while there are significant differences in ξ_x .

3.6 Conclusions

In summary, our simulations reproduce the experimental results for the reconstruction of Cd terminated CdTe(001) surfaces qualitatively. Under vacuum, there is a crossover from a $c(2 \times 2)$ reconstruction at low temperature to a high temperature phase with a dominant (2×1) arrangement. An external flux of A atoms stabilizes the $c(2 \times 2)$ arrangement at temperatures above the reordering in vacuum. We find that correlation lengths in the y -direction are much greater than those in the x -direction. This agrees with experimental results reported in [74, 75].

We have shown that the reconstruction order of A atoms on a vicinal surface sublimating in step flow mode does not change qualitatively compared to a planar lattice gas in thermal equilibrium. In particular, the behaviour of the short range correlations K_A^x and K_A^d in the 3D model is quite similar to that found in the 2D model. This shows, that the investigation of comparatively simple models like those introduced in chapter 2 is an appropriate tool to get insight into the behaviour of reconstructed surfaces under MBE conditions.

The nonequilibrium conditions of sublimation induce characteristic deviations of the arrangement of A atoms on the surface from the equilibrium configuration. Perhaps the most important one is the absence of long range order at low T and high ρ_A . This is reminiscent of the behaviour of the growth model of Chin and den Nijs [20].

Our findings can be understood within the following picture of sublimation: There is a permanent creation and annihilation of reconstructed surface. As the terminating layer of the crystal evaporates, the layer below is uncovered and becomes the new surface. In this process, a given atom stays on the surface for a typical time $\tau_{\text{rel}} = 1/r_{\text{sub}}$ before it is desorbed. During this time, the arrangement of the atoms evolves towards the equilibrium configuration. However, it is insufficient for a complete equilibration. Therefore, there are characteristic defects in the reconstruction order of A atoms.

At low temperature and high A coverage, there is a division of the surface in domains. Most of the domain walls run in the y -direction. This can be understood from the fact that the formation of such a domain wall requires only a small energy of $\Delta E = |2\varepsilon_d - \varepsilon_x|/2 = 0.015$ per unit length. Thus, there is only a comparatively small driving force which makes the domains coarse. Similarly, the small energy difference between a $c(2 \times 2)$ order and a (2×1) arrangement might be responsible for the high values of K_A^x at high temperature. At small ρ_A , both K_A^d and K_A^x are smaller than in thermal equilibrium. This indicates, that in the 3D model there is a higher fraction of single A atoms than in the 2D model. This may be understood from the fact that τ_{rel} is not sufficient for some diffusing adatoms to meet a binding partner.

On the other hand, the good agreement between the correlation lengths in the y -direction measured in the 2D model and in the 3D model shows, that important aspects of the statistical mechanics of the lattice gas in thermal equilibrium are preserved in step flow sublimation.

Chapter 4

Simulation of CdTe

In this chapter, we extend the model of a binary compound with surface reconstructions presented in chapter 3 to make it a more realistic model of CdTe. We simulate the zinc-blende lattice of II-VI semiconductor crystals instead of a simple cubic lattice. To be meaningful, a fully three-dimensional modelling of the CdTe crystal requires a detailed understanding of the interactions of the atoms on *all* possible surface orientations and the correct treatment of vacancies and non-stoichiometric crystals. Such a model is beyond the scope of this investigation which aims at an understanding of the behaviour of reconstructed (001) surfaces. However, as we will show, a physically relevant model is not possible within the limits of the solid-on-solid condition.

To find a reasonable compromise between the complexity of a fully three-dimensional model and the limits of a strict solid-on-solid model, we permit the occupation of Cd sites by Te atoms and the binding of Te atoms to single Cd atoms *on the surface*, while the incorporation of point defects into the *bulk* of the crystal is forbidden. Then we can treat those atoms which stay in the correct sublattice and have at least two chemical bonds to atoms in the layer below in a solid-on-solid manner, while the weakly bound Te atoms are considered separately.

First, we study the behaviour of this model in vacuum and under a flux of pure Cd or pure Te. In particular, we show that a reasonable choice of model parameters yields semi-quantitative agreement with experiments. Then, we perform simulations of atomic layer epitaxy and compare our results with those of experimental investigations of CdTe by means of this growth technique.

4.1 The zinc-blende lattice

In this section, we present a solid-on-solid representation of the zinc-blende lattice. A sketch of its unit cell is shown in figure 2.1. We use cartesian coordinates where the x -axis points in the $[110]$ direction, the y -axis points in the $[1\bar{1}0]$ direction and the z -axis points in the $[001]$ direction which is perpendicular to the (001) surface. The origin of the coordinate system is at the centre of a Te atom. If the zinc-blende lattice is projected onto the x - y plane in the z -direction, the image positions of all atoms lie on a square lattice (figure 4.1). Measuring the lattice constant in appropriate units, the images of Te atoms are at positions $(2i, 2j)$ and $(2i + 1, 2j + 1)$ in the x - y plane where $i, j \in \mathbb{Z}$. The images of Cd atoms are at positions $(2i, 2j + 1)$ and $(2i + 1, 2j)$ with integer i, j . This square lattice is used as the basis of our

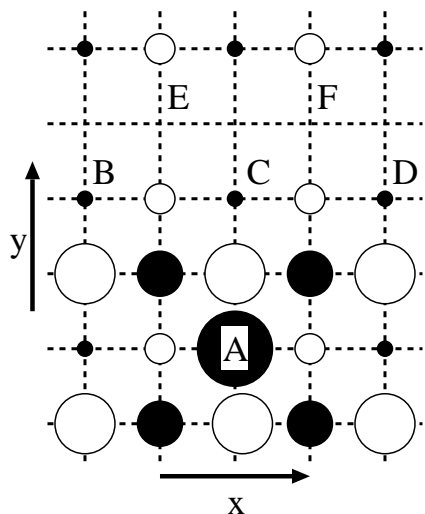


Figure 4.1: The zinc-blende lattice lattice seen from the $[001]$ direction. The figure shows a Te terminated surface with a step in the x -direction. Cd atoms are shown as filled circles, Te atoms as open circles. The size of the atoms corresponds to their z -coordinate: the higher the atom, the larger the circle.

solid-on-solid representation of the zinc-blende (001) surface, which is described by a two-dimensional $2L \times 2N$ array h of integers. $h_{x,y}$ is the maximal z -coordinate of the column of atoms whose images are at (x,y) , measured in units of the spacing between a Cd and a Te layer. In the following, for simplicity we will loosely denote any atom whose image is at (x,y) as “atom at (x,y) ” and $h_{x,y}$ as “height of the atom at (x,y) ”.

An atom in the zinc-blende lattice may have at most 4 binding partners. Since the solid-on-solid condition forbids overhangs and vacancies, each atom must have at least two bonds to atoms of the opposite species in the layer below. Only atoms with exactly two bonds may be *removed* from the crystal without violating the solid-on-solid condition: An atom with 4 bonds is inside the bulk of the crystal. If we remove it, we create a vacancy. If we remove an atom with three bonds the atom in the layer above which is bound to it becomes an overhang. Atoms with only one bond form an overhang and do not exist in a solid-on-solid model. In the following, we will denote atoms which may be removed from the surface without violating the solid-on-solid condition as *mobile*. Similarly, an atom can be *deposited* only at a site where it has exactly two bonds. The deposition of an atom with only one bond creates an overhang. Empty sites where the deposition of an atom creates three or four bonds can exist only in the presence of overhangs or vacancies, which is not the case in a solid-on-solid model. In consequence, a *diffusion process* where an atom is removed from one site and deposited at another cannot change the number of chemical bonds in the system.

A Cd atom at (x,y) is bound to Te atoms at $(x,y \pm 1)$ in the layer below and can be bound to Te atoms at $(x \pm 1,y)$ in the layer above. The atom is mobile, if there are no bonds to Te atoms in the layer above, which is the case if $h_{x,y} > h_{x \pm 1,y}$. The neighbouring Cd atoms of a Te atom at (x',y') are at $(x' \pm 1,y')$ in the layer below and at $(x',y' \pm 1)$ in the layer above. Thus, the condition for mobility of a Te atom is $h_{x',y'} > h_{x',y' \pm 1}$.

An atom can be deposited at a site if the solid-on-solid condition is fulfilled and the atomic species matches the character of the site. At a Cd site at (x,y) , the solid-on-solid condition demands that $h_{x,y-1} = h_{x,y+1}$ and $h_{x,y} < h_{x,y \pm 1}$. A Te site at (x',y') can be occupied if $h_{x'-1,y'} = h_{x'+1,y'}$ and $h_{x',y'} < h_{x' \pm 1,y'}$. The deposition of an atom at (x,y) is performed by setting $h_{x,y} \leftarrow h_{x,y} + 4$. Similarly, setting $h_{x,y} \leftarrow h_{x,y} - 4$ removes the atom at (x,y) .

As discussed in section 2, the positions of the atoms in *one half-layer* of the zinc-blende lattice lie on a square lattice. However, this is not identical to the square lattice structure

of the solid-on-solid representation of the crystal lattice, as it is in the simple cubic model presented in chapter 3. The distance between nearest neighbours in the square lattice of one half-layer (denoted as *lateral neighbours* in the following) is *twice* the distance between neighbouring images of atoms in the projection of the whole crystal onto the x - y plane.

4.1.1 Desorption and adsorption

Due to the solid-on-solid condition, only mobile atoms may desorb. We consider the desorption of single atoms from the surface, neglecting the fact that in reality Te probably desorbs as a binary molecule from the CdTe surface. Similarly, we consider only the adsorption of single atoms via an incorporation process (section 1.4.1): First, the species of the atom and the landing site are chosen randomly. Then, we search for sites where the deposition of this atom is possible within an incorporation radius r_i around the landing site. The atom is deposited at the lowest site which has been found in that search. If two or more sites of equal height have been found, one of these sites is chosen randomly. If no appropriate site is found, the atom is reflected.

4.1.2 Diffusion

We consider an atom diffusing on a flat surface, for example a Cd atom on a Te terminated surface. For an atom at \vec{x}_0 , the nearest sites that can be occupied by an atom of its species are the lateral neighbour sites at $\vec{x}_0 + \Delta\vec{x}$, where the hopping vector $\Delta\vec{x}$ is an element of the set $\{(0, 2), (0, -2), (2, 0), (-2, 0)\}$. Similar to the model discussed in section 3 we consider also diffusion to lateral diagonal neighbour sites, i.e. $\Delta\vec{x} \in \{(2, 2), (2, -2), (-2, 2), (-2, -2)\}$.

However, a particle that can perform only these diffusion hops is not able to cross a step. We discuss this for the example of the Cd atom at site A in figure 4.1 diffusing downhill at a step in x -direction. It is not possible to deposit the atom at either of the sites B, C and D, since the condition $h_{x,y-1} = h_{x,y+1}$ is not fulfilled there. Similar considerations hold for other step orientations, diffusion uphill and for the diffusion of Te atoms. Thus there is an infinite Schwoebel barrier in a model in which only these diffusion hops are considered. Since we do not want to restrict ourselves in this special case, we introduce additional hopping vectors for diffusion. In figure 4.1, the nearest sites to site A at the lower side of the step that can be occupied by a Cd atom are E and F, which yield $\Delta\vec{x} = (1, 3)$ and $\Delta\vec{x} = (-1, 3)$. Extending these considerations to different step orientations, we obtain the set $\{(3, 1), (3, -1), (-3, -1), (-3, 1), (1, 3), (-1, 3), (1, -3), (-1, -3)\}$ of hopping vectors which are sufficient to permit the crossing of steps of one monolayer height difference oriented in arbitrary direction. To permit the crossing of steps higher than one monolayer, we would have to introduce additional hopping vectors. However, such high steps rarely occur in our simulations. Therefore, it is a reasonable approximation to neglect diffusion across high steps in order to reduce the complexity of the model. In summary, there are 16 hopping vectors for the diffusion of an atom. However, due to the conditions that must be fulfilled to permit the deposition of the atom at the landing site, at most 8 diffusion hops are allowed for a single mobile atom.

4.2 The Hamiltonian of the solid-on-solid model

The basic idea behind our model of the CdTe(001) surface is similar to that of the simple cubic crystal presented in chapter 3: besides the Cd-Te bond, there is an isotropic interaction between Cd atoms and between Te atoms on lateral nearest neighbour sites in the bulk. The interaction of Te atoms on the surface is identical to that of Te atoms in the bulk, i.e. we neglect the formation of Te dimers. The interaction of Cd atoms, however, depends strongly on whether they are mobile or incorporated into the crystal. Mobile Cd atoms interact with their lateral nearest neighbours and lateral diagonal neighbours with the interactions of the lattice gas model introduced in chapter 2.

4.2.1 The Cd-Te bond

There is a chemical bond between Cd and Te atoms on nearest neighbour sites. We assume that the total energy of these bonds is proportional to their number with an energy ε_c per bond. Since the strength of the interaction between atoms is a quickly decreasing function of their distance, we expect this energy to be the greatest part of the total binding energy of the crystal. To remove a mobile atom from the surface, two Cd-Te bonds have to be broken. This yields an energy barrier $\varepsilon_v = -2\varepsilon_c$ for the desorption of an atom in addition to contributions from other, weaker interactions.

As discussed in section 4.1, a diffusion process cannot change the total number of nearest neighbour bonds. Consequently, the strength of the Cd-Te bond does not influence the energy difference between the starting and the final state of the atom. In our model, the energy barrier a diffusing adatom must overcome is a separate parameter. It is smaller than the energy required to break up its bonds. Thus, the rates of diffusion processes are not a function of ε_c .

4.2.2 Interactions with lateral neighbours

Interactions with a longer range than nearest neighbour interactions are required to describe surface reconstructions and to ensure that the equilibrium surface at low temperature is flat.

It is a reasonable approximation to consider only interactions between particles in the same layer. In a solid-on-solid model, the environment of an atom in the vertical direction is always the same. Therefore, interactions of longer range with atoms in this direction will be always present as long as the atom remains on the surface. In case of desorption they may be treated as an additional contribution to ε_c .

We introduce an attractive interaction between atoms which are incorporated in the crystal, i.e. atoms with more than two bonds. An atom interacts with its lateral nearest neighbours and the strength of the interaction is isotropic. However, we allow a different strength for the attraction between Cd atoms ($\varepsilon_{Cd,b}$) and Te atoms ($\varepsilon_{Te,b}$).

We assume that the interaction between Te atoms is independent on whether they are incorporated in the crystal or mobile atoms on the surface and do not consider the dimerization of surface Te atoms. This simplification reduces the complexity of the model considerably. Mobile Cd atoms interact via the anisotropic interactions ε_x , ε_d and a hardcore repulsion between particles on lateral neighbour sites in the y -direction which were introduced in chapter 2. Additionally, we introduce an interaction $\varepsilon_{Cd,h}$ between mobile and incorporated Cd atoms which we assume to be isotropic.

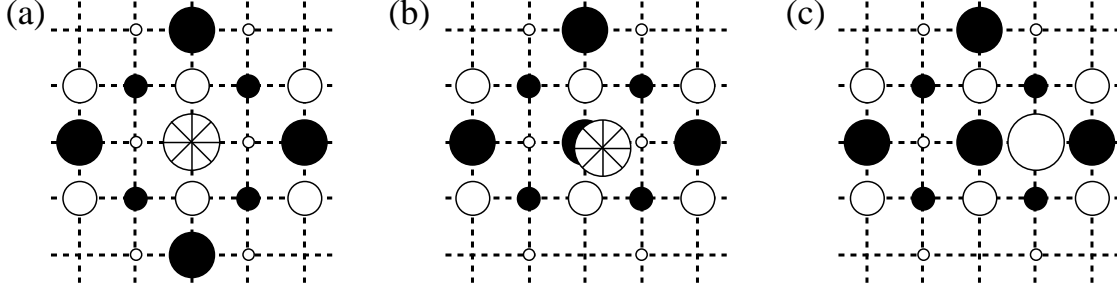


Figure 4.2: Deposition of a Te atom on a $c(2 \times 2)_{\text{Cd}}$ reconstructed surface via a Te^* state. The Te^* atom is shown as an open circle with a star inside.

In summary, the Hamiltonian of the solid-on-solid model is

$$H_{\text{SOS}} = \varepsilon_c n_c + \underbrace{\varepsilon_{\text{Cd},b} n_{\text{Cd},b} + \varepsilon_{\text{Te},b} n_{\text{Te},b} + \varepsilon_h n_{\text{Cd},h} + \varepsilon_x n_{\text{Cd},x} + \varepsilon_d n_{\text{Cd},d}}_{H_{\text{lat}}} \quad (4.1)$$

Here, n_c is the number of chemical bonds between Cd and Te atoms on nearest neighbour sites. $n_{\text{Cd},b}$ and $n_{\text{Te},b}$ are the numbers of pairs of incorporated Cd and Te atoms on lateral nearest neighbour sites. $n_{\text{Cd},h}$ is the number of mobile Cd atoms which are lateral nearest neighbours of incorporated Cd atoms. $n_{\text{Cd},x}$ and $n_{\text{Cd},d}$ are the numbers of pairs of mobile Cd atoms on lateral nearest neighbour sites in the x -direction and on lateral diagonal neighbour sites, respectively. In addition to these interactions we impose the constraint that the number $n_{\text{Cd},y}$ of mobile Cd atoms on nearest neighbour sites in the y -direction must always be zero.

4.3 Beyond the solid-on-solid condition

In the present state of our model, there is a violation of the ergodicity condition similar to the one discussed in section 3.1. Consider the surface configuration shown in figure 4.3a. Energetically, it is favourable to shift the small island by one lattice constant into the negative y -direction to obtain the configuration shown in figure 4.3e. However, it is not possible to construct a sequence of allowed single particle moves to do so. In chapter 3 we introduced the diffusion of AB molecules with B atoms on top to solve an analogous problem. The counterpart of this process on the zinc-blende lattice would be the diffusion of a cluster of two Cd atoms and one Te atom. Then, the small island in figure 4.3 could diffuse as a whole. However, this is not a general solution to the ergodicity problem. It is not possible to remove such a cluster from the edge of a greater Te terminated island without violating the solid-on-solid condition. There is at least one additional Te atom in the top layer of the island which is bound to a Cd atom in the cluster. If we remove the cluster, this atom becomes an overhang.

Additionally, in the present form of our model it is not possible to deposit an atom on a perfectly $c(2 \times 2)_{\text{Cd}}$ reconstructed surface. There are no sites which can be occupied by a Te atom without violating the solid-on-solid condition. The hardcore repulsion between mobile Cd atoms in the y -direction forbids a completion of the topmost Cd layer.

There is a solution to both of these problems which has the advantage of being consistent with an experimental observation made on CdTe: under a strong flux of Tellurium one finds

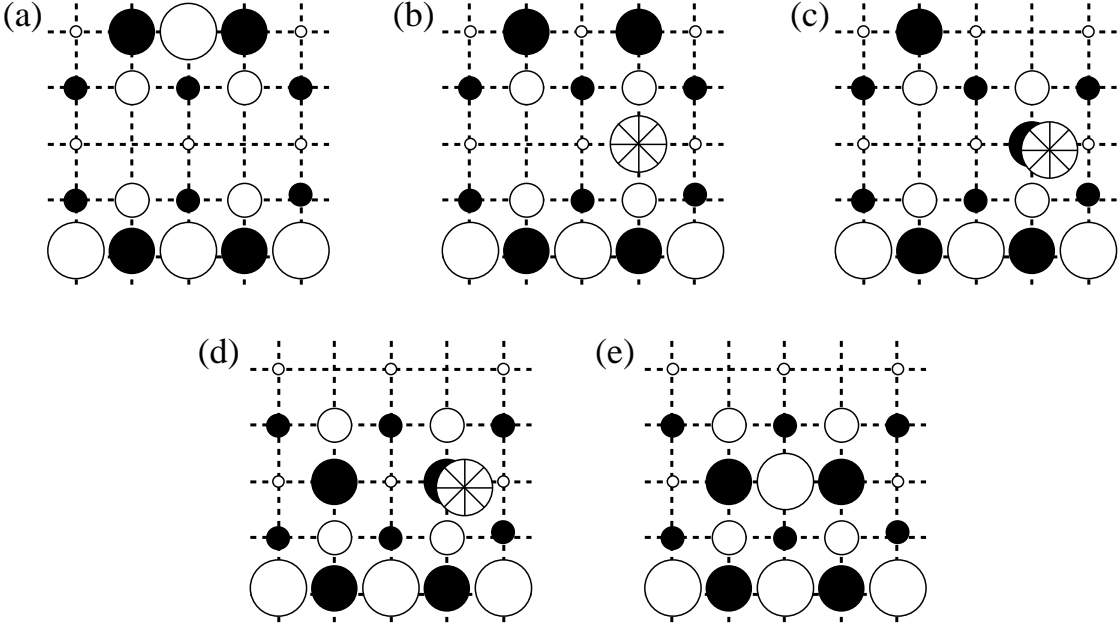


Figure 4.3: Coalescence of islands. The Te atom on top of the small island stays temporarily in a Te^* state.

surfaces with a Te coverage of $3/2$ and a (2×1) reconstruction (figure 2.3). This is explained by the formation of Te trimers which arrange in rows in the x -direction. A trimer is created if a Cd site on the surface is occupied by a Te atom. We consider this arrangement in our model. Additionally, we allow Te atoms which have only *one* bond to a Cd atom. In the following, we denote Te atoms in one of these configurations which both violate the solid-on-solid condition as Te^* atoms. It is not necessary to give up a solid-on-solid model in favour of a fully three-dimensional model to consider Te^* states if Te^* atoms may exist on the surface of the crystal but the incorporation of point defects into the crystal is forbidden. We describe the crystal by two two-dimensional $2L \times 2N$ arrays of integers, h and t . h represents those atoms which fulfil the solid-on-solid condition in the manner described in section 4.1. t represents the Te^* atoms. A Te^* atom at (x, y) corresponds to $t_{x,y} = 1$, otherwise $t_{x,y} = 0$.

The rules for Te^* atoms are the following:

1. Te^* atoms are allowed on sites with a mobile Cd atom (Te atoms with one bond to a Cd atom) and on sites where the deposition of a Cd atom would not violate the solid-on-solid condition (middle Te atom in a trimer). The coordinates of these sites correspond to Cd sites in the solid-on-solid model. Each site may be occupied by at most one Te^* atom.
2. Te^* atoms on different sites do not interact. The binding energy ε^* of a Te^* is independent on whether it is bound to two Te atoms or to one Cd atom.
3. Two laterally neighbouring sites in the y -direction may be occupied by two Cd atoms, if at least one of the sites is occupied by a Te^* atom. Thus, a Te^* atom neutralizes the hardcore repulsion between laterally neighbouring Cd atoms in the y -direction.

4. Atoms on the solid-on-solid surface which are mobile may diffuse or desorb even if they are binding partners of Te^* atoms. If a Te^* atom is on a site which may not be occupied by a Te^* atom any more after such a process (according to rule (1)), it is desorbed. Of course, the activation energy for the desorption of Te^* atoms has to be considered in the calculation of the rate of the process. Te^* atoms do not follow the motion of their binding partners.
5. Both the desorption of Te^* atoms and the deposition of Te atoms from an external particle beam in Te^* states are possible. If a Te atom is landing on the surface, in the incorporation process Te^* states within r_i are considered in addition to states in the solid-on-solid lattice. Te^* atoms may diffuse on the surface. We permit the same hopping vectors as for the diffusion of atoms on the solid-on-solid lattice.
6. Te atoms may change between states in the solid-on-solid lattice and Te^* states. This is a diffusion process where the Te atom hops between Te sites in the solid-on-solid lattice and Te^* sites, which have the coordinates of Cd sites in the solid-on-solid model. We consider the set

$$\{(1, 0), (-1, 0), (1, 2), (-1, 2), (1, -2), (-1, -2), (2, 1), (2, -1), (-2, 1), (-2, -1), (3, 0), (-3, 0), (0, 3), (0, -3)\}$$

of hopping vectors for this process.

Thus, the Hamiltonian of our model is

$$H = H_{lat} + \varepsilon_c n_c + \varepsilon^* n^*. \quad (4.2)$$

Here, H_{lat} is the contribution of the lateral interactions to the energy of the system. It has been defined in equation 4.1. n_c is the number of Cd-Te bonds in the solid-on-solid lattice. n^* is the number of Te^* atoms. Additionally, we consider only surface configurations where the number $n'_{Cd,y}$ of pairs of mobile Cd atoms without a Te^* atom on lateral neighbour sites in the y -direction is zero.

Now we show examples of the role of Te^* states in the deposition of a Te atom on a Cd terminated surface and the coalescence of islands. Figure 4.2 shows the deposition of a Te atom on a $c(2 \times 2)_{\text{Cd}}$ reconstructed surface. First, the atom is deposited in a Te^* state in one of the gaps of the $c(2 \times 2)_{\text{Cd}}$ reconstruction (figure 4.2a). According to rule (3), one of the neighbouring Cd atoms can diffuse into the gap (figure 4.2b). Following rule (4), now the Te^* atom is bound to that Cd atom. This process creates a site in the solid-on-solid lattice which can be occupied by a Te atom. In the last step, the Te^* atom diffuses to that site (figure 4.2c) following rule (6). Figure 4.3 shows the coalescence of islands. The Te atom on top of the small island stays temporarily in a Te^* state. Then, the two Cd atoms can diffuse to the step edge. Finally, the Te atom is deposited on the site in the solid-on-solid lattice provided by the Cd atoms.

The assumption of noninteracting Te^* atoms (rule (2)) is a simplification which has been introduced to make an investigation of this model computationally feasible. Considering interactions between the quickly diffusing Te^* atoms would lead to a considerable slowing down of the simulations. This simplification is justified if the density of Te^* is so low that the probability to find a partner to interact with is small. We will show that interactions between

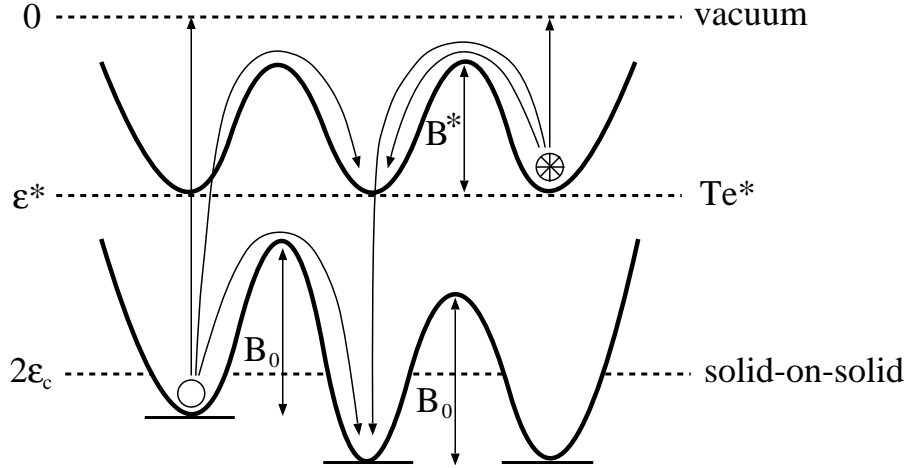


Figure 4.4: The potential energy surface of adatoms

Te* atoms should be considered to describe the behaviour of a surface under a strong flux of pure Te at low temperature.

A Te* atom which is bound to a Cd atom has three dangling bonds. As discussed in section 1.1, these bonds are negatively charged. It is plausible to assume that this compensates the energetically unfavourable concentration of positively charged Cd dangling bonds on a pair of neighbouring Cd atoms in the y -direction. This might justify rule (3) which has been introduced to make the landing of Te atoms on a perfectly $c(2 \times 2)_{\text{Cd}}$ reconstructed surface possible. Without rule (3), it would be impossible for a Cd atom to perform a diffusion process which provides a site in the solid-on-solid lattice that can be occupied by a Te atom.

In the set of hopping vectors introduced in rule (6), we have considered diffusion to those sites which have a smaller distance to the starting site than the final sites of a diffusion process within the same sublattice. These hopping vectors permit the crossing of steps with a height of one monolayer. We have omitted the hopping vectors $(0, 1)$ and $(0, -1)$, since due to the topology of the zinc-blende lattice it is never possible to deposit the atom on the final site of such a diffusion process.

4.4 The dynamics of adatoms

In our model, we assume Arrhenius rates (equation 1.2) for diffusion and desorption processes. To calculate the activation energy we assume the energy of the transition state between the starting and the final configuration of the system to be equal to the greater of the energies of both configurations plus an additional barrier height. Since atoms on the solid-on-solid surface are bound stronger than Te* atoms, it is reasonable to assume that the barrier height for diffusion of atoms on the solid-on-solid surface is greater than that for diffusion of Te* atoms. In our model, we use the simplest choice for the energy barriers of all processes that meets this condition. There is an equal barrier height B_0 for all diffusion hops of particles without lateral nearest neighbours and a barrier height B^* for the diffusion of Te* atoms. The barrier heights for the other processes are chosen such that the barriers for all moves of

one particle which do not increase the energy of the system are equal and detailed balance is fulfilled for diffusion processes.

This principle yields the following activation energies for diffusion on the solid-on-solid surface ($E_{s \rightarrow s}$), diffusion of Te^* atoms ($E_{* \rightarrow *}$), diffusion of a Te atom from a solid-on-solid state to a Te^* state ($E_{s \rightarrow *}$), diffusion of a Te^* atom into a solid-on-solid state ($E_{* \rightarrow s}$), desorption of an atom on the solid-on-solid surface ($E_{s \rightarrow v}$) and desorption of a Te^* atom ($E_{* \rightarrow v}$):

$$E_{s \rightarrow s} = \max\{B_0, B_0 + \Delta H\} \quad (4.3)$$

$$E_{* \rightarrow *} = \max\{B^*, B^* + \Delta H\} \quad (4.4)$$

$$E_{s \rightarrow *} = \max\{B_0, B^* + \Delta H\} \quad (4.5)$$

$$E_{* \rightarrow s} = \max\{B^*, B_0 + \Delta H\} \quad (4.6)$$

$$E_{s \rightarrow v} = \max\{B_0, \Delta H\} \quad (4.7)$$

$$E_{* \rightarrow v} = \max\{B^*, \Delta H\}. \quad (4.8)$$

Figure 4.4 shows a sketch of the energy barriers in our model.

In the following, we will focus on the parameter set $r_i = 2$, $\varepsilon_x = -1.95|\varepsilon_d|$, $\varepsilon_h = 0$, $\varepsilon_{Cd,b} = \varepsilon_{Te,b} = -0.8|\varepsilon_d|$, $\varepsilon_c = -6.5|\varepsilon_d|$, $\varepsilon^* = -3|\varepsilon_d|$, $B_0 = 9|\varepsilon_d|$ and $B^* = 2|\varepsilon_d|$. Since there is an attractive interaction between mobile Cd atoms on lateral diagonal neighbour sites, ε_d is necessarily negative. This choice of parameters is guided by the following principles: $\varepsilon_x = -1.95|\varepsilon_d|$ ensures that $c(2 \times 2)_{\text{Cd}}$ is energetically favourable compared to $(2 \times 1)_{\text{Cd}}$ and the difference between the surface energies of both reconstructions is small compared to the total surface energy. The parameters $\varepsilon_{Cd,b}$, $\varepsilon_{Te,b}$ and ε_h have been chosen such that we obtain a $c(2 \times 2)_{\text{Cd}}$ reconstruction under vacuum at low temperature. Our model of a flat surface in thermal equilibrium (chapter 2) indicates that $|\varepsilon_d|$ is slightly smaller than 0.1 eV. On the other hand, we expect the activation energy $2\varepsilon_c$ which is required for the desorption of a single adatom to be on the same order of magnitude as the macroscopic activation energy of sublimation. Experimentally, values between 0.96 eV and 1.95 eV have been measured [21, 73, 75] depending on particle species and mode of sublimation. Thus, $\varepsilon_c = -6.5|\varepsilon_d|$ seems to be a good guess. An adsorption of Te on a $c(2 \times 2)_{\text{Cd}}$ reconstructed surface via a Te^* state is possible only if Te^* atoms are not desorbed too fast such that ε^* must not be too small. The barrier for diffusion of a Te atom on the solid-on-solid surface should be smaller than that for diffusion into a Te^* state such that $B_0 < |2\varepsilon_c - \varepsilon^*|$. Finally, the diffusion barrier for a Te^* atom must be smaller than that for desorption of Te^* which implies $B^* < |\varepsilon^*|$. The prefactor of the Arrhenius rates has been set to $\nu = 10^{12}/\text{s}$ which has turned out to be a good choice for CdTe [73, 100].

The value of $|\varepsilon_d|$ sets the energy scale of the model which needs not to be specified if temperature is expressed by means of the dimensionless parameter $\Theta = kT/|\varepsilon_d|$. If we set $k = |\varepsilon_d| = 1$ like in the previous chapters, we have $\Theta = T$. In this chapter, we will determine $|\varepsilon_d|$ in physical units by identifying the temperature of the $c(2 \times 2)_{\text{Cd}}-(2 \times 1)_{\text{Cd}}$ transition with the experimental value. As we will show, this yields activation energies for sublimation which are on a reasonable order of magnitude.

4.5 Characterization of the surface

In principle, the methods applied for the characterization of the surface of this model follow the ideas introduced in chapters 2 and 3. Note however, that there is an important difference

between the simple cubic lattice and the zinc-blende lattice: In our representation of the zinc-blende lattice, the distance between lateral nearest neighbours in one half-layer is two unit lengths. The positions of atoms in each CdTe monolayer are shifted by one unit length both in the x - and in the y -direction compared to the atoms in the layer below or above. Thus, the pattern of a surface reconstruction cannot be continued across a step as it is possible in the simple cubic lattice. Consequently, it is not possible to define the order parameter $M_{Cd}^{(2 \times 2)}$ of the whole system in analogy to the planar lattice gas. Similarly, this effect hinders a calculation of correlation lengths with the method introduced in section 3.2. Therefore, we restrict ourselves to an investigation of the short-range correlations K_{Cd}^x and K_{Cd}^d .

To calculate these, we define a $2L \times 2N$ array of integers c , where $c_{i,j} = 1$ if there is a *mobile* Cd atom at (i, j) and zero otherwise. In terms of these variables, we have

$$K_{Cd}^d := \frac{1}{2\rho_{Cd}NL} \sum_{i,j=1}^{2L,2N} c_{i,j} (c_{i+2,j+2} + c_{i+2,j-2}) \quad (4.9)$$

$$K_{Cd}^x := \frac{1}{\rho_{Cd}NL} \sum_{i,j=1}^{2L,2N} c_{i,j} c_{i+2,j} \quad (4.10)$$

where $\rho_{Cd} = (LN)^{-1} \sum_{i,j=1}^{2L,2N} c_{i,j}$ is the density of mobile Cd atoms on the surface.

4.6 Sublimation

Qualitatively, the behaviour of a surface under vacuum is quite similar to that observed in our model of a simple cubic crystal with surface reconstructions presented in section 3.

On a flat surface sublimating in layer-by-layer mode, the correlations K_{Cd}^x and K_{Cd}^d oscillate (figure 4.5). Like in the simple cubic model, island boundaries induce a preferential arrangement of Cd atoms in rows such that there is a maximum of K_{Cd}^x whenever the surface width W is large and a maximum of K_{Cd}^d whenever the surface is flat.

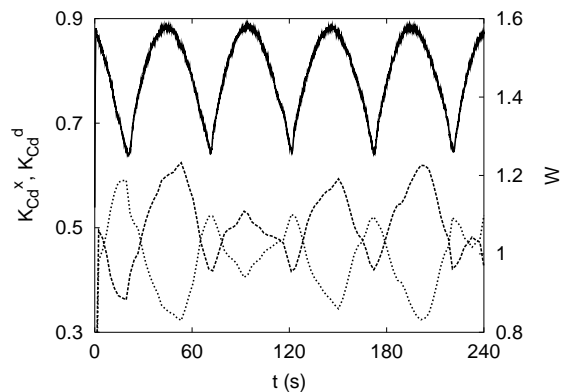


Figure 4.5: Surface width W (solid) and correlations K_{Cd}^x (dashed), K_{Cd}^d (dotted) during the sublimation of a flat surface at $\Theta = 0.525$ which corresponds to $T = 525$ K in physical units. For clarity of plotting, the curves of the correlations have been smoothed; W shows the natural fluctuations. The system size is $L = N = 64$.

Figure 4.6a shows the correlations K_{Cd}^x , K_{Cd}^d and the Cd coverage ρ_{Cd} as functions of temperature in the stationary state of step flow sublimation. The steps are parallel to the $[100]$ direction and have a distance of 16 lattice constants. In the investigated temperature range, ρ_{Cd} is close to 0.5. It decreases slightly from $\rho_{Cd} = 0.49$ at $\Theta = 0.45$ to $\rho_{Cd} = 0.43$

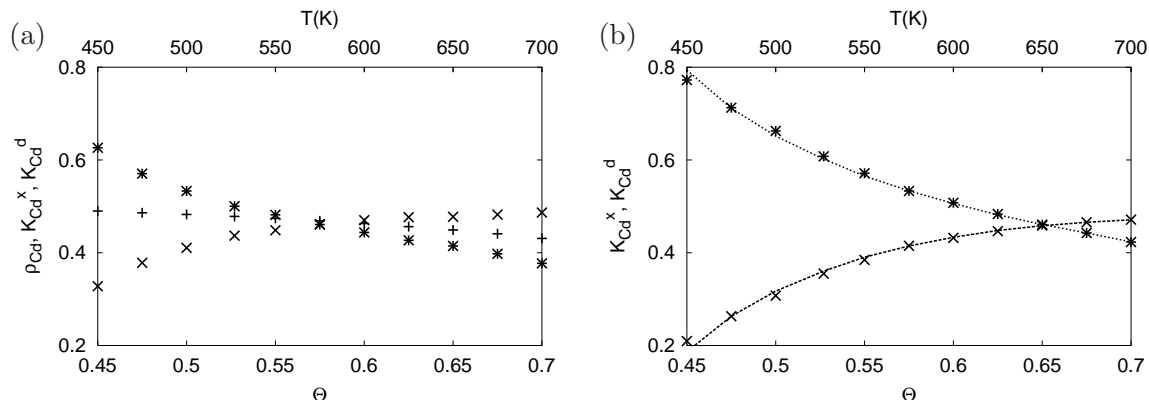


Figure 4.6: Panel (a): Stationary values of ρ_{Cd} ($+$), K_{Cd}^x (\times) and K_{Cd}^d ($*$) in step flow sublimation. Shown are time averages of these quantities which have been measured during the sublimation of 5 monolayers. Additionally, averages over 3 independent simulation runs have been performed. Panel (b): Equilibrium values of these quantities in the planar lattice gas in thermal equilibrium. The symbols show results of canonical Monte Carlo simulations at the values of ρ_{Cd} which are found on sublimating surfaces. $10^4 \cdot LN$ events have been performed both for equilibration and for measurement. The lines show results of a transfer matrix calculation at a strip width $L = 16$. The chemical potential μ has been adjusted to obtain the desired value of ρ_{Cd} . In both Monte Carlo simulations, the system size is $L = N = 64$.

at $\Theta = 0.7$. At low temperature, the Cd atoms arrange preferentially in a $c(2 \times 2)_{Cd}$ order. At high temperature, the Cd atoms prefer to arrange in rows which are characteristic of the $(2 \times 1)_{Cd}$ reconstruction. The crossover between both regimes where $K_{Cd}^x = K_{Cd}^d$ is at $\Theta = 0.57$.

We compare the values of K_{Cd}^x and K_{Cd}^d which are found on the sublimating surface with those measured in the planar lattice gas introduced in section 2.2.4 at the same temperature and Cd coverage. We find, that the nonequilibrium conditions of sublimation enhance the tendency of Cd atoms to arrange in rows. At all temperatures, in step flow sublimation we find greater (smaller) values of K_{Cd}^x (K_{Cd}^d) than on a flat surface in thermal equilibrium. An inspection of surface snapshots shows, that at low temperature the $c(2 \times 2)_{Cd}$ reconstructed surface is divided into domains which are elongated in the y -direction. Thus, there is no long range order in the lattice gas of Cd atoms on one terrace. These observations parallel our findings in the simple cubic model. Consequently, the ideas about reconstruction order on sublimating surfaces developed in section 3 are valid also in the more complicated model presented in this chapter.

We set the energy scale of our model by identifying $\Theta = 0.57$ where $K_{Cd}^x = K_{Cd}^d$ with the experimental value of ≈ 570 K [21, 75] for the temperature of the transition between $c(2 \times 2)_{Cd}$ and $(2 \times 1)_{Cd}$. Then, we have $T = \Theta \cdot 1000$ K which corresponds to $\varepsilon_d = -0.0862$ eV.

Given the parameter set in physical units, we check its physical relevance by comparing activation energies of sublimation processes with the corresponding experimental values. A Te terminated surface decays in a temperature-dependent time interval τ which corresponds to a sublimation rate $r_{Te} = 1/\tau$. The measurement of sublimation rates in stoichiometrical evaporation is done straightforward by counting the number of desorbed particles. It is convenient to plot the logarithm of the sublimation rate versus $1/T$. In this representation

which is denoted as *Arrhenius plot*, the data points lie on a straight line if the dependence of the sublimation rate on temperature is given by an Arrhenius law.

Figure 4.7 shows that this is the case both for $r_{\text{Te,step}}$ and for the rate r_{step} at which CdTe evaporates stoichiometrically in step flow mode. The corresponding activation energies are $E_{\text{Te,step}} = 1.23 \text{ eV}$ and $E_{\text{step}} = 1.43 \text{ eV}$. Experimentally, values of $E_{\text{Te,step}} = 0.96 \text{ eV}$ [119] and $E_{\text{step}} = 1.54 \text{ eV}$ [75] have been found. In layer-by-layer sublimation, the agreement of the data with an Arrhenius law is as good as in step flow sublimation. We find an activation energy $E_{\text{layer}} = 1.50 \text{ eV}$ which is smaller than the experimental value 1.94 eV [73]. The activation energy for the decay of the Te-terminated surface in layer-by-layer sublimation is $E_{\text{Te,layer}} = 1.35 \text{ eV}$. Surprisingly the difference between E_{step} and E_{layer} is quite small. From the quality of the fits of simulation data with an Arrhenius law, we estimate the accuracy of the values of the activation energies to about $\pm 0.02 \text{ eV}$. For the attempt frequencies, we obtain values on the order of magnitude of $10^{12}/\text{s}$. In general, the deviation of our values of the activation energies from the experimental results is less than 30%. This shows that our model parameters are at least in a physically reasonable region of the parameter space.

At present, an optimization of model parameters to obtain better agreement with experiments does not make much sense. First, the experimental data are insufficient for a systematical fit of the nine parameters in our model and there are no values of diffusion barriers available from ab initio or at least semi-empirical calculations. Therefore, any parameter set will be partly based on estimates and physical reasoning. Second, our model still contains several important simplifications like a neglecting of Te dimerization and interactions between Te^* atoms. Additionally, we have made a comparatively simple ansatz for the potential energy surface. Therefore, a perfect agreement with experiments is not expected.

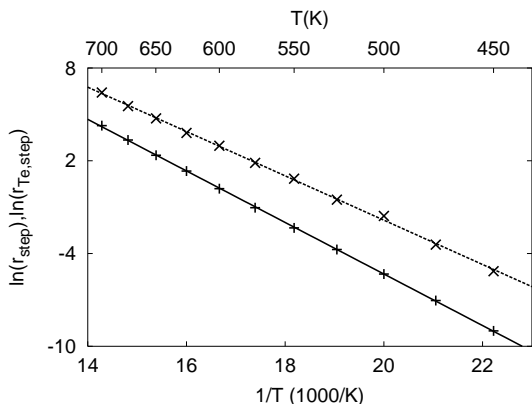


Figure 4.7: Arrhenius plot of the sublimation rate in step-flow mode (+) and the rate at which the initial Te terminated surface decays (\times). These data have been obtained in the simulation runs shown in figure 4.6a. The lines show fits with an Arrhenius law.

4.7 Surfaces under an external particle flux

Figure 4.8a shows the Cd coverage and the correlations K_{Cd}^x , K_{Cd}^d on a stepped surface which is exposed to a flux of pure Cd or pure Te at $T = 500 \text{ K}$. Under vacuum, the Cd atoms arrange preferentially in a $c(2 \times 2)_{\text{Cd}}$ pattern at this temperature. A Te flux decreases the Cd coverage of the surface. The remaining Cd atoms arrange preferentially in rows. Thus, the behaviour of our model at low ρ_{Cd} agrees qualitatively with that of the planar lattice gas in thermal equilibrium. Of course, this is what we expect in analogy to the simple cubic model introduced in section 3.

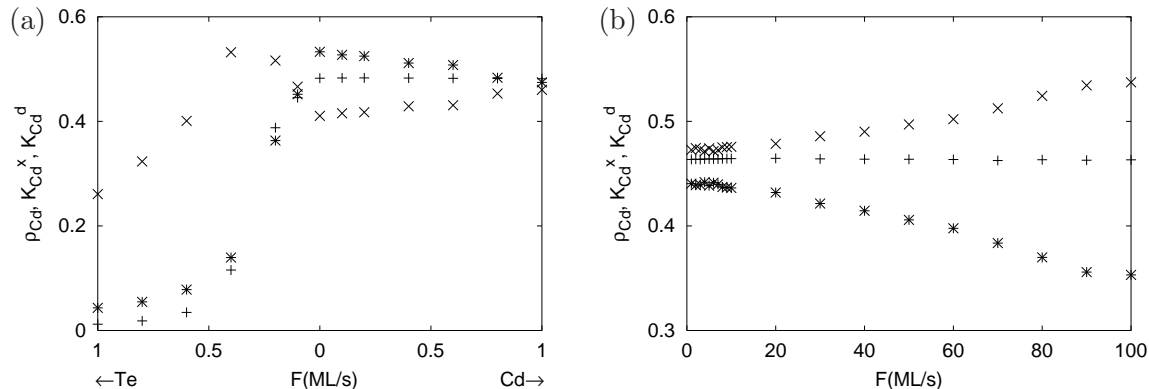


Figure 4.8: ρ_{Cd} (+), K_{Cd}^x (\times) and K_{Cd}^d (\ast) on stepped surfaces with a terrace width of 16 lattice constants under an external particle flux. The system size is $L = N = 64$. Panel (a): $T = 500$ K. The simulation shows time averages over 140s of simulated time after a relaxation phase of 140s. Panel (b): $T = 600$ K. The surface is exposed to a flux of pure Cd. Time averages have been performed over 7s of simulated time after a relaxation phase of equal length.

However, a Cd flux does not increase the tendency of the Cd atoms to arrange in a checkerboard pattern as it is the case for the A atoms in the simple cubic model. For Cd fluxes smaller than ≈ 0.6 ML/s, the correlations K_{Cd}^x and K_{Cd}^d remain almost constant. At greater Cd flux, K_{Cd}^x increases and K_{Cd}^d decreases. A similar behaviour is found at $T = 600$ K where $K_{Cd}^x > K_{Cd}^d$ under vacuum (figure 4.8b). For Cd fluxes smaller than 10 ML/s, K_{Cd}^x and K_{Cd}^d remain close to their vacuum values. A greater Cd flux leads to an increase of K_{Cd}^x .

Surprisingly, there is no significant difference in the Cd coverage between a surface in vacuum and a surface which is exposed to an external Cd flux. If we determine the equilibrium values of K_{Cd}^x and K_{Cd}^d in the two-dimensional lattice gas at the values of ρ_{Cd} which are measured on a surface under a Cd flux, we obtain values which are almost identical to those found at the ρ_{Cd} of a surface in vacuum. This agrees qualitatively with the result that on a surface of a three-dimensional crystal which is exposed to a small Cd flux K_{Cd}^x and K_{Cd}^d are close to the values which are measured in vacuum. However, the increase of K_{Cd}^x under a large Cd flux cannot be understood within the framework of a qualitative agreement of our model with the two-dimensional lattice gas.

On the zinc-blende lattice, Cd atoms can be deposited only at sites where they are bound to two Te atoms in the layer below. This implies, that the maximum possible density of mobile Cd atoms on a stepped surface is smaller than 0.5. The exact value depends on the shape of the steps. Therefore, the fact that we measure $\rho_{Cd} < 0.5$ does not imply that there are many sites where an additional Cd atom can be deposited. If the density of such sites is small, an additional Cd flux cannot increase ρ_{Cd} further such that there is no reason for the mobile Cd atoms on the surface to arrange preferentially in a checkerboard pattern. This might explain why the behaviour of our model deviates from experiments which show that a Cd flux stabilizes the $c(2 \times 2)_{Cd}$ reconstruction at high temperature.

We expect a different behaviour if the dimerization of Te atoms in the terminating layer is considered. In a dimer, there is a chemical bond between two Te atoms which might also be the binding partners of a Cd atom in the layer above. Consequently, dimers are sites where

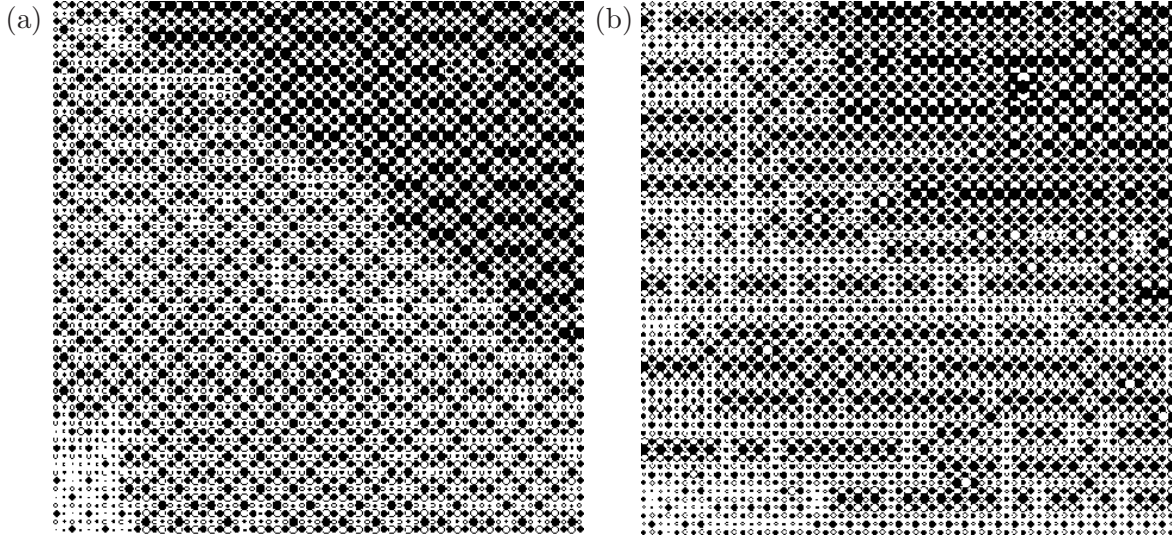


Figure 4.9: Sections of $16\sqrt{2} \times 16\sqrt{2}$ lattice constants of surfaces which have been exposed to a flux of pure Cd for 280 s at $T = 500$ K. Panel (a): $F = 0.6$ ML/s. Panel (b): $F = 10$ ML/s. Cd atoms are shown as filled circles, Te atoms as open circles. Greater circles denote greater values of $h_{i,j}$.

a Cd atom from a particle beam can be deposited. The binding energy of a dimer stabilizes the Te atoms with respect to desorption. Therefore, we expect that there are dimers on a surface sublimating under vacuum at high temperature if the binding energy of dimers is large enough. Such a surface is probably similar to the disordered phase of the planar lattice gas with Te dimerization introduced in chapter 2 (figure 2.7e). Under a Cd flux, Cd atoms are incorporated into the dimers which leads to an increase of ρ_{Cd} . This makes the Cd atoms arrange preferentially in a $c(2 \times 2)_{Cd}$ pattern.

The morphology of a surface under a small Cd flux is similar to that of a surface in vacuum. An example is shown in figure 4.9a. At large Cd flux, the morphology changes. In figure 4.9b, we show a snapshot of a surface which is exposed to a Cd flux of 10 ML/s at $T = 500$ K. The terraces are not flat. Instead, there is a network of grooves with a depth of one CdTe monolayer which run across the surface. The edges of the grooves are (111), $(1\bar{1}1)$, $(\bar{1}11)$ and $(\bar{1}\bar{1}1)$ facets. Between the grooves, there are ridges which consist of long rows of Cd atoms which are parallel to the x -direction. These rows yield the extremely large values of $K_{Cd}^x \approx 0.8$ which are measured on such a surface. Consequently, the increase of K_{Cd}^x on surfaces under a strong flux of Cd is induced by a faceting of the crystal surface.

At low temperature, the increase of K_{Cd}^x which accompanies the formation of grooves and ridges occurs at a smaller flux (0.6 ML/s at 500 K) than at high temperature (10 ML/s at 600 K). This indicates that under a small flux faceting is suppressed by the thermally activated diffusion of particles which smoothens the surface. A quantitative estimate confirms this consideration. We assume that the onset of faceting occurs at a fixed ratio between the Cd flux and the rate at which adatoms diffuse. In our model, the latter is given by an Arrhenius law with the energy barrier defined in equation 4.3. Attractive interactions between particles in one layer are small compared to B_0 . Therefore, B_0 is a good approximation for the typical

energy barrier of a diffusing atom. This yields a ratio of 20 for the fluxes where facetting begins at $T = 600$ K and $T = 500$ K which agree well with the results of our simulations.

The facetting of surfaces of II-VI compounds under an excess of one constituent has also been observed in experiments. In [129] it is reported that the (001) surface of ZnSe is facetting if it is exposed to a mixed particle beam with a large ratio of Zn to Se. The critical ratio between Zn and Se increases with temperature.

4.8 Atomic layer epitaxy

Atomic layer epitaxy (ALE) is used frequently in the fabrication of semiconductor heterostructures and has been applied successfully to determine the stoichiometry of the surface reconstructions of CdTe and other II-VI semiconductors. Thus, it provides a scenario for the investigation of our model in a situation present in technical applications and permits a direct comparison of computer simulations with experiments. As explained in the introductory section 1.6, the basic idea of ALE is to obtain self-regulated growth by alternate deposition of pure Cd and Te. In the absence of reconstructions, one would expect the formation of complete half-layers of Cd and Te during deposition of the elements such that in each cycle one CdTe monolayer is grown. However, this is not necessarily the case in the presence of surface reconstructions where the number of atoms in the terminating layer of the crystal is different from that in a layer inside the bulk.

In CdTe experimental investigations of the ALE growth rate v_g , i.e. the number of CdTe monolayers deposited per cycle have shown that it decreases in subsequent plateaus as temperature is increased [21, 27, 35]. Within large temperature intervals, v_g is almost constant. At temperatures below ≈ 510 K, CdTe grows at a speed of 1 ML/cycle. In the temperature interval $530 \text{ K} \leq T \leq 640 \text{ K}$ growth rates which are slightly lower than 0.5 ML/cycle have been found. At $T > 700$ K, ALE growth is not possible at all.

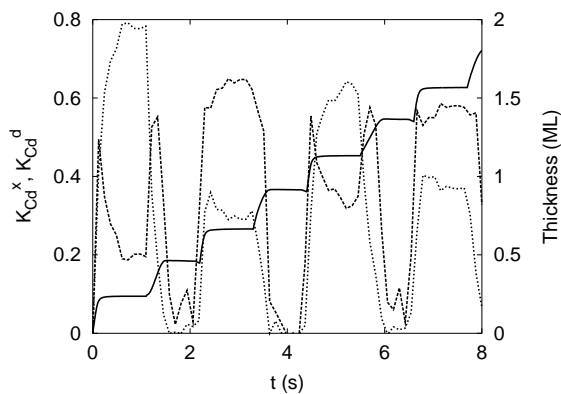


Figure 4.10: Thickness of the deposited layer (solid), K_{Cd}^x (dashed) and K_{Cd}^d (dotted) as functions of time in atomic layer epitaxy at $T = 500$ K. Pulse time and dead time are $t_p = 1$ s and $t_d = 0.1$ s. The particle flux during the pulses is 5 ML/s. The system size is $L = N = 128$. For clarity of plotting, the curves of K_{Cd}^x and K_{Cd}^d have been smoothed.

Since experiments [123] indicate that ALE growth proceeds in layer-by-layer mode, we focus on simulations of flat surfaces. Figure 4.10a shows the evolution of ρ_{Cd} , K_{Cd}^x and K_{Cd}^d during ALE at $T = 500$ K. The initial configuration is a flat Te terminated surface. In the first phase, a Cd flux of 5 ML/s is applied for a pulse time $t_p = 1$ s, followed by a dead time $t_d = 0.1$ s. In the second phase, Te is deposited with the same flux and identical parameters t_p and t_d . This cycle is repeated permanently. Snapshots of the surface during ALE growth are shown in figure 4.11.

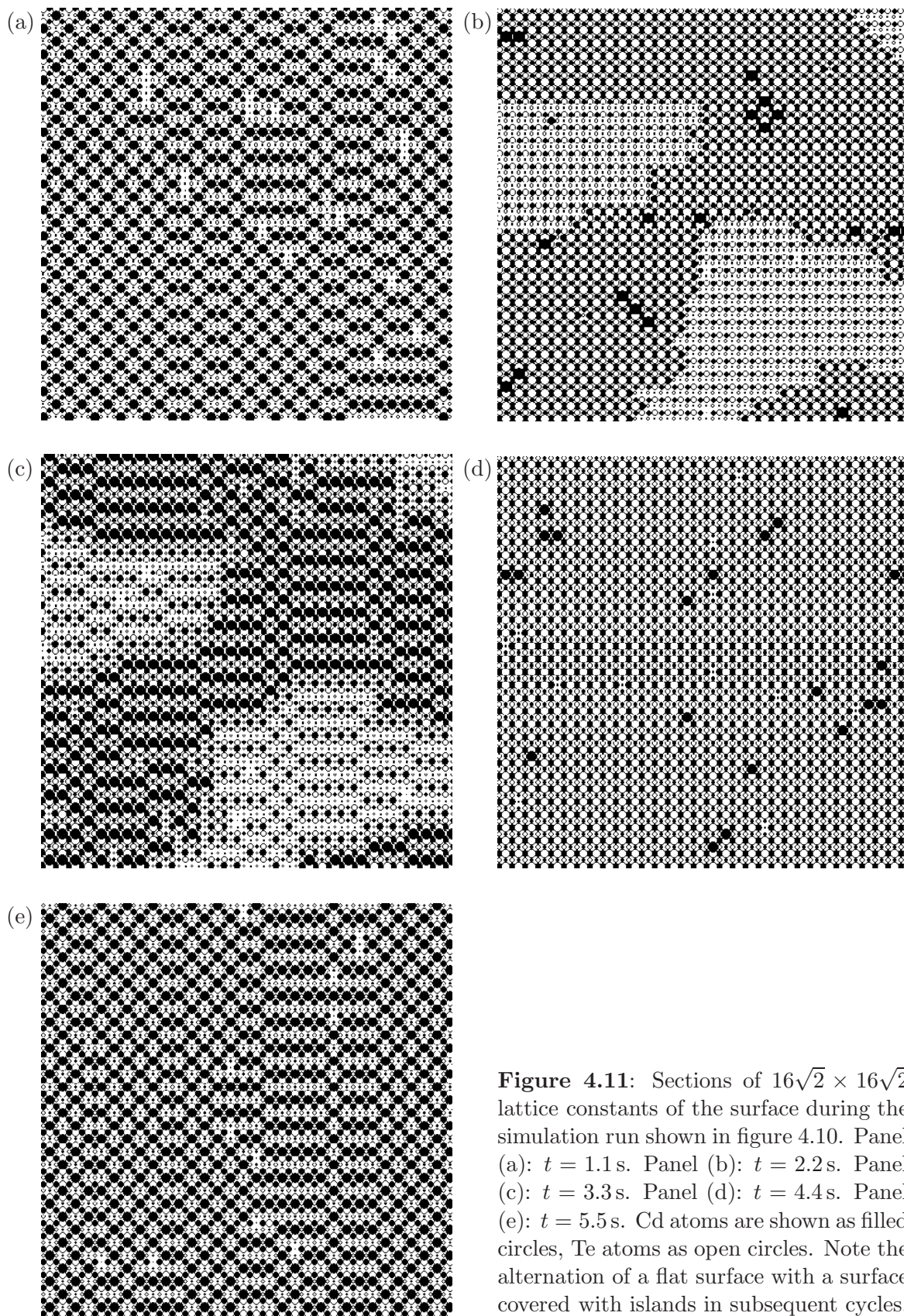


Figure 4.11: Sections of $16\sqrt{2} \times 16\sqrt{2}$ lattice constants of the surface during the simulation run shown in figure 4.10. Panel (a): $t = 1.1$ s. Panel (b): $t = 2.2$ s. Panel (c): $t = 3.3$ s. Panel (d): $t = 4.4$ s. Panel (e): $t = 5.5$ s. Cd atoms are shown as filled circles, Te atoms as open circles. Note the alternation of a flat surface with a surface covered with islands in subsequent cycles.

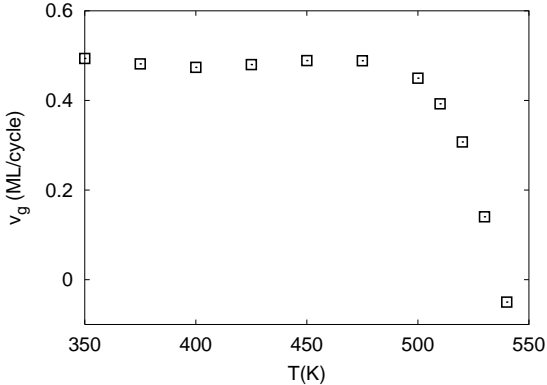


Figure 4.12: Temperature dependence of the growth rate in ALE on a flat surface. v_g has been determined from the increase of $\langle h_{i,j} \rangle$ in cycles 2–4. Apart from T , all parameters are identical to the simulation shown in figure 4.10.

The first Cd pulse creates a Cd terminated surface with $\rho_{Cd} \approx 1/2$ (figure 4.11a). Since T is below the $c(2 \times 2)_{Cd} - (2 \times 1)_{Cd}$ transition, the dominant reconstruction is $c(2 \times 2)_{Cd}$. At the onset of the Te phase, ρ_{Cd} decreases rapidly. This leads to an increase of K_{Cd}^x since at low Cd coverages it is energetically favourable for the remaining Cd atoms to arrange in rows. At the end of the cycle, approximately 50% of the surface are covered with Te terminated islands (figure 4.11b). The formation of a closed layer is impossible since only one half of the Cd atoms needed for a complete monolayer are present on the surface. The following Cd phase deposits half a monolayer of Cd again (figure 4.11c). However, now the reconstruction is preferentially $(2 \times 1)_{Cd}$. This is due to the influence of the island edges on the reconstruction and analogous to the maximum of K_{Cd}^x we observe in layer-by-layer sublimation after half a monolayer has desorbed. During the following Te phase, Cd atoms from the terminating layer of the islands and newly deposited Te atoms diffuse into the gaps between the islands which leads to the formation of an almost complete Te terminated surface (figure 4.11d). In the next Cd phase, a $c(2 \times 2)_{Cd}$ reconstructed flat surface is created and the whole process repeats (figure 4.11e). Thus, at the end of the odd cycles, the surface is rough, i.e. covered with islands, whereas at the end of the even cycles the surface is atomically flat. In our simulations the alternation of a rough and a flat surface can be traced during 3–4 cycles. There are two effects which keep it from repeating infinitely. First, we obtain a growth rate of 0.45 ML/cycle which is smaller than the ideal value of 0.5 ML/cycle. Second, the diffusion of particles from the islands into the gaps is not complete. Both effects hinder a perfect closure of a monolayer at the end of the even cycles which leads to a damping of the characteristic behaviour.

These observations closely resemble the ideas developed to explain CdTe growth at a speed of ≈ 0.5 ML/cycle in [27]. Figure 4.12 shows v_g as a function of temperature. For $350 \text{ K} \leq T \leq 500 \text{ K}$, growth proceeds at a speed of about 0.5 ML/cycle. If temperature is increased further, v_g decreases quickly. Thus, our model is also capable of reproducing the experimental observation of plateaus in $v_g(T)$.

There are two differences between our computer simulations and experimental results. First, in experiments the plateau of ALE growth at 0.5 ML/cycle extends to considerably higher temperatures than in our model. Second, our model does not reproduce growth at a speed of one monolayer per cycle at low temperature.

An inspection of the surface shows, that the breakdown of ALE at high temperature is mainly due to the quick evaporation of Te atoms during the Te phase. On the contrary, surfaces under a Cd flux appear to be comparatively stable. A simple consideration confirms

this picture. We expect a surface under a flux F of the particle species which terminates the reconstruction to be stable if the sublimation rate r_{sub} is smaller than F . If sublimation is an Arrhenius activated process with macroscopic activation energy E_{sub} and attempt frequency ν_{sub} , the temperature T_{inst} where $r_{\text{sub}} = F$ is given by

$$T_{\text{inst}} = -\frac{E_{\text{sub}}}{k \ln(F/\nu_{\text{sub}})}. \quad (4.11)$$

Inserting the activation energy and the corresponding prefactor for the decay of a flat Te-terminated surface, we obtain $T_{\text{inst}} = 570$ K which is close to the temperature 540 K at which v_g becomes zero. The experimental value of $T_{\text{inst}} = 700$ K [35] corresponds to an activation energy of ≈ 1.6 eV¹. Thus, the deviation from our value of 1.35 eV is about 20%. While this deviation might be cured by a tuning of model parameters, our considerations indicate an inconsistency between different experiments. Clearly, the fact that ALE is possible at temperatures above 600 K is incompatible with an activation energy as low as 0.96 eV for the decay of the Te terminated surface which has been measured in [119] unless an unphysically low attempt frequency $\sim 10^7$ /s is assumed.

The observation of a growth rate of 1 ML/cycle has been explained with the formation of a surface reconstruction with a Te coverage of 3/2 in the Te phase. Here, one half of the potential Cd sites on the surface are occupied by Te* atoms. In the following Cd phase, these particles are bound to newly deposited Cd atoms where they provide sites which can be occupied by additional Cd atoms. Thus, in each cycle a complete CdTe monolayer is deposited in spite of the hard repulsion between Cd atoms on neighbouring sites in the y -direction.

This effect can occur only if Te* atoms on a Te terminated surface are bound strong enough such that the rate of desorption of Te* is smaller than the particle flux. Since there is no interaction between Te* atoms in our model, macroscopical attempt frequency and activation energy are identical to the microscopical model parameters. Inserting these in equation 4.11, we find that a layer of Te* atoms on the surface is stable at $T < 116$ K which is far below ALE growth temperatures. Simulations confirm this result. Conversely, the experimental ALE data and equation 4.11 yield an activation energy of 1.28 eV for the decay of a surface terminated by Te trimers. This high value indicates that there are attractive interactions between trimers. On the other hand, there must be also repulsive interactions which stop the Te coverage from becoming greater than 3/2. Thus, a consistent description of ALE growth at comparatively low temperature probably requires the introduction of anisotropic interactions between Te trimers.

For completeness, we have also performed simulations of ALE on a stepped surface. At a terrace width of 16 lattice constants ALE growth proceeds in step flow mode. We find, that the growth rate v_g is identical to that found in ALE on a flat surface. However, there is no alternation between a rough and a flat surface in subsequent cycles. The deposited particles are captured by step edges and no islands are created. Therefore, we find a dominance of a $c(2 \times 2)_{\text{Cd}}$ arrangement in all Cd phases.

4.9 Summary and discussion

In summary, we have presented a model of growth and sublimation of CdTe(001) which might be an important step towards a realistic model of this surface. We have introduced an

¹Since T_{inst} depends on $\ln(F/\nu_{\text{sub}})$, variations of particle flux and attempt frequency within a physically reasonable range have small effects.

efficient representation of the (001) surface of the zinc-blende lattice. On the one hand, the great advantage of a solid-on-solid model to allow for a two-dimensional representation of a three-dimensional crystal is preserved. On the other hand, it is possible to consider overhangs and atoms in the wrong sublattice as long as these are not incorporated into the crystal. The reconstructions of the Cd terminated surface are considered in a way which is inspired by the ideas developed in sections 2 and 3. Simulations of this model show, that a physically reasonable parameter set yields a rough quantitative agreement with experiments.

To the best of our knowledge, we have performed the first simulations of atomic layer epitaxy. Our results show that it is possible to investigate the influence of surface reconstructions on this important growth process by means of Monte Carlo simulations. Additionally, a comparison of the ALE growth rate as a function of temperature between simulations and experiments should be useful to fit model parameters.

However, there are still some open questions. (1) What is the role of Te dimers on a non-equilibrium crystal surface? The lattice gas model of a flat CdTe(001) surface in thermal equilibrium (chapter 2) suggests that Te dimerization might be important, in particular at low ρ_{Cd} . As discussed in section 4.7, the dimerization of Te atoms might lower the Cd coverage of surfaces sublimating under vacuum at high temperature. This should lead to an increase of ρ_{Cd} and K_{Cd}^d and to a decrease of K_{Cd}^x under an external Cd flux. Experiments indicate that the Cd coverage under vacuum is indeed smaller than the values which we find in our simulations. In [75] $\rho_{Cd} \approx 0.35$ has been measured at the temperature of the crossover between dominant $c(2 \times 2)_{Cd}$ and dominant $(2 \times 1)_{Cd}$. As discussed in section 2.3, this would correspond to a coexistence of a $c(2 \times 2)_{Cd}$ and a $(2 \times 1)_{Te}$ phase on the surface in vacuum. (2) Our model does not reproduce ALE growth at a speed of one ML/cycle at low temperature. As discussed in section 4.8, an understanding of this feature requires the consideration of interactions between Te trimers. Experiments have shown, that trimers arrange in rows parallel to the x -direction yielding a (2×1) reconstruction[21, 119]. There are no trimers on nearest neighbour sites in the y -direction which can be understood from the electron counting rule (section 1.1). This suggests a modelling by means of an attractive interaction between trimers on neighbouring sites in the x -direction and a hard repulsion between trimers on neighbouring sites in the y -direction. However, it is questionable whether the simulation of such a model is computationally feasible. Since Te^* atoms are comparatively weakly bound, the diffusion of Te^* atoms is fast. This leads to a dramatical slowing down of the simulations if there is a high density of Te^* on the surface. Itoh et. al. [45, 46] faced a similar problem in the simulation of epitaxial growth of GaAs(001) where there is a high density of weakly bound As_2 molecules. They solved it by treating all As_2 states as one homogeneous particle reservoir without distinguishing between different arrangements of the molecules. In our model, a similar treatment of the Te^* atoms should be possible. The basic idea is to assume that the diffusion of Te^* atoms is so fast that the probability of a Te^* atom to interact with a given atom on the solid-on-solid surface does not depend on its history. Then, it is a reasonable approximation to assume that there is an equal density of Te^* atoms above each site on the solid-on-solid surface. Interactions between Te^* atoms might be treated in a mean field manner by assuming that the binding energy of a Te^* atom depends on the total number of Te^* atoms in the reservoir.

Chapter 5

Singularity spectra and dynamic scale invariance of kinetically rough surfaces

The past decade has raised much theoretical research in the subject of *kinetic roughening* of surfaces during growth. The investigation of this effect promises deep insight into statistical physics far from thermal equilibrium, see e.g. [12] for an overview. As discussed in section 1.5.1, this process creates surfaces which have fractal properties on lengthscales smaller than the correlation length $\xi(t)$.

We focus on a solid-on-solid model with a simple cubic lattice structure and nearest neighbour interactions only. The surface is represented by a two-dimensional array h of integers $h_{x,y}$ which denote the height of the column of atoms at (x, y) . The rates of thermally activated processes are given by the Arrhenius law 1.2. Energy barriers are determined by the number of bonds which must be broken to remove the particle from its initial site.

Atoms may diffuse to nearest neighbour sites. The rate of such a process is $\nu \exp(-(\varepsilon_b + n\varepsilon_n)/(kT))$, where ε_b and ε_n are the binding energies of a particle to the substrate and to its n nearest neighbours in the same layer. ν is the attempt frequency, and kT has its usual meaning. On each site, new particles are deposited with a rate F . There is no incorporation process. In contrast to earlier investigations of similar models [23], we permit the *desorption* of particles from the surface with rates $\nu \exp(-(\varepsilon_v + n\varepsilon_n)/(kT))$, where $\varepsilon_v > \varepsilon_b$. Simulations of this model are performed by means of the continuous time algorithm which is introduced in appendix B. Clearly, such a simple model neglects many effects which are present in real materials. On the other hand, it captures the essential features of processes which occur on unreconstructed surfaces in the absence of a Schwoebel barrier. Therefore, it is adequate to obtain insight into fundamental properties of the roughening process which are not specific to a particular material.

Recently, Arnéodo et. al. [7, 8, 29, 96] have suggested a method for the investigation of fractal and multifractal surfaces which uses the continuous wavelet transform. This is superior to the structure function approach which has to date solely been used in the analysis of models of epitaxial growth. In this chapter, we use the wavelet method for a precise characterization of kinetically rough surfaces. In particular, we investigate the influence of desorption on the surface morphology. We show that our model fulfils the dynamic scale invariance which was introduced in section 1.5.3. We relate the dynamic exponents α , β with the static scaling properties of the multifractal surface. We conclude with some remarks on the question of universality of scaling exponents.

5.1 Anomalous scaling and multiscaling

Originally, it was believed that the scaling properties of kinetically rough surfaces can be understood within the framework of Family-Vicsek scaling. Then, the properties of the surface are invariant under the dynamic scale transformation 1.9. On lengthscales smaller than $\xi(t)$ the surface is self-affine. Its Hurst exponent equals the dynamic exponent α . Under these conditions, the scaling properties of the surface are characterized completely by the two exponents α and $\beta = \alpha/z$. These are assumed to be universal, i.e. independent of model parameters.

Different methods have been suggested to measure α and β in computer simulations. Frequently, β is measured from the increase of the surface width with time, $W(t) \propto t^\beta$ (equation 1.11). Since α characterizes both the static scaling properties of the surface at fixed time and the dynamic scaling properties, there are two fundamentally different approaches to determine its value. The *static* approach investigates the height-height correlation function $G(\vec{l}, t)$ at fixed time t . For small $l := |\vec{l}|$, from equation 1.5 we expect it to increase $\sim l^{2\alpha}$. The *dynamic*¹ approach analyzes the dependence of the *surface width* W_{sat} in the saturation regime on the system size N : According to equation 1.14, we have $W_{\text{sat}}(N) \sim N^\alpha$. An alternative method uses equation 1.12: α and z are chosen such that the curves of $G(\vec{l}, t)/l^{2\alpha}$ versus $l/t^{1/z}$ collapse on a unique function u within a large range of t and l .

However, a careful analysis of simulation data [11, 23, 24, 57] has shown that several models of epitaxial growth show significant deviations from this simple picture. First, frequently one obtains significantly different exponents from the static and the dynamic approach. This phenomenon is commonly denoted as *anomalous scaling*. Second, a powerlaw behaviour of $G(\vec{l}, t)$ for small $|\vec{l}|$ does not necessarily imply that the surface is self-affine. The standard approach to test for self-affinity considers the height-height correlation functions of order q

$$\Gamma(q, \vec{l}, t) := \left\langle \left| f(\vec{x}, t) - f(\vec{x} + \vec{l}, t) \right|^q \right\rangle_{\vec{x}}, \quad (5.1)$$

which are generalizations of $G(\vec{l}, t) \equiv \Gamma(2, \vec{l}, t)$. Here, $f(\vec{x}, t)$ is the reduced surface height $h(\vec{x}, t) - \langle h(\vec{x}, t) \rangle$. On a self-affine surface we expect $\Gamma(q, \vec{l}, t) \sim l^{\gamma_q}$ for small l , where $\gamma_q = \alpha$ for all q . However, sometimes one encounters the phenomenon of *multiscaling*: the initial powerlaw behaviour of $\Gamma(q, \vec{l}, t)$ yields a hierarchy of q -dependent exponents γ_q .

These observations can be interpreted within the mathematical framework of *multifractality*. The *Hölder exponent* [7, 10, 12, 72] $\chi(\vec{x}_0)$ of a function f at \vec{x}_0 is defined as the largest exponent such that there exist a polynomial of order $n < \chi(\vec{x}_0)$ and a constant C which yield $|f(\vec{x}) - P_n(\vec{x} - \vec{x}_0)| \leq C|\vec{x} - \vec{x}_0|^{\chi(\vec{x}_0)}$ in the neighbourhood of \vec{x}_0 . The Hölder exponent characterizes *local* symmetry properties of the surface. In the vicinity of \vec{x}_0 , we have

$$f(\vec{x}_0 + b\vec{l}, t) - f(\vec{x}_0, t) \sim b^{\chi(\vec{x}_0)} \left[f(\vec{x}_0 + \vec{l}, t) - f(\vec{x}_0, t) \right].$$

Thus, the Hölder exponent is a local counterpart of the Hurst exponent: a self-affine function with Hurst exponent H has $\chi(\vec{x}) = H$ everywhere. However, in the case of a *multiaffine* function different points \vec{x} might be characterized by different Hölder exponents. In this case, the surface consists of interwoven fractal sets of points where there is one particular Hölder exponent. This general case is characterized by the *singularity spectrum* $D(\chi)$, which denotes the Hausdorff dimension of the set of points where χ is the Hölder exponent of f .

¹In the literature (e.g. [60, 62, 63, 91]) the static and the dynamic approach are frequently denoted as “local” and “global” approach, respectively.

5.2 The wavelet approach to multifractality

There is a deep analogy between multifractality and thermodynamics [12, 105, 125], where the Hölder exponents play the role of energy, the singularity spectrum corresponds to entropy, and q plays the role of inverse temperature. So, theoretically $D(\chi)$ might be calculated via a Legendre transform of γ_q : $D(\chi) = \min_q(q\chi - q\gamma_q + 2)$ [7, 10, 72], a method which has been called *structure function* (SF) approach. However, its practical application raises fundamental difficulties: First, to obtain the complete singularity spectrum, one needs γ_q for positive *and* negative q . But as $|f(\vec{x}, t) - f(\vec{x} + \vec{l}, t)|$ might become zero, $\Gamma(q, \vec{x}, t)$ is in principle undefined for $q < 0$. Therefore, only the left, ascending part of $D(\chi)$ is accessible to this method. Additionally, the results of the SF method can easily be corrupted by polynomial trends in $f(\vec{x})$ [10]. It might be due to these difficulties, that—to our knowledge—no attempt to determine the singularity spectrum of *growing surfaces* from γ_q has ever been made. On the basis of simulations of several simple growth models, it has been argued that the γ_q might collapse onto a single γ in the limit $t \rightarrow \infty$, which characterizes the asymptotic universality class of the model [23, 24, 26]. This would imply that multiscaling is a finite size effect. However, there is no physical reason why this should be the case. A precise measurement of $D(\chi)$ will help to test this hypothesis.

To this end, we follow the strategy suggested by Arnéodo et. al. [7, 10, 121], which circumvents the problems of the SF approach and permits a reliable measurement of the complete singularity spectrum. Mathematically, the wavelet transform of a function $f(\vec{x})$ of two variables is defined as its convolution with the complex conjugate of the wavelet $\psi(\vec{x})$ which is *dilated* with the *scale* a and rotated by an angle θ [121]:

$$T_\psi[f](\vec{b}, \theta, a) = C_\psi^{-1/2} a^{-2} \int d^2x \psi^*(a^{-1} \mathbf{R}_{-\theta}(\vec{x} - \vec{b})) f(\vec{x}). \quad (5.2)$$

Here \mathbf{R}_θ is the usual 2-dimensional rotation matrix, and $C_\psi = (2\pi)^2 \int d^2k |\vec{k}|^{-2} |\hat{\psi}(\vec{k})|^2$ is a normalization constant, whose existence requires square integrability of the wavelet $\psi(\vec{x})$ in fourier space. Apart from this constraint, the wavelet can (in principle) be an arbitrary complex-valued function. Introducing the wavelet $\psi_\delta(\vec{x}) = \delta(\vec{x}) - \delta(\vec{x} + \vec{n})$, where \vec{n} is an arbitrary unit vector, one obtains easily

$$\begin{aligned} T_{\psi_\delta}[f](\vec{b}, \theta, a) &= C_{\psi_\delta}^{-1/2} \left[f(\vec{b}) - f(\vec{b} + a \mathbf{R}_\theta \vec{n}) \right] \\ &\Rightarrow \int d^2b \left| T_{\psi_\delta}[f](\vec{b}, \theta, a) \right|^q \propto \Gamma(q, a \mathbf{R}_\theta \vec{n}). \end{aligned} \quad (5.3)$$

Consequently, a calculation of the moments of the wavelet transform of the surface yields the SF approach as a special case. To avoid its weaknesses, two major improvements are necessary.

First, we use a class of wavelets with a greater number of *vanishing moments* $n_{\vec{\Psi}}$ than $\psi_\delta(\vec{x})$. Then, the wavelet is orthogonal to any polynomial of degree less than $n_{\vec{\Psi}}$. This increases the range of accessible Hölder exponents and improves the insensitivity to polynomial trends in $f(\vec{x})$. We introduce a two-component version of the wavelet transform

$$\vec{T}_{\vec{\Psi}}[f](\vec{b}, a) = \frac{1}{a^2} \int d^2x \begin{pmatrix} \Psi_1(a^{-1}(\vec{x} - \vec{b})) \\ \Psi_2(a^{-1}(\vec{x} - \vec{b})) \end{pmatrix} f(\vec{x}), \quad (5.4)$$

where the components Ψ_1, Ψ_2 of the analyzing wavelet $\vec{\Psi}$ are defined as partial derivatives of a radially symmetrical convolution function $\Phi(\vec{x})$: $\Psi_1(\vec{x}) = \partial\Phi/\partial x$, $\Psi_2(\vec{x}) = \partial\Phi/\partial y$. Then $\vec{T}_{\vec{\Psi}}[f](\vec{b}, a)$ can be written as the gradient of $f(\vec{x})$, smoothed with a filter Φ with respect to \vec{b} . This definition becomes a special case of equation 5.2, when multiplied with $\vec{n}_\theta = (\cos(\theta), \sin(\theta))^\top$, yet allows for an easier numerical computation². For example, Φ can be a gaussian, where $n_{\vec{\Psi}} = 1$, or $\Phi_1(\vec{x}) = (2 - \vec{x}^2) \exp(-\vec{x}^2/2)$ which has two vanishing moments.

Second, the integration over \vec{b} in equation 5.3 is undefined for $q < 0$, since the wavelet coefficients might become zero. The basic idea is to replace it with a discrete summation over an appropriate partition of the wavelet transform which takes on nonzero values only, but preserves the relevant information on the Hölder regularity of $f(\vec{x})$. In the following, we give a brief outline of the rather involved algorithm and refer the reader to [7, 10, 121] for more details and a mathematical proof.

The *wavelet transform modulus maxima* (WTMM) are defined as local maxima of the modulus $M_{\vec{\Psi}}[f](\vec{b}, a) := |\vec{T}_{\vec{\Psi}}[f](\vec{b}, a)|$ in the direction of $\vec{T}_{\vec{\Psi}}[f](\vec{b}, a)$ for fixed a . If $\Phi(\vec{x})$ is the gaussian function, the computation of their positions is equivalent to the detection of edges in image processing [65, 66]. Similarly, for arbitrary wavelets the WTMM lie on connected curves which trace structures of size $\sim a$ on the surface. The strength of each curve is characterized by the *maximal* value of $M_{\vec{\Psi}}[f](\vec{b}, a)$ along the line, the so-called *wavelet transform modulus maxima maximum* (WTMMM) [7]. While proceeding from large to small a , successively smaller structures are resolved. Connecting the WTMMM at different scales yields the set \mathcal{L} of maxima lines l , which lead to the locations of the singularities of $f(\vec{x})$ in the limit $a \rightarrow 0$. The partition functions

$$Z(q, a) = \sum_{l \in \mathcal{L}(a)} \left(\sup_{(\vec{b}, a') \in l, a' \leq a} M_{\vec{\Psi}}[f](\vec{b}, a') \right)^q \sim a^{\tau(q)} \quad \text{for } a \rightarrow 0 \quad (5.5)$$

are defined on the subset $\mathcal{L}(a)$ of lines which cross the scale a . From the analogy between the multifractal formalism and thermodynamics, $D(\chi)$ is calculated via a Legendre transform of the exponents $\tau(q)$ which characterize the scaling behaviour of $Z(q, a)$ on small scales a : $D(\chi) = \min_q (q\chi - \tau(q))$. Additionally, $\tau(q)$ itself has a physical meaning for some q : $-\tau(0)$ is the fractal dimension of the set of points where $h(\vec{x}) < \infty$, while the fractal dimension of the surface $f(\vec{x})$ itself equals $\max(2, 1 - \tau(1))$.

5.3 Results

In our simulations, we choose the parameters $\nu = 10^{12}$ s, $\varepsilon_b = 0.9$ eV, $\varepsilon_n = 0.25$ eV, and a temperature $T = 450$ K. To study the influence of desorption, we consider three models with different activation energies ε_v : in model A desorption is forbidden, i.e. $\varepsilon_v = \infty$. Models B and C have $\varepsilon_v = 1.1$ eV and $\varepsilon_v = 1.0$ eV. We simulate the deposition of $2 \cdot 10^4$ monolayers at a growth rate of one monolayer per second on a lattice of $N \times N$ unit cells using periodic boundary conditions, our standard value being $N = 512$. To check for finite size effects, we have also simulated $N = 256$. In all presented results averages over 6 independent simulation runs have been performed. Snapshots of the surface in a simulation of model A are shown in figure 5.1. Visually, surfaces of models B and C look quite similar.

²For simplicity, the irrelevant constant $C_{\vec{\Psi}}$ has been omitted.

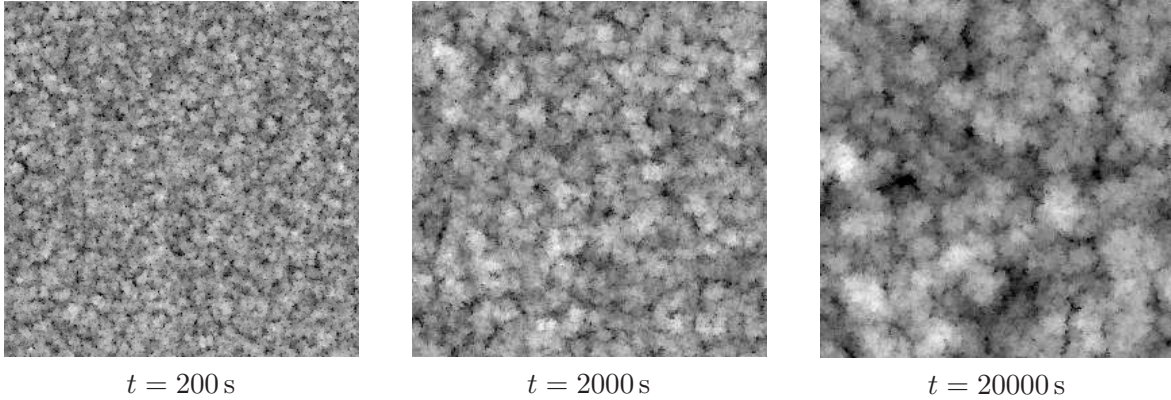


Figure 5.1: Evolution of the surface in a simulation run of model A. Brighter shades of grey denote greater surface heights.

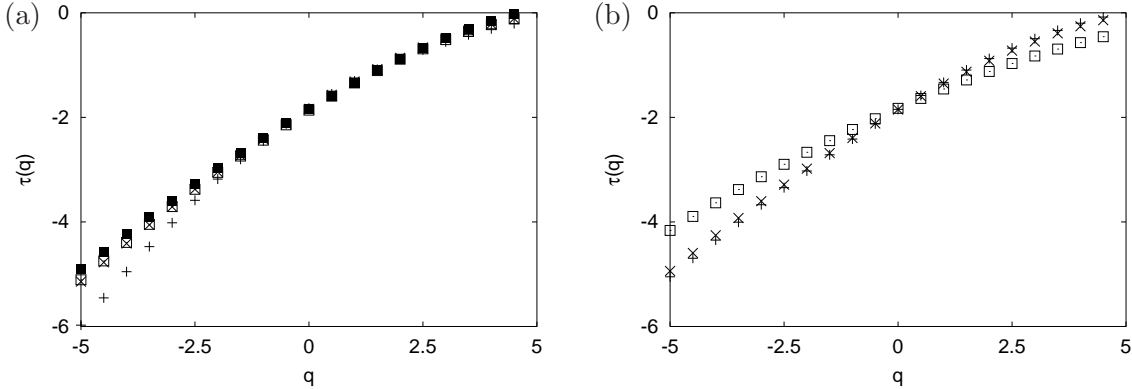


Figure 5.2: Panel (a): $\tau(q)$ in model A as obtained from investigations with wavelets derived from the filters Φ_0 (+), Φ_1 (\times), Φ_2 (\square) and Φ_3 (\blacksquare). Note the deviations of the data obtained with the gaussian function Φ_0 . Panel (b): $\tau(q)$ for models A (+), B (\times) and C (\square). All data have been obtained from surfaces after $2 \cdot 10^4$ s of simulated time. Sizes of errorbars are on the order of symbol sizes.

5.3.1 Singularity spectra

First, we have checked our results for artifacts resulting from properties of the analyzing wavelet rather than the analyzed surface by using different convolution functions Φ_n : Φ_0 is the gaussian function, $\Phi_n, n \geq 1$ are products of gaussians and polynomials which have been chosen in a way that the first n moments vanish. Then, the analyzing wavelets have $n_{\bar{\psi}} = n + 1$ vanishing moments. We find (figure 5.2a), that the $\tau(q)$ -curve obtained with Φ_0 deviates significantly from those obtained with Φ_1 , Φ_2 and Φ_3 . The latter agree apart from small differences which are mainly due to the discrete sampling of the wavelet in the numerical implementation of the algorithm. This is explained by the theoretical result [72] that $d\tau(q)/dq = n_{\bar{\psi}}$ for $q < q_{\text{crit.}} < 0$ if the number of vanishing moments of the analyzing wavelet is too small. Consequently, the agreement of the other curves proves their physical relevance.

Figure 5.2b shows averages of $\tau(q)$ curves obtained with the convolution functions Φ_1 , Φ_2 ,

Φ_3 from surfaces after $2 \cdot 10^4$ s of growth on an initially flat substrate. For all our models, their nonlinear behaviour reflects the multifractal surface morphology. From the fact that these curves are reproduced within statistical errors in simulations with $N = 256$ we conclude that finite size effects can be neglected. Clearly, desorption reduces the slope of $\tau(q)$, although only a small fraction of the incoming particles is desorbed: 0.18% in model B and 2.57% in model C with slightly higher values at earlier times. The corresponding singularity spectra are shown

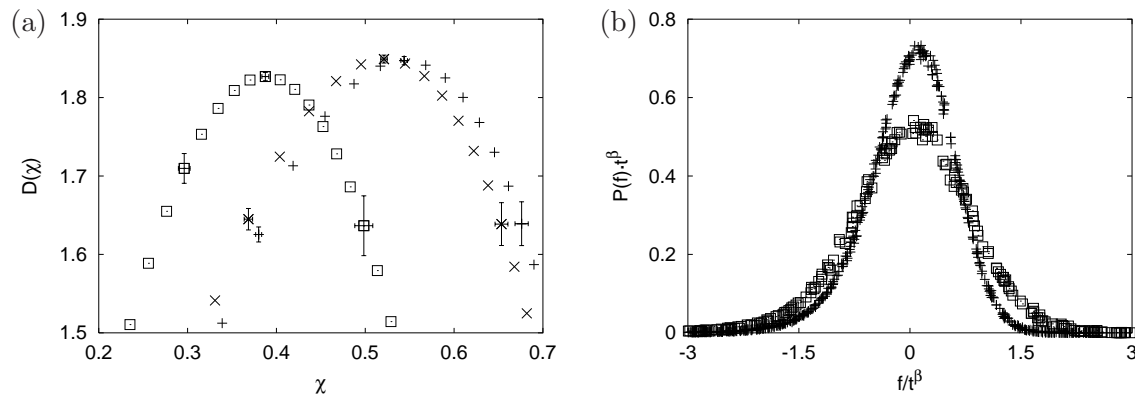


Figure 5.3: Panel (a): Singularity spectra obtained from a Legendre transform of the data in figure 5.2b. Panel (b): Data collapse of rescaled PDFs of surface heights for times between 150 s and $2 \cdot 10^4$ s (model A) respectively 150 s and 7500 s (model C). The corresponding scaling exponents are summarized in table 5.1. Time is measured in seconds. In both panels, the symbol + represents results of model A, × corresponds to model B and □ denotes results of model C. Model B which is not shown in panel (b) yields a data collapse of similar quality as model A.

in figure 5.3a. They have a typical shape whose descending part seems to be symmetrical to the ascending part and which changes at most slightly, while the whole spectra are shifted towards smaller Hölder exponents as desorption becomes more important. We emphasize that we find no evidence for a *time dependence* of the singularity spectra within the range $9700 \text{ s} \leq t \leq 2 \cdot 10^4 \text{ s}$, such that our results do *not* support the idea of an asymptotic regime which is governed by Family-Vicsek scaling. However, the accessible time range of computer simulations is limited, so we cannot finally disprove the existence of such a regime.

5.3.2 The relation between static and dynamic scaling properties

In Family-Vicsek scaling, we have $H = \alpha$ such that the scaling exponent of a static surface is identical to one of the dynamic exponents. The multifractal formalism has replaced the unique Hurst exponent H of a self-affine surface with a wide spectrum of Hölder exponents. This raises the question whether the analogy between static and dynamic scaling behaviour holds also in the presence of multiscaling such that there is a distribution of dynamic scaling exponents. Alternatively, it is possible that multiscaling affects only the properties of static surfaces while dynamic scaling is governed by two unique exponents α and β .

To answer this question, we need a reliable method to decide whether the properties of the surface are invariant under the transformation 1.9. To this end, we investigate the probability distribution function (PDF) $P_f(f, t)$ of the reduced surface height. Invariance under dynamic

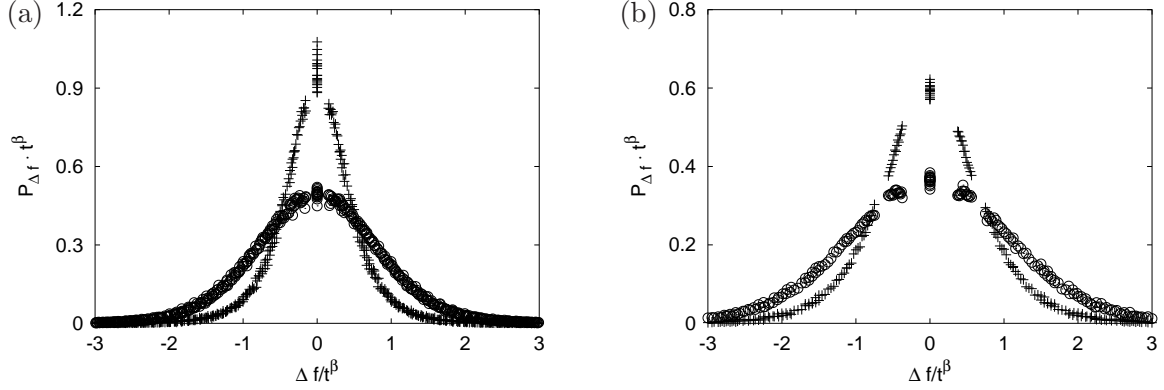


Figure 5.4: Data collapse of $P_{\Delta f}$. Panel (a) shows data from model A in the time range $150 \text{ s} \leq t \leq 2 \cdot 10^4 \text{ s}$ at $l/t^{1/z} = 0.33$ (+) and $l/t^{1/z} = 8.42$ (\odot). In panel (b), we show results for model C within the time range $150 \text{ s} \leq t \leq 7500 \text{ s}$ at $l/t^{1/z} = 0.63$ (+) and $l/t^{1/z} = 15.1$ (\odot). The data collapse is good apart from small lattice effects at $\Delta f = 0$. Model B yields results similar to model A. In all results shown, the vector \vec{l} is parallel to the x -direction.

scaling implies that $P_f(b^\alpha f, b^z t) d(b^\alpha f) = P_f(f, t) df$. This is fulfilled if

$$P_f(f, t) = \frac{1}{t^\beta} p_f \left(\frac{f}{t^\beta} \right). \quad (5.6)$$

Consequently, within a large time range the rescaled PDFs $P_f t^\beta$ should collapse onto a single function p_f if they are plotted as a function of f/t^β . Additionally, we consider the PDF $P_{\Delta f}(\Delta f, \vec{l}, t)$ of the height increment at a distance \vec{l} , $\Delta f := f(\vec{x}, t) - f(\vec{x} + \vec{l}, t)$. Similar to equation 5.6, we obtain

$$P_{\Delta f}(\Delta f, l, t) = \frac{1}{t^\beta} p_{\Delta f} \left(\frac{\Delta f}{t^\beta}, \frac{\vec{l}}{t^{1/z}} \right). \quad (5.7)$$

Therefore, in a large time range one should obtain a data collapse if $t^\beta P_{\Delta f}$ is plotted versus $\Delta f/t^\beta$ and the ratio $\vec{l}/t^{1/z}$ is kept fixed. Surface width and height-height correlation functions of arbitrary order are moments of P_f and $P_{\Delta f}$, respectively. Consequently, our analysis of the PDFs considers all the information which is contained in $W(t)$ and $\Gamma(q, \vec{l}, t)$ for arbitrary q .

To obtain values of the dynamic exponents α and β , we apply standard methods which have been reported in the literature. We measure β from the increase of the surface width with time, which follows a power law for $t \geq 150 \text{ s}$ in models A and B and for $150 \text{ s} < t < 7500 \text{ s}$ in model C which then starts to approach the final *saturation regime*. The dynamic exponents α and z have been obtained from the data collapse of the scaled height-height correlation function $G(\vec{l}, t)$. The results are summarized in table 5.1.

In figure 5.3b, we show the data collapse of P_f in models A and C which is of high quality. Model B yields similar results. Examples of rescaled $P_{\Delta f}$ are shown in figure 5.4. The data collapse is good for $\Delta f \neq 0$. However, the probability that the height difference between points at a distance $l/t^{1/z}$ is zero does not follow the behaviour which is expected from the

assumption of dynamic scale invariance. This deviation is a finite size effect. Dynamic scale invariance is a continuous symmetry property. On the other hand, due to the discrete lattice structure, differences between surface heights can assume only integer values. This makes it impossible to fulfil dynamic scale invariance exactly, since the transformation 1.9 maps integer height differences to noninteger height differences. If we approximate a real random number r with an integer i , on average the relative error $|i - r|/r$ is greater for smaller r . Therefore, it is plausible that the deviations of the empirical $P_{\Delta f}(\Delta f, \vec{l}, t)$ from the theoretical result in equation 5.7 are greater for small Δf . However, in the limit of late time and lengthscales which are large compared to the lattice constant, corrections due to the lattice structure can be neglected. Consequently, there is no indication that there is a violation of dynamic scale invariance apart from small finite size corrections. This parallels the result of Krug [57] that there is an unique exponent β in the one-dimensional Das Sarma-Tamborenea model.

Finally, we relate the static scaling properties of the surface which have been determined precisely by means of the WTMM method with the dynamic scaling properties. Our results (table 5.1) show, that the dynamic scaling exponent α and the value χ_m of the Hölder exponent which *maximizes* $D(\chi)$ agree within errorbars. This empirical finding can be explained with a saddle point argument. We calculate the standard deviation of the surface in a square of size $L \times L$,

$$w(L, t)^2 = \frac{1}{L^2} \int_0^L \int_0^L d^2x f(\vec{x}, t)^2 = \frac{1}{L^2} \int d\tilde{\chi} \underbrace{\int_0^L \int_0^L d^2x \delta(\tilde{\chi} - \chi(\vec{x})) f(\vec{x}, t)^2}_{I(\tilde{\chi})}. \quad (5.8)$$

Since $I(\tilde{\chi})$ grows like $L^{D(\tilde{\chi})}$ with L , for large L the integral over $\tilde{\chi}$ will be dominated by $I(\chi_m)$. Thus, $w(L, t)$ is governed by the subset of points which has the greatest fractal dimension. Consequently, in a multifractal surface $w(L, t)$ is identical to that of a self-affine surface with Hurst exponent χ_m . In particular, for $L < \xi(t)$ we have $w(L, t) \sim L^{\chi_m}$ (equation 1.7). On the other hand, dynamic scale invariance implies $w(L, t) \sim L^\alpha$ for $L < \xi(t)$. Consequently, $\chi_m = \alpha$.

The conventional picture of anomalous scaling [60, 62, 63] notes the difference between a “global α ” (the dynamic exponent) and a “local α ” which is determined from the power-law behaviour of $G(\vec{l}, t)$ for small l and, in our notation, is termed γ_2 . Within the multifractal formalism, the local α simply corresponds to some Hölder exponent on the ascending part of the singularity spectrum. In contrast to the dynamic scaling exponents, it is not related to any symmetry property of the model itself. Therefore, we expect the dynamic exponents α and z to be most significant to characterize the scaling properties of a growth model.

5.4 Conclusions

Our results support the following picture of the scaling behaviour of kinetically roughening surfaces: Dynamic scale invariance is fulfilled on time- and lengthscales where lattice effects can be neglected. Surfaces at fixed time have multifractal properties which are characterized by a wide spectrum of Hölder exponents. The Hölder exponent which maximizes $D(\chi)$ is identical to the dynamic exponent α . There is no indication that the singularity spectra narrow with time. Consequently, it is plausible that the multifractal properties of the surface are preserved in the limit of infinite time and there is no transition to Family-Vicsek scaling.

Model	p_d	β	χ_m	α	z	D_f
A	0	0.19 ± 0.01	0.54 ± 0.01	0.55	2.9	2.32 ± 0.01
B	0.18 %	0.17 ± 0.01	0.52 ± 0.01	0.51	3.3	2.35 ± 0.01
C	2.57 %	0.11 ± 0.01	0.38 ± 0.01	0.39	3.5	2.45 ± 0.02

Table 5.1: Simulation results: p_d is the fraction of particles which desorbs, χ_m the Hölder exponent which maximizes $D(\chi)$, α , β and z are the dynamic scaling exponents, and D_f is the fractal dimension of the surface.

Our discussion of equation 5.8 indicates that this is the most general scaling behaviour given the following conditions are fulfilled: (1) The statistical properties of the model are invariant under the dynamic scale transformation 1.9. (2) The surface is *scale-free* such that the statistical properties of sections of the surface of size L are independent of L whenever $L < \xi(t)$. Then, $\xi(t)$ is the only relevant lengthscale of the surface. This picture contains Family-Vicsek scaling as the special case where there is only one Hölder exponent.

According to López [61], there are continuum models of epitaxial growth which exhibit anomalous scaling but not multiscaling. In particular, this is the case for the Mullins equation and the Lai-Das Sarma equation. Since the singularity spectrum is the Legendre transform of γ_q , in this case $D(\chi)$ has a single peak at one characteristic Hölder exponent which equals the exponent γ_2 . Thus, the static scaling properties which are measured on short lengthscales (equation 5.5) are not related to the dynamic scaling properties. This implies necessarily, that the dynamic properties are determined by large structures which appear smooth on small lengthscales. Consequently, the surface is not *scale-free*. Instead, we expect that there is a second lengthscale $\Xi(t) < \xi(t)$. On lengthscales $\ll \Xi(t)$, the surface appears self-affine with a Hurst exponent $H = \gamma_2$. The dynamic properties are determined by structures on lengthscales between $\Xi(t)$ and $\xi(t)$. Note, that dynamic scale invariance of the model implies $\Xi(t) \propto \xi(t)$.

Table 5.1 summarizes our quantitative results. Model A without desorption reviews the results in [23], which have been obtained with slightly different activation energies on smaller systems and shorter timescales. Models B and C show, that desorption is an important process, which, although it affects only a small fraction of the adsorbed particles, must not be neglected, since it alters the scaling properties of the surfaces by reducing both α and β . Since the dynamic exponents depend continuously on the desorption rate, the paradigm of a few universality classes characterized by a *small* number of exponents which are *independent* of details of the model is *not* adequate to catch the features of kinetic roughening in our computer simulations. Since the time range of computer simulations is limited by the available CPU time, our results cannot finally disprove that there is a crossover to a different, possibly universal scaling behaviour after the deposition of a number of monolayers which is large compared to our $2 \cdot 10^4$. However, if this should indeed be the case, it is improbable that the asymptotic scaling behaviour might ever be observed on experimentally relevant timescales of a few hours of growth.

Chapter 6

The influence of the crystal lattice on coarsening in unstable epitaxial growth

In spite of considerable efforts [48, 69, 95, 110, 111, 117, 118], see e.g. [86] for an overview, a thorough theoretical understanding of the coarsening process of mounded surfaces is still lacking. In this chapter we investigate the problem of growth in the presence of a strong Schwoebel barrier which hinders interlayer transport. As discussed in section 1.5.2, this leads to an instability of the flat surface. During an initial transient, *mounds* form on the surface which start to merge as soon as their flanks have assumed the stable slope. It is generally accepted that this asymptotic coarsening regime fulfils the dynamic scale symmetry which has been introduced in section 1.5.3.

It was first pointed out by Siegert et. al. [110, 111] that lattice symmetries may play an important role in the coarsening process. These authors investigated continuum equations, using an analogy between coarsening and a phase ordering process which has recently gained popularity [58]: areas of constant slope should correspond to domains of a constant order parameter. They derived scaling exponents $\alpha = 1, \beta = 1/3$ on surfaces with a triangular symmetry, and $\beta = 1/(3\sqrt{2}) \approx 0.24$ for generic cubic surfaces, while $\beta = 1/3$ requires a fine-tuning of parameters. Moldovan and Golubovic [69] applied similar methods to surfaces with hexagonal symmetry and found $\beta = 1/3$.

However, Monte Carlo simulations have raised doubts on these predictions, since they yield $\beta \simeq 1/3$ on cubic surfaces for a great range of parameters, see e.g. [6, 15, 101, 104]. In this chapter, we address the following questions: (1) What are the *mesoscopic* processes which make the mounds coarse? (2) How does the coarsening process depend on the crystal lattice and its symmetries? (3) Do these results support a deeper analogy between coarsening and phase ordering?

6.1 Effective single particle simulations

To answer these questions, we perform computer simulations of growth on (001) surfaces of the simple cubic (sc) lattice, the simple hexagonal lattice (sh), the body-centred cubic (bcc) lattice and the (0001) surface of the hexagonal close packing (hcp). This is done under solid-on-solid conditions, i.e. the effects of overhangs or dislocations are neglected. Then, the simple lattices

can be represented by a square (sc) and a triangular mesh (sh) of integers respectively, which denote the height $h(\vec{x})$ of the surface. We build the bcc (hcp) lattice out of two intersecting sc (sh) sublattices, which contain the even and the odd heights, respectively¹. Here, an adatom in a *stable* configuration is bound to 4 (3) neighbours below in the other sublattice, which will be denoted as *vertical neighbours* in the following. Particles with fewer vertical neighbours form overhangs which are forbidden by the solid-on-solid condition. This is physically reasonable, since such particles are only weakly bound and therefore these configurations will be unstable. Additionally, particles may have neighbours in the *lateral* direction which are in the same sublattice.

The investigation of the coarsening process requires a fast algorithm which allows for the simulation of the deposition of thick films on comparatively large systems. Kinetical Monte Carlo techniques which consider the moves of many particles on the surface simultaneously are too slow for our purpose even if the efficient continuous time algorithms introduced in appendix B are used. Instead, we simulate the moves of a *single* particle from deposition until an immobile state is reached [15, 50, 101].

An adatom impinges on a randomly chosen lattice site. As discussed in section 1.4.1, it is reasonable to assume that a newly deposited adatom undergoes an incorporation process. In our model, the particle funnels downhill [32, 33, 130] to the lowest (vertical) neighbour site. On bcc and hcp this is repeated until it reaches a *stable site* as defined above. On the simple lattices this is a site \vec{x} where all nearest neighbour sites have a height $\geq h(\vec{x})$.

Then, the adatom diffuses on the surface. If the particle has no lateral neighbours, one of its neighbour sites is chosen at random. On the simple lattices, the particle moves to this site only if its height does not change, i.e. we introduce an infinite Schwoebel barrier. On the bcc or hcp lattice, the particle is moved to the neighbour site if it is stable. This condition implies an infinite Schwoebel barrier, too. Similar to our model of the zinc-blende lattice introduced in chapter 4, interlayer diffusion would require the consideration of additional hopping vectors.

As discussed in section 1.5, from time to time adatoms which diffuse around on a flat surface collide and nucleate a new island. The typical distance l_i between neighbouring islands depends on the ratio of the adatom diffusion constant D and the particle flux F . In our effective single particle dynamics, we consider this effect by limiting the maximal number of diffusion steps of a particle. If an atom has performed l_d^2 diffusion steps, diffusion stops and the particle becomes an island nucleus which will capture subsequent particles. The *diffusion length* l_d fixes the number of islands in the first layer which is identical to the initial number of mounds. In the later stages of growth, the typical terrace width is much smaller than l_d and nucleation occurs only at the top terraces of the mounds.

As soon as a particle has a lateral neighbour, it is bound to it. This process is irreversible in the sense that we forbid diffusion processes which reduce the number of bonds like the detachment from a step edge. In section 1.5 we have shown that this is a reasonable approximation if the rates of these processes are much smaller than F . However, the adatom may diffuse along the edge. After l_k^2 steps, or if the particle has reached a kink site, it is fixed to the surface. If not stated otherwise, diffusion around corners is allowed. Analogous to planar diffusion, l_k determines the typical distance of nucleation events in the effectively one-dimensional step edge diffusion, see [124] for a discussion.

In this model, we measure time t in units of the time needed to deposit one monolayer

¹For simplicity, we assume the spacing between the layers to be one unit length. Our algorithm depends only on the *topology* of the lattice.

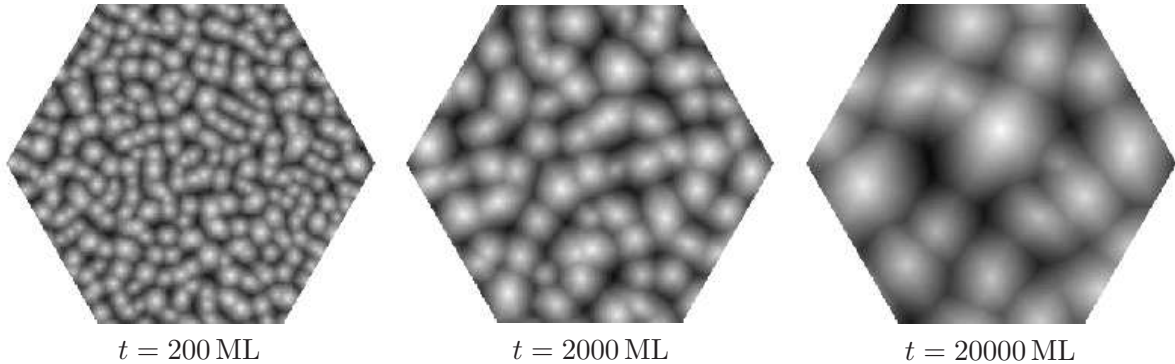


Figure 6.1: Coarsening of mounds on the hcp(0001) surface at $M = 300$, $l_d = 15$ and $l_k = 20$. Brighter shades of grey correspond to greater values of the surface height.

(ML). This algorithm may be programmed very efficiently and is at least one order of magnitude faster than full diffusion Monte Carlo algorithms.

The two essential simplifications in our model are (a) the effective representation of nucleation events in a single particle dynamics and (b) the consideration of irreversible processes, i.e. infinite energy barriers for detachment and downward diffusion at edges. For the simple cubic lattice, the model was studied in [15, 101, 104] with particular emphasis on the role of step edge diffusion. In [104] a full diffusion model is considered for comparison which includes detachment as well as finite Schwoebel barriers and displays the same asymptotic coarsening exponents as measured in the simplified model.

In all our simulations we choose $l_d = 15$ which controls the initial island distance. We simulate a variety of different values of the step edge diffusion length l_k in the range between $l_k = 1$ and $l_k = 20$. The simulations are performed on a square of $N \times N$ lattice constants using periodic boundary conditions (bcc and sc) and a regular hexagon with edges of length M (hcp and sh) using helical boundary conditions, our standard values being $N = 512$ and $M = 300$. For every parameter set we have performed 7 independent simulation runs.

6.2 Surface morphologies

During the first (about 100) monolayers of growth on an initially flat surface islands nucleate on which mounds build up and take on their stable slope. Then, the asymptotical coarsening regime starts. As an example, in figure 6.1 we show the evolution of the hcp surface at $l_k = 20$. As expected, on the simple lattices the mounds obtain regular shapes which are determined by the symmetry of the surface: square pyramids on sc, hexagonal ones on sh (figure 6.2). On bcc and hcp however, *rounded* corners as well as sharp corners can be found (figures 6.1, 6.4 and 6.5).

Here one finds two fundamentally different types of mounds: On the one hand there are mounds, where *all* corners are rounded with octagonal shapes on bcc (figure 6.5b), and 12-cornered ones on hcp. On the other hand, one observes a *breaking* of the *symmetry* given by the lattice: approximately triangular mounds on hcp (figure 6.4b) and oval shapes on bcc (figure 6.5a), where every second corner is sharp while the others are rounded. We have observed that in the process of coarsening, on all lattice structures mounds merge preferentially at the *corners*, while mounds touching at the flanks are a *metastable* configuration. On bcc

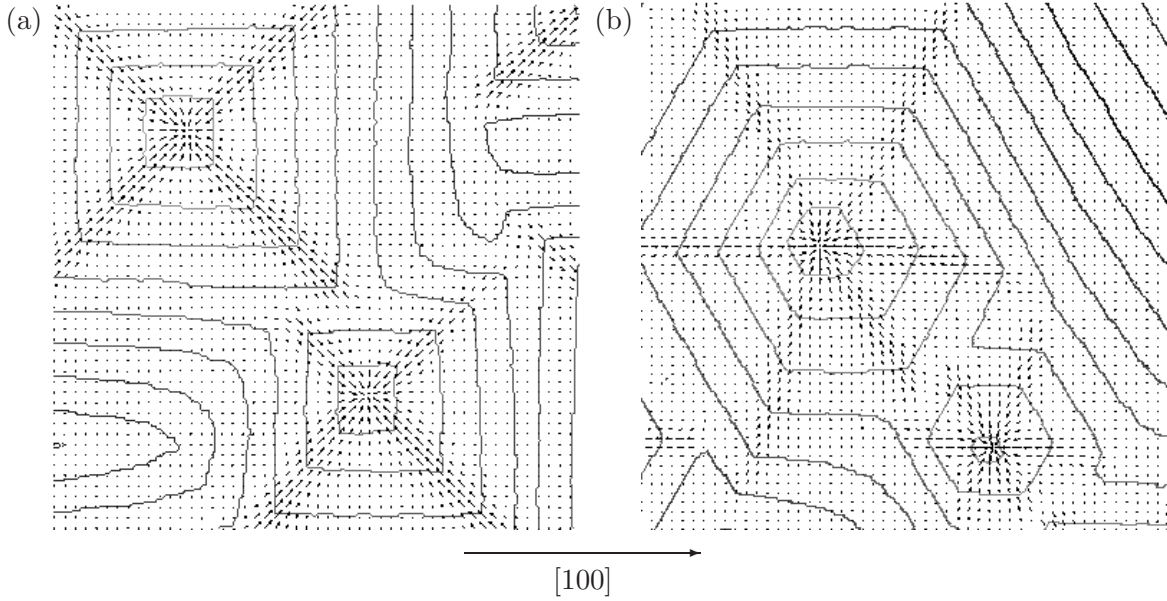


Figure 6.2: Contour plots of surfaces of the simple lattices at $t = 2 \cdot 10^4$ ML. Brighter contours denote greater surface heights. The arrows show the average diffusion current on the surface during the deposition of additional 200 ML. The figures show sections of 250×250 lattice constants of systems of size $N = 512$ (simple cubic, panel (a)) and $M = 300$ (simple hexagonal, panel (b)). Diffusion length and step edge diffusion length are $l_d = 15$ and $l_k = 20$, respectively.

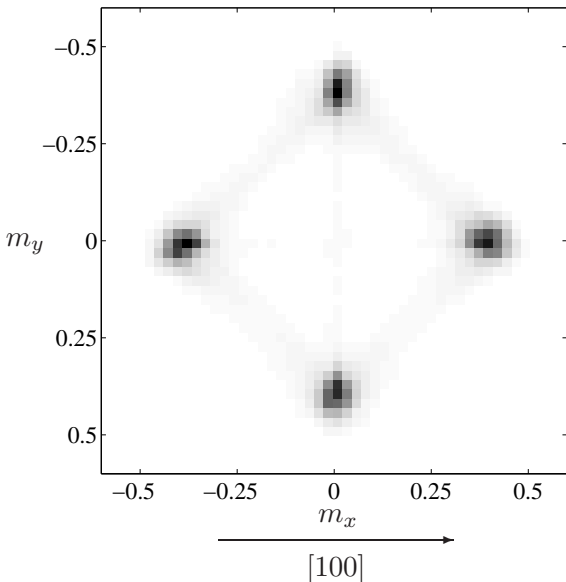


Figure 6.3: Histogram of the slopes on simple cubic surfaces ($N = 512$, $l_d = 15$, $l_k = 20$, $t = 2 \cdot 10^4$ ML). High probabilities are drawn dark. Each of the four dark spots corresponds to the slope of one pyramid edge.

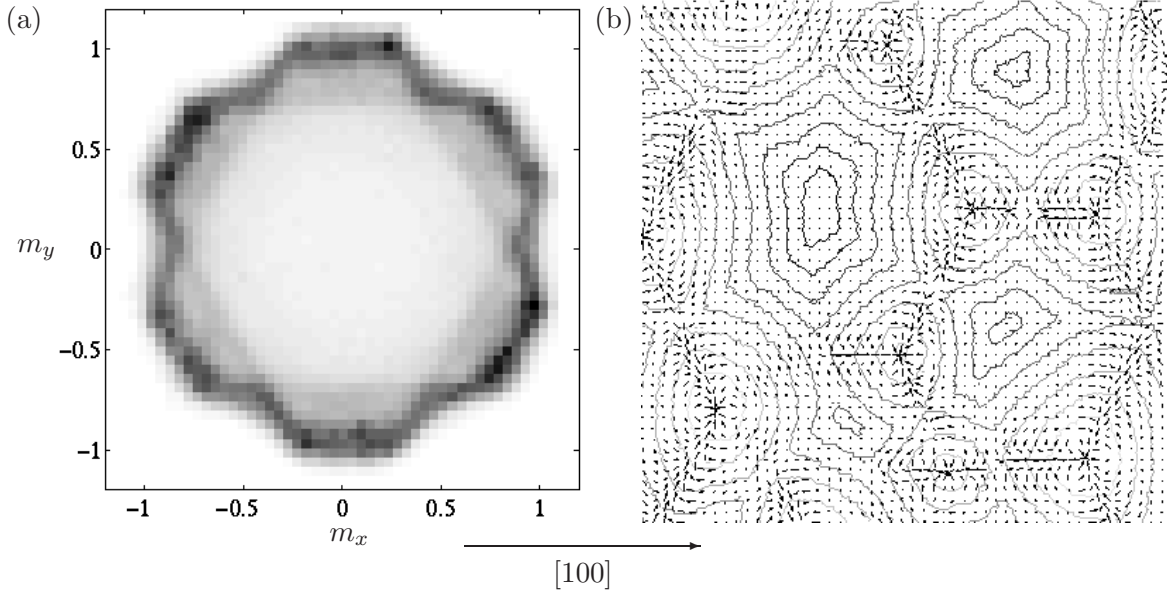


Figure 6.4: Simulation results on hcp ($M = 300$, $l_d = 15$, $l_k = 10$, $t = 20000$ ML). Panel (a): Histogram of slopes (density plot). High probabilities are drawn dark. Panel (b): Contour plot of a part of size 250×250 lattice constants of the surface. High levels are plotted in light grey. The arrows show the diffusion current as measured during the deposition of additional 200 ML.

and hcp, the metastable configuration consists of mounds with completely rounded corners. Mounds whose shapes break the lattice symmetry are always in the course of merging with a neighbour they touch with a sharp corner. Note that similar configurations were observed in a full diffusion simulation of bcc(001) growth [6].

To characterize the morphology quantitatively, we investigate the slopes $\vec{m} = \nabla h$ of the surface. On average, $|\vec{m}|$ obtains a value which can be estimated by a simple argument [84]: The Schwoebel effect yields an uphill current due to the preferential attachment of particles to steps from the lower terrace which is compensated by a downhill current due to funneling. If we assume that a particle reaches its final height after at most one incorporation step, the sc and the sh surface select $|\vec{m}| = 1/2$, while bcc and hcp select $|\vec{m}| = 1$. In practice, the selected slopes are slightly smaller, since the maximal number of incorporation steps in the funneling process is unlimited. Since a direct computation of the numerical gradient of simulated surfaces fails due to the discrete heights, we first apply a gaussian filter with variance $\sigma = 4$. This value has turned out to be a good compromise: it removes the atomistic structure but preserves the shape of the mounds. On sc and sh, we find a regular square and hexagon of slightly broadened peaks, respectively, which correspond to the slope of the flanks of the mounds (figure 6.3). This is what one expects at pyramidal mounds.

On bcc and hcp, however, we obtain a more complicated pattern. Figure 6.4a shows a histogram of the slopes on hcp surfaces: due to the round shapes of the mounds, one finds a pronounced maximum of the probability density function in every direction of \vec{m} . The most probable value of $|\vec{m}|$ has a directional dependence: it is *minimal* in the lattice directions (0.88 ± 0.02), and *maximal* (0.99 ± 0.02) in the intermediary directions. Consequently, the

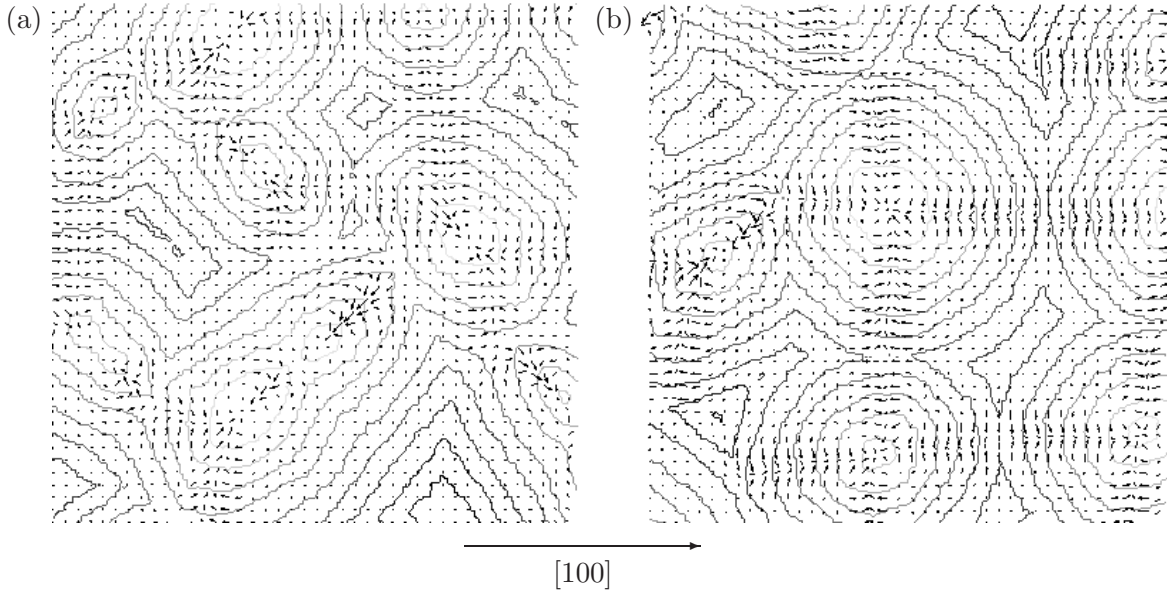


Figure 6.5: Contour plots of parts of size 250×250 lattice constants of bcc surfaces ($N = 512$, $l_d = 15$, $l_k = 10$, $t = 2 \cdot 10^4$ ML). Panel (a): section dominated by quickly coarsening mounds breaking the surface symmetry. Panel (b): metastable configuration.

rounded corners are *steeper* than the flanks. This is possible because the rounding occurs at the base of the mounds, whereas close to the tips corners are typically sharp, cf. figure 6.5. On bcc the results are equivalent, apart from the different symmetry.

6.3 Diffusion currents

In order to gain deeper insight into the coarsening process, we investigate the *material transport* on mesoscopic lengthscales by tracing the motion of particles on the surface. On all lattice structures, we observe a strong uphill current at the corners of mounds which is a geometrical effect: an adatom attaching at the corner is transported over a mean distance l_k , namely with equal probability along either of the two flanks of the mound. This results in a net current \vec{j} in the direction of the bisector of the angle at the corner, which is directed uphill. A simple calculation yields

$$|\vec{j}| = r_a l_k \cos \frac{\phi}{2}$$

if there is a straight step edge of length $\gg l_k$, which is the case on the simple lattices (figure 6.2). Here, r_a is the rate at which particles attach to a step edge. ϕ is the angle between the two steps which meet at a corner. We have $\phi = \pi/2$ on surfaces with cubic symmetry and $\phi = 2\pi/3$ on hexagonal surfaces.

On the bcc and the hcp lattice however, material transport along step edges is severely restricted due to the rounded corners. There, particles diffusing along the edge are typically *reflected*. This can be understood from the fact that the slope of the rounded corners is high. Consequently, there are sites next to a step where an additional atom would have less than 4 (on bcc) or 3 (on hcp) vertical neighbours. Since we consider only diffusion to stable sites,

an atom cannot cross such sites.

In the metastable configuration, this leads to a current towards the middle of the smooth step edges at the flanks of the mounds which have an extension $\approx l_k$ (figure 6.5). This current has a non-vanishing *uphill* component due to the Schwoebel effect. On the rounded corners on the contrary, one observes a weak *downhill* current. This is explained by the observation of steep gradients (figure 6.4a), at which the downhill current due to funneling dominates the uphill current of the Schwoebel effect. On these surfaces the stable slope at which the currents cancel is *not* assumed *locally*, but only in the *global* average, which results in spatial current patterns on the surface. An analogous behaviour is observed at the symmetry-breaking, merging mounds (figures 6.4b, 6.5a). Here, the smooth edges are in the proximity of the sharp corners. Particles are reflected at the rounded corners, too. This yields a net current towards the sharp corners which *compensates* the geometrically induced uphill current exactly if the smooth edges have a length l_k . This fact explains the broken symmetry of these mounds: if there is any process which transports matter towards sharp corners, this material is not completely diffusing inward as it would be the case on pyramidal mounds but is attached to the corner and makes it overgrow its neighbours. Merging of mounds, however, *is* such a process: consider a terrace which goes around two mounds touching each other at the corners. Due to its curvature, in this contact zone there is a high concentration of kink sites which make it a *sink* for diffusing particles.

6.4 Theoretical estimation of scaling exponents

Our observation that mounds merge preferentially in positions with touching corners gives strong evidence that the current which fills the gap between two mounds plays a dominant role in the process of coarsening, at least in the case of large l_k where it is efficient. If this is the case, then a simple consideration yields the scaling exponents: Due to step edge diffusion, adatoms are transported over a typical distance l_k . If l_k is noticeably greater than a few lattice constants, this is much more than the average terrace width. Then, material transport via diffusion on terraces is small compared to transport via step edge diffusion and can be neglected. Our investigation of the diffusion currents shows, that the current into the gap is significant on a few atomic layers in the vicinity of the contact point only. In consequence, this current is *independent* of the size of the mounds if the latter is much greater than l_k . Since the volume of the gap is proportional to L^3 , if L is the typical distance between the mounds, it will take a time $t \sim L^3$ to fill it. In consequence, $L \sim t^{1/3} \implies z = 3$. Since $\alpha = 1$ in the presence of slope selection, this yields $\beta = 1/3$. In contrast to the effects discussed in [110, 111] these considerations are completely independent of lattice symmetries. In [117, 118] a similar argument has been applied to the case of coarsening in the absence of dominant step edge diffusion processes (“bond energy driven coarsening”), where material is transported mainly by terrace diffusion. This yields $\beta = 1/4$. The same exponent is obtained, if coarsening is exclusively due to fluctuations in the particle beam (“noise assisted coarsening”). We expect, that these processes dominate step edge diffusion in the limit of small l_k which leads to a transient from $\beta = 1/4$ to $\beta = 1/3$ if l_k is increased.

6.5 Measurement of scaling exponents

We apply a variety of methods to measure the scaling exponents. This is important as a consistency check and to eliminate systematical errors which might be intrinsic to some methods. According to equation 1.11, β can be obtained from the increase of the *surface width* $W(t) \sim t^\beta$ [12]. This power law behaviour may be corrupted by the presence of noise on the surface profile, an additional contribution to $W(t)$ which has been called *intrinsic width* [12, 49]. Similarly, the *number of mounds* n_m in the system will decrease like $t^{-2/z}$, if this scaling hypothesis holds. We measure n_m by counting the number of *top terraces* in the system. Since a single particle is counted as a top terrace, this method may be misleading if particles nucleate on terraces at the flanks of mounds. A method which is widely used in the literature uses the fourier transform $\hat{f}(\vec{k})$ of the reduced surface height $f(\vec{x})$: The *structure factor* $S(\vec{k}) := \langle \hat{f}(\vec{k})\hat{f}(-\vec{k}) \rangle$ is maximal at nonzero wavenumbers $|\vec{k}_m| = 2\pi/l_m$, if there are structures at a typical lengthscale l_m on the surface. Since $l_m \sim t^{1/z}$, $|\vec{k}_m|$ will decay $\sim t^{-1/z}$. In practice, a direct search for the maximum often fails due to noise effects; one avoids this problem by calculating the averages $k_m^{(p)} := \left(\sum_{\vec{k}} |\vec{k}| S(\vec{k})^p \right) / \sum_{\vec{k}} S(\vec{k})^p$. However, the choice of the correct power p is a bit arbitrary.

6.5.1 The wavelet method

To avoid these difficulties, we propose a method which uses the continuous wavelet transform which was introduced in chapter 5. Due to the easier numerical computation, we employ the two-component version 5.4.

The basic idea of this transformation is to convolve $h(\vec{x})$ with the wavelet which is *dilated* with the scale a . As already noted in section 5.2, in a wavelet transform where the radially symmetrical filter $\Phi(\vec{x})$ is a gaussian, the search for the wavelet transform modulus maxima (WTMM) at scale a is equivalent to the detection of edges of structures of size $\sim a$ [65, 66]. This makes it a natural tool to search for the typical size a_t of mounds on the surface. Therefore, in the remainder of this chapter we use this particular wavelet. We investigate the average of the WTMM on the scale a

$$\Omega(a) := \left\langle M_{\vec{\Psi}}[h](\vec{b}, a) \right\rangle_{\vec{b}=\text{WTMM}}. \quad (6.1)$$

This function has a pronounced maximum at a value a_m which is the scale that contains the most relevant contributions to the surface morphology. On mounded surfaces, we expect $a_m \propto a_t$. As an example, $\Omega(a)$ of the surface of a simple cubic crystal is shown in figure 6.7. Figure 6.6 shows the WTMM of the same surface at different scales including $a = a_m = 17$. Clearly, at $a = a_m$ the WTMM lines trace the contours of the mounds. On the contrary, at the small scale $a = 5$, the search for the WTMM yields structures at the flanks of the mounds which are small compared to the mounds themselves. The positions of the WTMM lines at $a = 80$ which is much greater than a_m are not related to the mounds at all. On other lattice structures and at different time, we obtain similar results. Consequently, a_m is indeed a measure for the *lateral* size of the mounds. Since the convolution of the surface with the wavelet $\vec{\Psi}_0$ is the gradient of the surface smoothed with the gaussian filter Φ_0 , $\Omega(a_m)$ is a measure for the *height* of the mounds. During the coarsening process, we have $a_m \sim t^{1/z}$ and $\Omega(a_m) \sim t^\beta$.

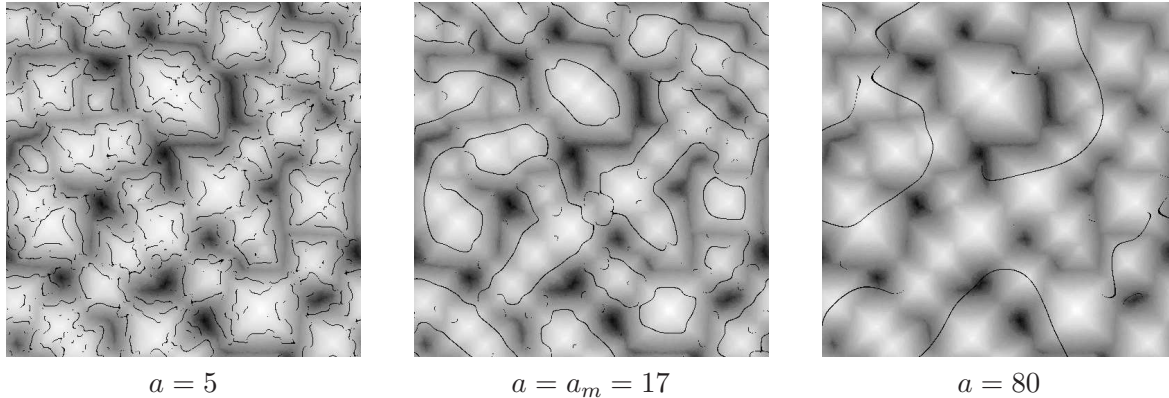


Figure 6.6: WTMM at the surface of a simple cubic crystal ($N = 512$, $l_d = 15$, $l_k = 8$, $t = 3400$ ML) at different scales a . The WTMM are shown in black. At $a = a_m$, the WTMM lines trace the contours of the mounds. At smaller a , the WTMM lines enclose details of the surface at the flanks of the mounds, whereas at large a the WTMM seem to be independent of the mounds.

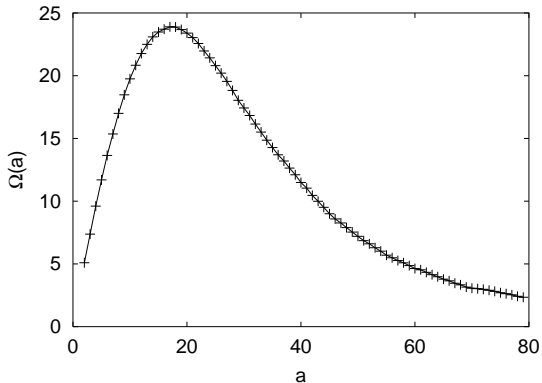


Figure 6.7: $\Omega(a)$ for the surface shown in figure 6.6. There is a pronounced maximum at $a = a_m = 17$ where the WTMM lines enclose the mounds.

This procedure has several advantages compared to the standard methods used in the literature: (1) The detection of the WTMM leads to an efficient suppression of noise and therefore eliminates the (noisy) intrinsic width. (2) Since only the most important lengthscale is considered, the results may not be corrupted by details of the surface morphology on small lengthscales. (3) Appropriate wavelets are well localized both in real space and in Fourier space. Therefore, this analysis combines the advantages of real space techniques, like the counting of mounds, and Fourier techniques, like the calculation of k_m^p . We have tested this method on various artificial test surfaces and found a clear superiority to the standard methods, especially in the presence of noise which should make it interesting for experimental investigations.

6.5.2 Results

In our simulations, the asymptotic scaling behaviour is obtained after a long initial transient of about 100 monolayers. Since after this transient only a comparatively small number of mounds is left on the surface, the measurement of exponents is complicated by finite size effects: due to the periodicity of the system, there is a *self-interaction* of the currents on the

mounds, if their size is no more small compared to the system size. We measure $\alpha \approx 1$ for all $l_k > 1$, a consequence of slope selection. At $l_k = 1$ however, we measure smaller values which *do* depend on the crystal lattice: $\alpha = 0.85$ on bcc and $\alpha = 0.94$ on hcp. A similar effect was observed in [15, 101] on the simple cubic lattice. We remark that our results are independent of the method which was applied to measure the exponents.

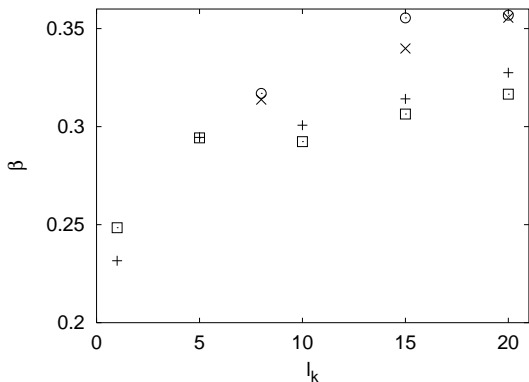


Figure 6.8: β , as obtained from the wavelet method, plotted as a function of the step edge diffusion length. +: bcc lattice, \times : sc, \square : hcp, \odot : sh. Results from measurements of β from the surface width are identical within error bars which are on the order of magnitude of the symbol size. These have been estimated from the logarithmic fits; we expect the true errors to be larger due to systematical deviations.

In figure 6.8, β is plotted as a function of l_k . Clearly, its value does *not* depend systematically on the *symmetry* of the crystal surface. We find no significant deviations between β on bcc and on hcp (sc and sh). As already observed in [15, 101], there is a dependence of β on the step edge diffusion length. One obtains values $\approx 1/4$ at $l_k = 1$ and higher values at greater l_k . The values obtained at large l_k are compatible with $\beta = 1/3$. As indicated above, we explain this transient as a competition between different coarsening mechanisms. At large l_k the merging of mounds should proceed mainly by the step edge diffusion driven transport of material into the gap, at small l_k it is dominated by noise assisted coarsening and/or bond energy driven coarsening. This competition might also explain why the exponents measured on bcc and hcp are still slightly smaller than those obtained on the simple lattices even at values of l_k as large as 20, since the symmetry breaking of the mounds on these lattices halves the number of corners which are active in the coarsening process.

All the simulation results reported above have been obtained in simulations with unhindered step edge diffusion. To further corroborate our ideas of the coarsening process, we have also performed simulations with a corner diffusion barrier. A particle may perform at most l_k^2 diffusion hops along a straight step edge, but diffusion around corners is forbidden. Then, we observe *no symmetry breaking* of the mounds, which now obtain regular polygonal shapes on all lattice structures. These are rotated by an angle of 45 degrees against the lattice directions on cubic surfaces and 30 degrees on hexagonal ones. Due to the absence of aligned step edges, material transport by step edge diffusion is severely restricted under these conditions. Thus, we measure only small diffusion currents and observe no pronounced long-range order in the flux lines. Here, we find $\alpha \approx 1$, $\beta \approx 1/4$ on *all* lattices, *independent* of the step edge diffusion length. This slow coarsening in absence of the characteristic features of step edge diffusion driven coarsening—currents on mesoscopic lengthscales and symmetry breaking on bcc and hcp—strongly supports the important role of this mechanism for fast coarsening with $\beta = 1/3$.

6.6 Conclusions

In summary, we have presented a detailed investigation of the coarsening process in epitaxial growth. Our most important finding is that the crystal lattice has a considerable influence on the morphology of the growing surface which is by no means restricted to trivial symmetry effects. In spite of these differences, in the limit of large step edge diffusion lengths the mounds coarsen according to power laws with universal exponents. We obtain $\beta \approx 1/3$ in the case of unhindered step edge diffusion. In the case of restricted step edge diffusion, $\beta \approx 1/4$ is observed as it is for unhindered step edge diffusion with a small value of l_k .

Amar [6] has obtained values of the coarsening exponents of bcc(001) surfaces which agree with our results within errorbars. He performed standard kinetical Monte Carlo simulations which consider the motion of many particles on the surface simultaneously. However, with this method only the simulation of the deposition of at most 300 ML was possible, and the initial formation of mounds took up to 100 monolayers. Our effective single particle dynamics, on the contrary, allows for the simulation of $2 \cdot 10^4$ ML such that coarsening can be investigated over two decades in time. Thus, our simulations give strong evidence that the measured values of α and β are indeed the dynamic exponents of the asymptotic regime. Conversely, the agreement of the results proves that the simplifications made in the effective single particle dynamics do not alter the values of the coarsening exponents.

Our results contradict previous studies of the coarsening process using continuum equations [69, 95, 110, 111] which predict slower coarsening on surfaces with a cubic symmetry. In these publications, equations have been studied which are invariant under the transformation $h(\vec{x}) \rightarrow -h(\vec{x})$. This symmetry reflects itself also in the up-down-symmetry of the solutions of the equations. Clearly, our simulation results *break* this symmetry and the arguments of [95, 110, 111] cannot apply here. In figures 6.2, 6.4b and 6.5 the contours of the mounds and those of the valleys are clearly distinct. This is also true for the *currents*, especially the step edge diffusion current which dominates the coarsening behaviour in the limit of large l_k and unhindered step edge diffusion and determines the scaling exponents. We conclude, that the breaking of the up-down symmetry is a central feature of unstable epitaxial growth. Its precise effect on the coarsening dynamics clearly deserves further attention.

However, we find it difficult to interpret our result in the context of an analogy to phase ordering processes, where the local slope of the surface corresponds to an order parameter. In this picture, the importance of the breaking of up-down symmetry leads to the conclusion, that now the stability of a domain wall between areas of equal slope is a complicated function of both the *orientation* of the wall and the *order parameters* on both sides of it. Additionally, in contrast to the simple lattices where there are only 4 (sc) respectively 6 (sh) stable slopes, on bcc and hcp one would have to deal with a *continuous* order parameter.

In any case, the behaviour of our models which implement the microscopic processes on the surface is governed by much more complex rules than those implemented in all the continuum models we are aware of. Differences are by no means restricted to some details, but have a fundamental influence on the behaviour of the system on large lengthscales.

Appendix A

Transfer matrices and finite size scaling

In principle, the transfer matrix method [19, 120] is a technique to calculate the free energy of *one-dimensional* lattice systems exactly in the thermodynamic limit. However, a system of arbitrary dimension can be treated formally as a one-dimensional system if it is decomposed in slices along an arbitrary direction. Each slice is then treated as one site in an infinite chain of slices. Since the transfer matrix method can consider only a *finite*, however large, number of possible states per site, the size of the slices must be finite. Therefore, in general we can investigate only semi-infinite systems which are finite in all directions but one. Only in some special cases, like the two-dimensional Ising model in the absence of a magnetic field, the limit of a real infinite system can be performed exactly. Otherwise, in two or more dimensions we must apply finite size scaling techniques to extrapolate to the thermodynamic limit from results obtained for semi-infinite systems.

A.1 The transfer matrix method

Consider a chain of N identical slices of a system of arbitrary dimension. Let \mathcal{M} denote the number of sites per slice. Each slice j can be in one of \tilde{n} different states X_j . We assume that there are interactions only between neighbouring slices. Interactions of longer but finite range can be considered by increasing the thickness of the slices. Then, the energy of the system can be written as

$$H = \tilde{H}(X_N, X_1) + \sum_{j=1}^{N-1} \tilde{H}(X_j, X_{j+1}) \quad (\text{A.1})$$

where we have assumed periodic boundary conditions. For simplicity, we assume without loss of generality that $\tilde{H}(X, Y) = \tilde{H}(Y, X)$. It is always possible to rearrange the Hamiltonian of the system such that this property is fulfilled. The partition function is

$$Z = \sum_{\{X_j\}_{j=1}^N} \exp \left[-\beta \tilde{H}(X_N, X_1) \right] \prod_{j=1}^{N-1} \exp \left[-\beta \tilde{H}(X_j, X_{j+1}) \right]. \quad (\text{A.2})$$

To calculate it, we map each of the \tilde{n} possible configurations of a slice to one of \tilde{n} orthonormal vectors, which span up a \tilde{n} -dimensional Hilbert space:

$$X \longleftrightarrow |X\rangle \quad \text{such that} \quad \langle X|Y\rangle = \begin{cases} 1 & \text{if } X \equiv Y \\ 0 & \text{else} \end{cases} . \quad (\text{A.3})$$

In the base of these vectors we define the $\tilde{n} \times \tilde{n}$ transfer matrix

$$T = \sum_{|X\rangle, |Y\rangle} |X\rangle \exp \left[-\beta \tilde{H}(X, Y) \right] \langle Y| , \quad (\text{A.4})$$

which has the property that the trace of T^N is equal to the partition function:

$$\begin{aligned} \text{Tr} [T^N] &= \sum_{|X_1\rangle} \langle X_1| T^N |X_1\rangle \\ &= \sum_{|X_1\rangle, \dots, |X_N\rangle} \langle X_1| T |X_2\rangle \langle X_2| T |X_3\rangle \cdots \langle X_N| T |X_1\rangle \\ &= \sum_{|X_1\rangle, \dots, |X_N\rangle} \exp \left[-\beta \tilde{H}(X_N, X_1) \right] \prod_{j=1}^{N-1} \exp \left[-\beta \tilde{H}(X_j, X_{j+1}) \right] \\ &= Z \end{aligned}$$

Consequently, the partition function can be expressed in terms of the eigenvalues λ_i of T . Since $\tilde{H}(X, Y) = \tilde{H}(Y, X)$, T is symmetric and all λ_i are real. We have

$$Z = \text{Tr} [T^N] = \sum_{i=1}^{\tilde{n}} \lambda_i^N . \quad (\text{A.5})$$

This identity can be used to calculate the free energy per site f in the limit of infinite N . The theorem of Perron-Frobenius states that the eigenvalue with the greatest absolute value is positive and nondegenerate. In the following, we will assume that the eigenvalues are sorted in descending order such that $\lambda_1 > \lambda_2 \geq \dots \geq \lambda_{\tilde{n}}$. Then,

$$f = -\frac{1}{\beta N \mathcal{M}} \ln Z = -\frac{1}{\beta N \mathcal{M}} \ln \left[\lambda_1^N \left(1 + \sum_{i=2}^{\tilde{n}} \left(\frac{\lambda_i}{\lambda_1} \right)^N \right) \right] \xrightarrow{N \rightarrow \infty} -\frac{1}{\beta \mathcal{M}} \ln \lambda_1 . \quad (\text{A.6})$$

Thus, we can calculate the free energy of a semi-infinite system by calculating the greatest eigenvalue of the $\tilde{n} \times \tilde{n}$ -dimensional transfer matrix T . Usually this is done numerically since \tilde{n} increases exponentially fast with the number of sites per slice.

A.1.1 Thermal averages

The standard method in statistical physics to calculate the thermal average $\langle q \rangle$ of an arbitrary intensive quantity q uses a field h which couples to q . Then,

$$\langle q \rangle = \lim_{h \rightarrow 0} \frac{\partial f_q}{\partial h} \quad (\text{A.7})$$

where f_q is the free energy of the system with the modified Hamiltonian $H_q = H + hN\mathcal{M}q$. Of course, this method can be applied straightforwardly in the transfer matrix formalism by performing the differentiation with respect to h numerically.

There is however an alternative which can be applied whenever q is well defined as a function $q(X_k)$ of the state of a single slice k . Then, since all slices are identical, the thermal average of q is the same in all slices and identical to the thermal average of q in the whole system. In a chain of N slices with periodic boundary conditions

$$\begin{aligned}\langle q \rangle &= \frac{1}{Z} \sum_{\{X_i\}_{i=1}^N} q(X_k) \exp \left[-\beta \tilde{H}(X_N, X_1) \right] \prod_{i=1}^{N-1} \exp \left[-\beta \tilde{H}(X_i, X_{i+1}) \right] \\ &= \frac{1}{Z} \sum_{|X_1\rangle, |X_k\rangle} \langle X_1 | T^{k-1} | X_k \rangle q(X_k) \langle X_k | T^{N-k+1} | X_1 \rangle.\end{aligned}\quad (\text{A.8})$$

The transfer matrix T can be written as $T = \sum_{i=1}^{\tilde{n}} |\lambda_i\rangle \lambda_i \langle \lambda_i|$, where $|\lambda_i\rangle$ is the normalized eigenvector to the eigenvalue λ_i . Further, we introduce the matrix

$$\hat{q} = \sum_{|X\rangle} |X\rangle q(X) \langle X| \quad (\text{A.9})$$

which will be denoted as the operator of q in the following. Then,

$$\langle q \rangle = \frac{1}{Z} \sum_{i=1}^{\tilde{n}} \lambda_i^N \langle \lambda_i | \hat{q} | \lambda_i \rangle \xrightarrow{N \rightarrow \infty} \langle \lambda_1 | \hat{q} | \lambda_1 \rangle, \quad (\text{A.10})$$

where we have used that $\langle \lambda_i | \lambda_j \rangle = \delta_{i,j}$ and $\sum_{|X_1\rangle} |X_1\rangle \langle X_1| = 1$. Thus, the thermal average of q can be calculated easily from the normalized eigenvector $|\lambda_1\rangle$.

In particular, the probability $P(X)$ to find a slice in state X is the thermal average of n_X which is defined as one, if the slice is in state X and zero otherwise. Its operator is $\hat{n}_X = |X\rangle \langle X|$. Using equation A.10, we find

$$P(X) = \langle \lambda_1 | X \rangle \langle X | \lambda_1 \rangle = |\langle \lambda_1 | X \rangle|^2. \quad (\text{A.11})$$

The square of every component of the normalized eigenvector to the greatest eigenvalue of T , represented in the base of the vectors $|X\rangle$, is the probability to find a slice in a particular state.

A.1.2 The correlation length

If we measure an arbitrary quantity q simultaneously in two different slices, due to the interactions between the slices these values are not statistically independent. This fact is measured by the correlation function

$$g_q(|l - k|) := \langle q(X_k) q(X_l) \rangle - \langle q \rangle^2. \quad (\text{A.12})$$

Nonzero values indicate correlations between $q(X_k)$ and $q(X_l)$. The thermal average of $q(X_k) q(X_l)$ in a chain of N slices can be expressed in terms of the transfer matrix:

$$\begin{aligned}\langle q(X_k) q(X_l) \rangle &= \frac{1}{Z} \sum_{\{X_i\}_{i=1}^N} q(X_k) q(X_l) \exp \left[-\beta \tilde{H}(X_N, X_1) \right] \prod_{i=1}^{N-1} \exp \left[-\beta \tilde{H}(X_i, X_{i+1}) \right] \\ &= \frac{1}{Z} \sum_{|X_1\rangle} \langle X_1 | T^{k-1} \hat{q} T^{l-k} \hat{q} T^{N-l+1} | X_1 \rangle.\end{aligned}\quad (\text{A.13})$$

For simplicity, we have assumed that $l > k$. We continue by expressing the transfer matrix in terms of its eigenvectors and eigenvalues and performing the limit $N \rightarrow \infty$. We find

$$\begin{aligned} \langle q(X_k)q(X_l) \rangle &= \frac{1}{Z} \sum_{i,j=1}^{\tilde{n}} \lambda_i^{k-1} \langle \lambda_i | \hat{q} | \lambda_j \rangle \lambda_j^{l-k} \langle \lambda_j | \hat{q} | \lambda_i \rangle \lambda_i^{N-l+1} \\ &\xrightarrow{N \rightarrow \infty} \langle \lambda_1 | \hat{q} | \lambda_1 \rangle^2 + \sum_{j=2}^{\tilde{n}} \left(\frac{\lambda_j}{\lambda_1} \right)^{l-k} |\langle \lambda_1 | \hat{q} | \lambda_j \rangle|^2 \end{aligned} \quad (\text{A.14})$$

The first term in equation A.14 yields $\langle q \rangle^2$. If $l - k \gg 1$, the sum is dominated by the term where the *absolute* value of λ_j is maximal and the matrix element $\langle \lambda_1 | \hat{q} | \lambda_j \rangle \neq 0$. In the following, we denote this eigenvalue as λ_m and the corresponding eigenvector as $|\lambda_m\rangle$. This yields the following asymptotics for the correlation function:

$$g_q(|l - k|) \sim |\langle \lambda_1 | \hat{q} | \lambda_m \rangle|^2 \left(\frac{\lambda_m}{\lambda_1} \right)^{|l-k|} \quad (\text{A.15})$$

If λ_m is positive, $g_q(|l - k|)$ decays exponentially. On the other hand, if λ_m is negative, $g_q(|l - k|)$ oscillates with an exponentially decaying amplitude between positive and negative values. This indicates that the values of q in neighbouring slices are anticorrelated. In both cases, the amplitude decays on a typical lengthscale

$$\xi = \left[\ln \left(\left| \frac{\lambda_1}{\lambda_m} \right| \right) \right]^{-1} \quad (\text{A.16})$$

which is called *correlation length*.

A.1.3 Symmetries of the Hamiltonian and vanishing matrix elements

The transfer matrix formalism is based on the assumption that the Hamiltonian of the investigated system is invariant under translations of the system in the infinite direction. However, frequently both the Hamiltonian and the operator of a quantity q fulfil additional symmetry properties. These can be used to predict which of the matrix elements $\langle \lambda_i | \hat{q} | \lambda_j \rangle$ are zero. Let there be an operator \hat{U} which maps each configuration of a slice uniquely to another one. We assume that the energy of the system is invariant under this transformation. Since the transfer matrix has the same symmetry properties as the Hamiltonian, we have

$$\hat{U}^\top \hat{U} = 1 \quad (\text{A.17})$$

$$\hat{U} T \hat{U}^\top = \hat{U}^\top T \hat{U} = T. \quad (\text{A.18})$$

Further, we assume that the operator \hat{q} is either symmetric or antisymmetric under the transformation \hat{U} such that

$$\hat{U} \hat{q} \hat{U}^\top = \chi_{\hat{q}} \hat{q} \quad \text{where } \chi_{\hat{q}} \in \{-1, 1\}. \quad (\text{A.19})$$

Applying equations A.17 and A.18 to the product of the transfer matrix with its eigenvector $|\lambda_i\rangle$ we find

$$\hat{U} T |\lambda_i\rangle = \hat{U} T \hat{U}^\top \hat{U} |\lambda_i\rangle = T \hat{U} |\lambda_i\rangle = \lambda_i \hat{U} |\lambda_i\rangle.$$

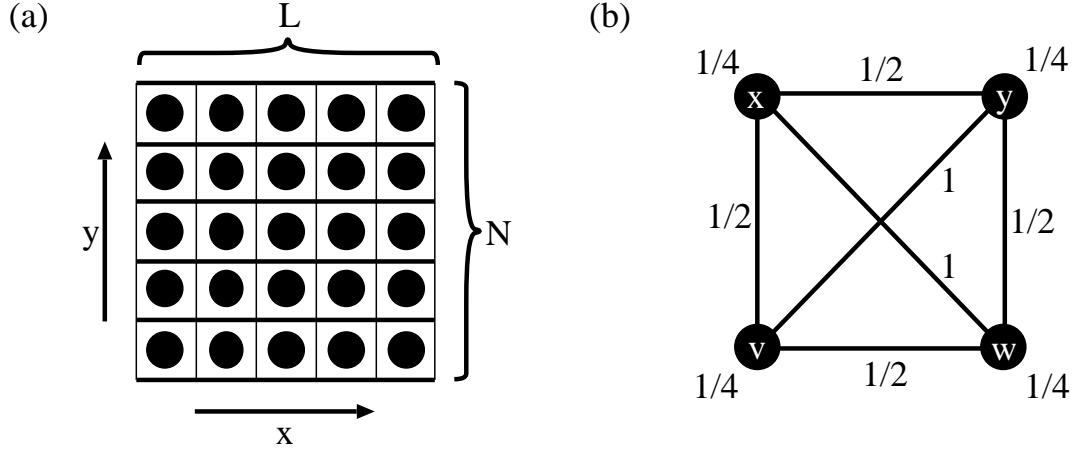


Figure A.1: Sketch of a square lattice system as discussed in section A.1.4. Panel (a) shows the decomposition of the system in lines with L sites each. Panel (b) shows the unit cell of the lattice. Sites are shown as black circles. Possible interactions are symbolized by lines. Note, that each of the sites belongs to four unit cells. The nearest neighbour bonds belong to two unit cells. Therefore, in the calculation of $h(v, w, x, y)$, the energies of these objects have to be weighted with the factors shown in the figure to avoid multiple counting of energies in equation A.24.

Consequently, $\hat{U} |\lambda_i\rangle$ is an eigenvector to the eigenvalue λ_i of the transfer matrix. In case of a non-degenerate eigenvalue λ_i , this condition implies

$$\hat{U} |\lambda_i\rangle = \chi_i |\lambda_i\rangle \quad \text{where } \chi_i \in \{-1, 1\}, \quad (\text{A.20})$$

since due to equation A.17 the multiplication with \hat{U} leaves the norm of $|\lambda_i\rangle$ invariant. If λ_i is degenerate, the eigenvectors of T are not uniquely determined. However, it is always possible to construct a set of orthonormal eigenvectors such that equation A.20 is fulfilled. Vectors with $\chi_i = 1$ are *symmetric* under the transformation \hat{U} . $\chi_i = -1$ characterizes an *antisymmetric* vector. Using equations A.17, A.19 and A.20, we find

$$\langle \lambda_i | \hat{q} | \lambda_j \rangle = \langle \lambda_i | \hat{U}^\top \hat{U} \hat{q} \hat{U}^\top \hat{U} | \lambda_j \rangle = \chi_i \chi_j \chi_{\hat{q}} \langle \lambda_i | \hat{q} | \lambda_j \rangle. \quad (\text{A.21})$$

For a nonzero matrix element $\langle \lambda_i | \hat{q} | \lambda_j \rangle$, this equation can be fulfilled only if $\chi_i \chi_j \chi_{\hat{q}} = 1$. Consequently, the matrix elements of a *symmetric* operator \hat{q} , where $\chi_{\hat{q}} = 1$ vanish whenever the eigenvectors $|\lambda_i\rangle$ and $|\lambda_j\rangle$ have different symmetry properties under the transformation \hat{U} . Conversely, for an *antisymmetric* operator ($\chi_{\hat{q}} = -1$) all matrix elements between eigenvectors of equal symmetry must be zero.

A.1.4 Application to two-dimensional lattice systems

Now we apply this formalism to a special class of models which are defined on a two-dimensional square lattice. Each lattice site can be in one of n different states. There are interactions only between nearest neighbour and diagonal neighbour sites. The models discussed in section 2 belong to this class. We consider a rectangular system with an extension

of L lattice constants in the x -direction and N lattice constants in the y -direction as shown in figure A.1a. The boundary conditions are assumed to be periodic.

To investigate the limit $N \rightarrow \infty$ of an infinite strip with the transfer matrix method, we decompose this system into slices which consist of a single line of sites in the x -direction. The configuration X of such a line is determined by the states of the L sites (x_1, x_2, \dots, x_L) . Since there are n possibilities for each of the x_i , we have $\tilde{n} = n^L$ different configurations of a line. The transfer matrix formalism requires a mapping of these configurations to a set of vectors such that $\langle X|Y \rangle = \delta_{x_1, y_1} \cdot \delta_{x_2, y_2} \cdots \delta_{x_L, y_L}$ for any two vectors $|X\rangle, |Y\rangle$ which represent configurations X, Y . For this purpose, we introduce real n^L -dimensional unit vectors

$$|X\rangle = \left(\delta_{1, \zeta(X)}, \delta_{2, \zeta(X)}, \dots, \delta_{n^L, \zeta(X)} \right)^\top, \quad (\text{A.22})$$

where $\zeta(X)$ is a function which maps each configuration uniquely to an integer $\in \{1, \dots, n^L\}$. To define such a function, we assume without loss of generality that the x_i can have values from 0 to $n - 1$. Then, we can read each configuration of a line as a number $\in \{0, \dots, n^L - 1\}$ written in a positional notation with radix n . Consequently,

$$\zeta(X) = 1 + \sum_{i=1}^L x_i n^{i-1} \quad (\text{A.23})$$

has the desired properties. It is convenient to use the notation $|X\rangle \equiv |x_1, \dots, x_L\rangle$ which shows the configuration of the line that is represented by $|X\rangle$ directly. Note, that the x_i are *not* the components of $|X\rangle$!

The Hamiltonian of the system can be written in the form of equation A.1, where

$$\tilde{H}(X, Y) = h(x_L, x_1, y_L, y_1) + \sum_{i=1}^{L-1} h(x_i, x_{i+1}, y_i, y_{i+1}). \quad (\text{A.24})$$

Here, $h(v, w, x, y)$ is the total energy of a unit cell as shown in figure A.1b. Inserting equation A.24 into equation A.4, we obtain the transfer matrix

$$T = \sum_{|X\rangle, |Y\rangle} |x_1, \dots, x_L\rangle t(x_L, x_1, y_L, y_1) \prod_{i=1}^{L-1} t(x_i, x_{i+1}, y_i, y_{i+1}) \langle y_1, \dots, y_L|, \quad (\text{A.25})$$

where we have introduced $t(v, w, x, y) = \exp(-\beta h(v, w, x, y))$.

We are interested in the extremal eigenvalues of T and the corresponding eigenvectors. Since T is a $n^L \times n^L$ matrix, the number of its elements, n^{2L} , increases extremely fast with L . Therefore, any approach where the transfer matrix is stored in computer memory is limited to very small strip widths L . However, there are algorithms for the computation of extremal eigenvalues which do not need the matrix itself but only a method to compute the product of the investigated matrix with an arbitrary column vector. One of these is the Lanczos algorithm which we use in this work. We refer the reader to the numerical literature [114] for a description of this method. In this context, it is important to note that the transfer matrix can be written as a product of L matrices which are extremely sparse [78, 120]:

$$T = T_L T_{L-1} \cdots T_1 \quad (\text{A.26})$$

The $n^{L+2} \times n^L$ matrix

$$T_1 = \sum_{|X\rangle} \sum_{y_1, y_{L+2}} |y_1, x_1, \dots, x_L, y_{L+2}\rangle t(y_{L+2}, y_1, x_L, x_1) \langle x_1, \dots, x_L| \quad (\text{A.27})$$

maps the n^L -dimensional space which is spanned up by the vectors $\{|x_1, \dots, x_L\rangle\}$ to a n^{L+2} -dimensional space. An orthonormal base which spans up this space can be constructed using a mapping of the configurations of a line of $L + 2$ sites to vectors similar to that defined in equations A.22 and A.23. The matrix elements are then defined in terms of the configuration both of the line of L sites and the line of $L + 2$ sites. Note, that T_1 has only $n^2 \cdot n^L$ nonzero elements. Similarly, we have $L - 2$ matrices of dimension $n^{L+2} \times n^{L+2}$

$$T_i = \sum_{|X\rangle} \sum_{y_i} |x_1, \dots, x_{i-1}, y_i, x_{i+1}, \dots, x_{L+2}\rangle t(x_{i-1}, y_i, x_i, x_{i+1}) \langle x_1, \dots, x_{L+2}| \quad (\text{A.28})$$

where $i = 2, \dots, L - 1$. Each of these matrices has $n \cdot n^{L+2}$ nonzero elements. Finally, we have the $n^L \times n^{L+2}$ matrix

$$T_L = \sum_{|X\rangle} |x_1, \dots, x_{L-1}, x_{L+2}\rangle t(x_{L-1}, x_{L+2}, x_2, x_{L+1}) \langle x_1, \dots, x_{L+2}| \quad (\text{A.29})$$

which has n^{L+2} nonzero elements. It is easy but lengthy to verify that the product of these matrices yields the transfer matrix. Using a sparse representation, we need to keep only the nonzero elements to store the T_i in computer memory. The T_i altogether have $n^{L+2} [2 + (L - 2)n]$ nonzero elements, which is significantly less than the n^{2L} elements of T itself. Since the product of the transfer matrix with an arbitrary vector $|v\rangle$ can be performed by successively multiplying $|v\rangle$ with the T_i , we can save a great amount of memory and CPU time by using this factorization. On our computer equipment, we can deal with strip widths up to $L = 18$ for $n = 2$ and $L = 10$ for $n = 3$.

A.2 Finite size scaling

Using the transfer matrix formalism, the thermodynamic properties of semi-infinite systems can be calculated exactly. However, we are interested in the thermodynamic limit of a system which is infinite in *all* directions. In particular, we want to study the phase transitions of the infinite system. A phase transition is an abrupt change of the order of the system in dependence of a parameter like temperature. At continuous transitions and first order transitions which are investigated in this thesis, the correlation length diverges to infinity. Additionally, there is a singularity in the free energy. From equation A.16, it follows that a diverging correlation length requires a degenerate greatest eigenvalue of the transfer matrix. Consequently, there are no phase transitions in semi-infinite systems since there the greatest eigenvalue of the transfer matrix is always nondegenerate. On the other hand, it is reasonable to assume that we can draw conclusions on the infinite system from results obtained for a semi-infinite system with sufficiently large slices. The theory of finite size scaling describes how this can be done. The procedure is different for continuous phase transitions and first order transitions.

A.2.1 Continuous phase transitions

In continuous phase transitions, the order parameter m which measures the order of the system decreases continuously to zero as the critical temperature T_c is approached from below. There is no latent heat and no interface tension between the low temperature phase and the high temperature phase. The description of this kind of transition is based on the observation that the system is self-similar at the critical point, i.e. the statistical features are invariant under rescaling. The method which is presented in this section has been suggested by Nightingale [77, 78] as “phenomenological renormalization group theory”.

We introduce the parameter $\epsilon := T - T_c$ ¹. Additionally, we consider an ordering field h which couples to the order parameter m . Then, in the infinite system the critical point is at $\epsilon = h = 0$. For simplicity, we assume an equal system size L in all finite directions. We divide the system into hypercubes with a linear dimension of b lattice sites. For small enough ϵ, h we have $b \ll \xi$. We map each block to a single site in a system of size L/b which might be done e.g. by a majority decision among the sites in the block. Following renormalization group theory, the free energy of the interactions between the blocks can be approximated by the free energy of the rescaled system at a different temperature ϵ_b and field h_b . Then, the total free energy per block is

$$b^d f(\epsilon, h, 1/L) = b^d g_b(\epsilon, h, 1/L) + f(\epsilon_b, h_b, b/L). \quad (\text{A.30})$$

d is the dimension of the system. The first term on the right hand side of this equation is the free energy of the interactions between the sites in the block. Since b is finite, it is analytical even at the critical point where $\epsilon = h = 0$ and $L = \infty$. All free energies have been expressed in terms of free energy densities per site. It is convenient to define the free energy as a function of the *inverse* system size. Then, at the critical point all arguments of f are zero. Clearly, the correlation length in the rescaled system is by a factor $1/b$ smaller than in the original system such that

$$\xi(\epsilon, h, 1/L) = b\xi(\epsilon_b, h_b, b/L). \quad (\text{A.31})$$

A simple consideration yields the functional dependence of ϵ_b and h_b on ϵ and h . We iterate the rescaling procedure by dividing the *rescaled* system into blocks of size b' . Clearly, this should yield the same result as a division of the original system into blocks of size bb' : $\epsilon_{b'}(\epsilon_b(\epsilon)) = \epsilon_{b'b}(\epsilon)$ and $h_{b'}(h_b(h)) = h_{b'b}(h)$. This group property is fulfilled if

$$\begin{aligned} \epsilon_b(\epsilon) &= b^{y_T} \epsilon \\ h_b(h) &= b^{y_h} h \end{aligned} \quad (\text{A.32})$$

with scaling exponents y_T and y_h . These exponents characterize the *universality class* of the model. Note, that formally the inverse system size enters the free energy and the correlation length like a field which drives the system away from the phase transition. The corresponding scaling exponent is one.

One can show [78] that the free energy can be decomposed into a singular and a regular part $f = f_{\text{sing}} + f_{\text{reg}}$. f_{reg} is analytical even at the critical point. Close to the phase transition, the behaviour of the system is dominated by the singular part f_{sing} which fulfils

$$b^d f_{\text{sing}}(\epsilon, h, 1/L) = f_{\text{sing}}(b^{y_T} \epsilon, b^{y_h} h, b/L). \quad (\text{A.33})$$

¹In principle, the temperature might be replaced by any other parameter which can be tuned to reach the critical point, e.g. a chemical potential.

The second derivatives of this equation with respect to ϵ and h , respectively, yield similar scaling forms for the specific heat c_L and the susceptibility χ_L of m . From these, we obtain how the singularities of c_L and χ_L build up as L goes to infinity:

$$c_L \propto f_{\epsilon\epsilon}(0, 0, 1/L) \sim L^{2y_T-d} \quad (\text{A.34})$$

$$\chi_L \propto f_{hh}(0, 0, 1/L) \sim L^{2y_h-d}. \quad (\text{A.35})$$

Using equations A.31 and A.32, we obtain the scaling behaviour of the inverse correlation length $\kappa := \xi^{-1}$:

$$b\kappa(\epsilon, h, 1/L) = \kappa(b^{y_T}\epsilon, b^{y_h}h, b/L). \quad (\text{A.36})$$

Consequently, at $\epsilon = h = 0$ the inverse correlation length, its derivative with respect to temperature and its second derivative with respect to the field h behave like

$$\kappa(0, 0, 1/L) \sim L^{-1} \quad (\text{A.37})$$

$$\kappa_\epsilon(0, 0, 1/L) \sim L^{y_T-1} \quad (\text{A.38})$$

$$\kappa_{hh}(0, 0, 1/L) \sim L^{2y_h-1}. \quad (\text{A.39})$$

In equation A.39, we have assumed $h \leftrightarrow -h$ symmetry of the investigated model such that the first derivative of κ with respect to h vanishes. These properties are sufficient to determine the critical temperature and the scaling exponents y_T and y_h . To this end, we measure the inverse correlation lengths $\kappa^{(1)}$, $\kappa^{(2)}$ at zero field for two different strip widths $L^{(1)}$ and $L^{(2)}$ as a function of temperature. Due to equation A.37, T_c is the temperature where $\kappa^{(1)}L^{(1)} = \kappa^{(2)}L^{(2)}$. Once T_c is known, y_T and y_h can be determined from equations A.38 and A.39. At T_c , we have

$$y_T = \ln \left(\frac{L^{(1)}\kappa_\epsilon^{(1)}}{L^{(2)}\kappa_\epsilon^{(2)}} \right) \left[\ln \left(\frac{L^{(1)}}{L^{(2)}} \right) \right]^{-1} \quad \text{and} \quad y_h = \frac{1}{2} \ln \left(\frac{L^{(1)}\kappa_{hh}^{(1)}}{L^{(2)}\kappa_{hh}^{(2)}} \right) \left[\ln \left(\frac{L^{(1)}}{L^{(2)}} \right) \right]^{-1}. \quad (\text{A.40})$$

A.2.2 First order phase transitions

At a first order phase transition, there is a discontinuity both in energy and the order parameter. The energy difference between the high temperature phase and the low temperature phase is called *latent heat*. Additionally, there is an *interface tension* between the phases. Since the surface of a phase and its volume scale differently if the rescaling procedure introduced in chapter A.2.1 is applied, this interface energy forbids self-similar properties of the system. It is connected with the phenomenon of *metastability*: The low (high) temperature phase is insensitive to *small* perturbations even at temperatures above (below) the transition temperature. Due to the interface tension, small droplets of the stable phase in the unstable phase are unfavourable. At the transition temperature, the system will spontaneously order in one of the phases unless this is impossible due to some constraint, e.g. a fixed particle number. In that case, the coexisting phases are separated and exist in different parts of the system.

The description of these phenomena requires an extension of the concept of free energy. Conventionally, the free energy is defined as a thermodynamic potential which characterizes the state of the *system*. In the theory of phase equilibria [92], the concept of the free energy of a *phase* is used. In the thermodynamic limit, the free energy of the system is then assumed to be the sum of the free energies of all coexisting phases. In the following paragraph, we discuss the connection of this idea with the transfer matrix formalism.

Phases and asymptotically degenerate eigenvalues

Due to the dependence of the correlation length on the eigenvalues of T in a finite system (equation A.6), one might expect that in the thermodynamic limit the greatest eigenvalue of the transfer matrix becomes degenerate at a phase transition. However, the transfer matrix of an infinite system is ill-defined. Since energy and free energy are extensive, $\tilde{H}(X, Y)$ and the free energy per slice grow proportional to the number of sites per slice, \mathcal{M} . Therefore, some elements and eigenvalues of T go to infinity as $L \rightarrow \infty$. To avoid this mathematical problem, we define the quantities

$$f_i := \frac{-1}{\beta\mathcal{M}} \ln |\lambda_i| \quad \text{for } i = 1, \dots, \tilde{n}. \quad (\text{A.41})$$

The eigenvalues λ_i are assumed to be sorted in descending order. For $L \rightarrow \infty$, f_1 converges to the free energy per site of the infinite system. Consider a system at a phase transition. Quite generally, we assume that there are ν positive eigenvalues $\lambda_1 > \lambda_2 \geq \dots \geq \lambda_\nu$ and μ negative eigenvalues $\lambda_{\tilde{n}} \leq \lambda_{\tilde{n}-1} \leq \dots \leq \lambda_{\tilde{n}-\mu+1}$ such that

$$\xi_i^{-1} := \ln \left(\left| \frac{\lambda_1}{\lambda_i} \right| \right) = -\beta\mathcal{M} (f_1 - f_i) \xrightarrow{L \rightarrow \infty} 0 \quad (\text{A.42})$$

for $i \leq \nu$ and $i > \tilde{n} - \mu$. In the following, we will denote these eigenvalues as ‘‘asymptotically degenerate’’. Each of the ξ_i might be the diverging correlation length of an appropriately chosen quantity.

We investigate the influence of a perturbing field h which couples to the extensive quantity $N\mathcal{M}q$. q is an arbitrary intensive quantity the operator of which is \hat{q} . This field drives the system away from the phase transition at $h = 0$. In the remainder of this paragraph it is assumed that $|h|$ is so small that terms of order h^2 and higher orders in h can be neglected. Variables which refer to the perturbed system are marked with a prime. The transfer matrix is

$$\begin{aligned} T' &= \sum_{|X\rangle, |Y\rangle} |X\rangle \exp \left[-\beta \left(\tilde{H}(X, Y) - \frac{h\mathcal{M}}{2} (q(X) + q(Y)) \right) \right] \langle Y| \\ &= \sum_{|X\rangle, |Y\rangle} |X\rangle \left[1 + \frac{\beta h\mathcal{M}}{2} (q(X) + q(Y)) \right] \exp \left[-\beta \tilde{H}(X, Y) \right] \langle Y| \\ &= T + \frac{\beta h\mathcal{M}}{2} (\hat{q}T + T\hat{q}). \end{aligned} \quad (\text{A.43})$$

According to perturbation theory, for small L the greatest eigenvalue of T' is $\lambda'_1 = \langle \lambda_1 | T' | \lambda_1 \rangle + \mathcal{O}(h^2)$. However, for large L the gap between the greatest eigenvalue of T and the asymptotically degenerate eigenvalues becomes smaller. For any small but finite h , there will be some value of L where the perturbation induced by h is comparable to the separation between the eigenvalues. In this case, the eigenvector $|\lambda'_1\rangle$ to the greatest eigenvalue of T' will be the linear combination of the eigenvectors to the asymptotically degenerate eigenvalues of T which maximizes $\langle \lambda'_1 | T' | \lambda'_1 \rangle$. We make the ansatz

$$|\lambda'_1\rangle = \sum_{k=1}^{\nu+\mu} c_k |\lambda_{z(k)}\rangle \quad (\text{A.44})$$

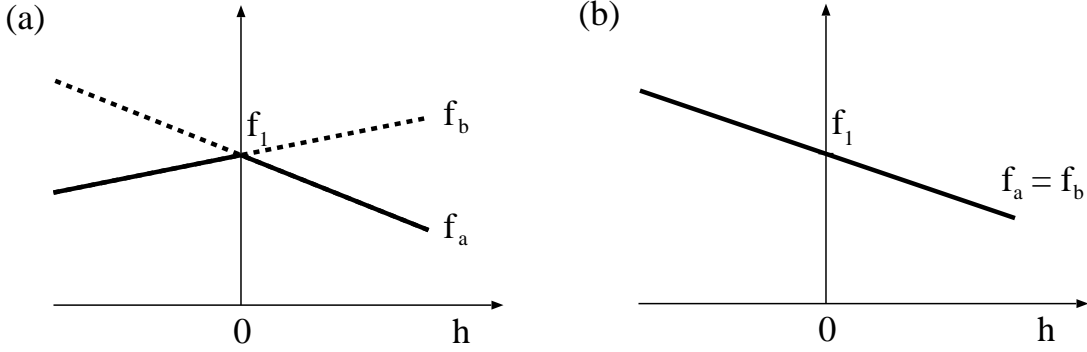


Figure A.2: Sketch of the behaviour of f'_1 at a phase transition where $\nu + \mu = 2$ in the limit $L \rightarrow \infty$. Panel (a): First order phase transition. The solid line shows the free energy of the system. At the phase transition ($h = 0$), there is a discontinuity in $\partial f'_1 / \partial h$. The dashed lines show the continuation of the free energies of the phases into the regions of metastability. Panel (b): Continuous phase transition. At $h = 0$, the first derivative of f'_1 is continuous.

energy of phase (b) should be f_b . We expect that both phases are metastable in the region where they are thermodynamically unstable. Since there is no singularity in the free energy of a phase at the transition (in contrast to the free energy of the system), the free energies of the phases in the metastable region should be given by the continuation of f_a and f_b .

Generalizing this idea, we find that in the vicinity of a first order phase transition the free energies of the metastable phases are functions of those eigenvalues of the transfer matrix which are asymptotically degenerate at the phase transition. The number of these eigenvalues equals the number of coexisting phases at the transition itself. For example, at a triple point we expect $\nu + \mu = 3$.

Application to semi-infinite systems

At continuous transitions, the inverse system size enters the free energy like a field which drives the system away from the phase transition. According to Privman, Fisher and Schulman [89, 90], a similar analogy holds in the vicinity of a first order transition. They argue, that the f_i of a semi-infinite system can be calculated from measurements of an infinite system via a perturbation theory similar to that presented in the preceding paragraph. The finiteness of the system size plays the role of a perturbing field. Consequently, the free energy per site in a semi-infinite system is the smallest eigenvalue of a $(\nu + \mu) \times (\nu + \mu)$ - dimensional free energy matrix which has the same structure as Q in equation A.47. Its diagonal elements are the free energies per site of the phases which coexist at the transition. The off-diagonal elements determine the finite size corrections. Since there is no mixing between positive and negative eigenvalues, the free energy matrix can be diagonalized blockwise.

In the models which are discussed in this thesis, we have to deal with lines of triple points, lines of points where four phases coexist and, in the model of the CdTe(001) surface with Te dimerization, a point where five phases coexist. In our investigations, the system is arranged such that the repulsive interactions are in the infinite direction. Then, neighbouring slices are anticorrelated which implies negative asymptotically degenerate eigenvalues. We find, that whenever the number of coexisting phases is ≤ 4 , there are at most two positive and

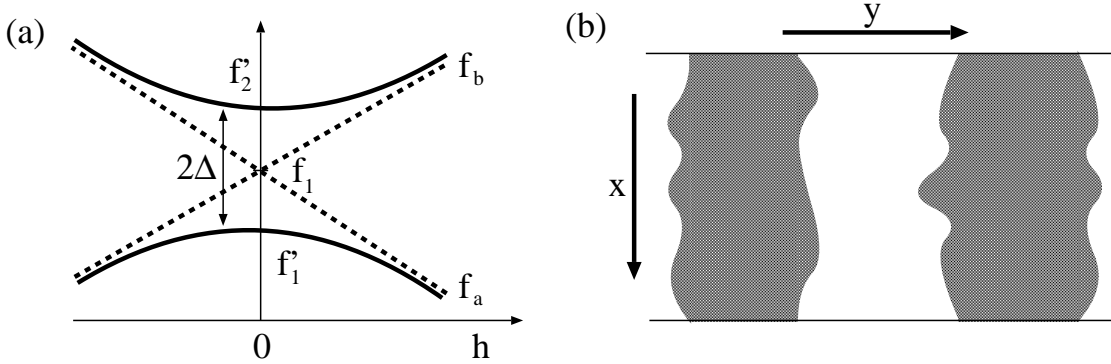


Figure A.3: Panel (a): Schematic behaviour of the f_i at a finite strip width L . The dashed lines show the free energies f_a , f_b of the phases of the infinite system. Panel (b): Sketch of a semi-infinite system at the phase transition of the infinite system. White and grey areas symbolize two coexisting phases.

two negative eigenvalues which are asymptotically degenerate. In the following, we restrict ourselves to this case. The point where 5 phases coexist can be found from the intersection of lines of other phase transitions. Due to the theorem of Perron-Frobenius, f_1 is the smallest eigenvalue of the positive block of the free energy matrix which has the form

$$\begin{pmatrix} f_a & \Delta \\ \Delta & f_b \end{pmatrix}. \quad (\text{A.50})$$

Its eigenvalues are

$$f_{1,2} = -\frac{1}{\beta\mathcal{M}} \ln \lambda_{1,2} = \frac{1}{2}(f_a + f_b) \mp \frac{1}{2}\sqrt{(f_a - f_b)^2 + 4\Delta^2}. \quad (\text{A.51})$$

At the phase transition, we have $f_a = f_b$. Then, the inverse correlation length is $\xi^{-1} = \ln |\lambda_1/\lambda_2| = 2\beta\Delta$. Further away from the phase transition, where $|f_a - f_b| \gg \Delta$, f_1 approaches to the minimum of f_a and f_b (figure A.3a).

Since Δ is a function of the correlation length at the phase transition, we can determine the functional form of the dependence of the finite size corrections on L from an estimation of ξ . In a semi-infinite system, there is no spontaneous symmetry breaking at the transition temperature of the infinite system. Instead, the system consists of alternating domains of the coexisting phases. A sketch of such a system is shown in figure A.3b. The correlation length is proportional to the typical distance between two domain walls. Due to the interface tension σ , the formation of such a domain wall costs a free energy $\alpha L\sigma$, where α is a dimensionless number $\mathcal{O}(1)$. Consequently, the probability for the formation of a domain wall is proportional to $\exp(-\beta\alpha L\sigma)$. Therefore, we have

$$\xi \propto \exp(\beta\alpha L\sigma) \implies \Delta \propto \exp(-AL) \quad \text{where } A = \beta\alpha\sigma. \quad (\text{A.52})$$

Since the behaviour of all other quantities depends on the free energy, an exponential decay of the finite size corrections should be a generic feature of first order phase transitions. However, frequently one encounters the phenomenon of a *tricritical point* at a temperature T_{tri} . At T_{tri} , the nature of the phase transition changes from first order at $T < T_{\text{tri}}$ to a continuous

Appendix B

Continuous time Monte Carlo simulations

A large number of Monte Carlo algorithms is based on the mathematical concept of *Markov chains* [76]. In all the simulations presented in this thesis, such methods were used. Consider a system with a finite set \mathcal{S} of possible states s . A Markov chain is a stochastic process in discrete timesteps which is characterized completely by a set of transition probabilities $\{W_{s \rightarrow s'} | s, s' \in \mathcal{S}\}$, where $W_{s \rightarrow s'}$ is the conditional probability to find the system in state s' at step $n + 1$ given that it is in state s at step n .

In equilibrium simulations one is interested in the calculation of averages over an ensemble of states distributed according to some probability distribution function $P(s)$. Of course, the most important example is the Gibbs distribution

$$P(s) = \frac{\exp[-H(s)/(kT)]}{\sum_s \exp[-H(s)/(kT)]},$$

where $H(s)$ is the energy of the system in state s , k is Boltzmann's constant and T is temperature. The idea is to construct a Markov chain, where *time averages* over this sequence of states converge to *ensemble averages* over $P(s)$ in the limit of infinite time. The first condition for this to be the case is that every state s of the system with $P(s) > 0$ can be reached within a finite number of steps from every initial configuration. A dynamics with this property is called *ergodic*. The second condition is that $P(s)$ is *stationary* under the dynamics. Consider an ensemble of Markov chains. Let $P_n(s)$ denote the probability of a randomly chosen member of such an ensemble to be in state s at time step n . The change of this probability in the next step is then given by

$$P_{n+1}(s) - P_n(s) = \sum_{s' \neq s} W_{s' \rightarrow s} P_n(s') - \sum_{s' \neq s} W_{s \rightarrow s'} P_n(s). \quad (\text{B.1})$$

The first sum is the total probability to enter state s in step n , the second sum is the total probability to leave state s . A distribution is stationary, if the left hand side of this equation is zero. In particular, this is the case if the transition probabilities fulfil a detailed balance condition

$$W_{s \rightarrow s'} P(s) = W_{s' \rightarrow s} P(s'). \quad (\text{B.2})$$

In case of a Gibbs distribution, this condition yields

$$\frac{W_{s \rightarrow s'}}{W_{s' \rightarrow s}} = \exp\left(-\frac{H(s) - H(s')}{kT}\right). \quad (\text{B.3})$$

Since there is no unique solution of equation B.3, there is some freedom in the choice of transition probabilities in simulations of thermal equilibrium. In particular, there is no need to choose the $W_{s \rightarrow s'}$ in agreement with the physical dynamics of the system.

In the simulation of systems far from equilibrium like crystal growth or sublimation one is interested in the evolution of the state of the system with time. If we look at the state of the system on a coarse-grained scale in discrete time intervals of appropriate length, we can describe its evolution by a Markov process. The transition probabilities depend on the chaotic microscopic motion of atoms (section 1.4). Therefore, the $W_{s \rightarrow s'}$ must reflect the physics of the investigated system. However, in the absence of external forces any physical system will finally reach thermal equilibrium. Therefore, any reasonable choice of the dynamics of the *isolated* system must fulfil *at least* the conditions of ergodicity and the stationarity of the Gibbs distribution. The simplest way to ensure the latter condition is to make an ansatz for the $W_{s \rightarrow s'}$ in agreement with the detailed balance condition B.3.

It is favourable to express the transition probabilities in terms of events which modify the system. Such events might be e.g. diffusion hops of atoms on a crystal surface or spin flips in an Ising model. In general, let there be a system where \mathcal{N} events $i = 1, \dots, \mathcal{N}$ are possible. There is a *rate* $\rho_i(s)$ for every event, which is a function of the actual state s of the system. We introduce the transition probabilities

$$W_{s \rightarrow s'} = \begin{cases} \frac{\rho_{i(s \rightarrow s')}(s)}{\mathcal{N}\rho_0} & \text{if } s \neq s' \text{ and } i(s \rightarrow s') \text{ exists} \\ 1 - \sum_{i=1}^{\mathcal{N}} \frac{\rho_i(s)}{\mathcal{N}\rho_0} & \text{if } s = s' \\ 0 & \text{otherwise} \end{cases}, \quad (\text{B.4})$$

where ρ_0 is a constant such that $\rho_0 \geq \max_i \rho_i$. Event $i(s \rightarrow s')$ changes the state of the system from s to s' . These $W_{s \rightarrow s'}$ fulfil the conditions $W_{s \rightarrow s'} \geq 0$ and $\sum_{s'} W_{s \rightarrow s'} = 1$ for probabilities. Detailed balance is fulfilled if $\rho_{i(s \rightarrow s')}/\rho_{i(s' \rightarrow s)} = P(s)/P(s')$.

These transition probabilities describe the dynamics of a stochastic system with independent events if the probability that two or more events occur simultaneously in the physical time interval Δt between subsequent Markov steps can be neglected. The probability of a random event with rate $\rho_i(s)$ to happen in a time interval Δt is $\rho_i(s)\Delta t$. Identifying this with the corresponding transition probability we find

$$\Delta t = \frac{1}{\mathcal{N}\rho_0}. \quad (\text{B.5})$$

Clearly, the probability for two or more events in Δt decreases $\sim 1/\rho_0^2$ as ρ_0 is increased. In continuous time algorithms, we can perform the limit $\rho_0 \rightarrow \infty$ exactly, such that there are no problems due to simultaneous events.

B.1 Fundamental algorithms

In the Markov chain defined in equation B.4, there are two different classes of steps: On the one hand, there are steps in which the state of the system changes. In the following, we will denote these as “modifying steps”. On the other hand, there are steps in which the state of the system remains the same (non-modifying steps). Especially at low temperature the probability $W_{s \rightarrow s}$ of a non-modifying step usually is high. This leads to a considerable slowing down of simple techniques like the Metropolis algorithm which simulate the Markov chain directly.

Continuous time algorithms [18, 64, 76] avoid this problem. The basic idea is to jump over the non-modifying steps. In every iteration of the algorithm one event is selected randomly with the conditional probability $\tilde{P}_i(s)$ that event i is performed in a Markov step *given* that this is a modifying step. Then, the number n_p of Markov steps which pass before the next modifying step is drawn randomly according to the probability of non-modifying steps. This procedure yields the correct statistics of the Markov chain, if quantities measured in the actual state of the system are weighted with n_p or, equivalently, with the corresponding physical time interval. According to equation B.4, the probability of a modifying step is

$$P_m(s) = 1 - W_{s \rightarrow s} = \frac{R(s)}{\mathcal{N}\rho_0} \quad \text{where} \quad R(s) = \sum_{i=1}^{\mathcal{N}} \rho_i(s). \quad (\text{B.6})$$

Using this equation, we can calculate $\tilde{P}_i(s)$. The probability that event i is performed in one Markov step is

$$P_i(s) = \frac{\rho_i(s)}{\mathcal{N}\rho_0} = P_m(s) \frac{\rho_i(s)}{R(s)} = P_m(s) \tilde{P}_i(s).$$

Consequently,

$$\tilde{P}_i(s) = \frac{\rho_i(s)}{R(s)}. \quad (\text{B.7})$$

The probability of a specific value of n_p is the probability of a sequence of $n_p - 1$ non-modifying steps followed by one modifying step which is

$$P(n_p, s) = (1 - P_m(s))^{n_p - 1} P_m(s). \quad (\text{B.8})$$

To perform the limit $\rho_0 \rightarrow \infty$, we express n_p in terms of the physical time interval $\tau = n_p \Delta t = n_p / (\mathcal{N}\rho_0)$ which passes between subsequent modifying steps. Then, the probability distribution function of τ is

$$P(\tau, s) d\tau = \lim_{\rho_0 \rightarrow \infty} \left(1 - \frac{R(s)}{\mathcal{N}\rho_0} \right)^{\mathcal{N}\rho_0 \tau} R(s) d\tau = R(s) \exp(-R(s)\tau) d\tau, \quad (\text{B.9})$$

where we have used equations B.6 and B.8.

Algorithm B.1 *Continuous time Monte Carlo simulation*

1. Draw an event i randomly with probability $\tilde{P}_i(s)$ and perform it. This changes the state s of the system.
2. Calculate the $\rho_i(s)$ and $R(s)$ in the new state of the system. If the event changes the state of the system only locally and the range of interactions is short, $\rho_i(s)$ changes only for a few i .
3. Draw a uniformly distributed random number $\chi \in]0, 1]$ and increase the system time by $\tau = -\ln \chi / R(s)$. τ is a random number distributed according to equation B.9. In the calculation of thermal averages, weight the quantities measured in the current state of the system with τ .
4. Go to step 1 unless some condition to terminate is fulfilled (e.g. a maximum number of steps is done).

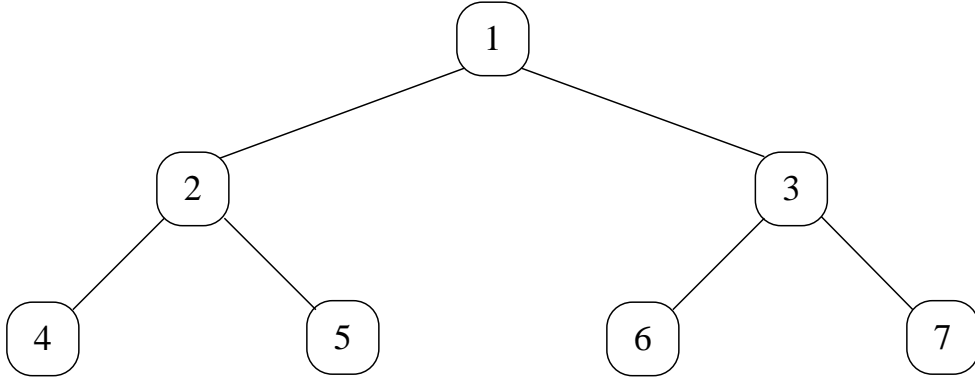


Figure B.1: Sketch of a complete binary tree.

To apply this algorithm, we need fast methods to perform the random selection of events in step 1 and the update of the rates in step 2. We first introduce algorithms which perform both tasks in $\mathcal{O}(\log_2 \mathcal{N})$ time [17]. They can be applied in the general case where there is a unique rate for every event.

We use a *complete binary tree* [53] to store the list of the rates of all events. Formally, a *binary tree* is defined as a finite set of nodes that either is empty, or consists of a root node and the elements of two disjoint binary trees which are called the left and the right subtree of the root. The root nodes of the subtrees of a node are commonly denoted as its “children”. Conversely, the node a node is child of is called its “parent”.

Usually, a binary tree is drawn with the root node on top. Lines connect every node with its children. Such a sketch of a binary tree is shown in figure B.1. There is a simple way to enumerate the nodes of a binary tree. The root node gets index 1. In general, node k has the left child $2k$ and the right child $2k + 1$. Then, the parent of node k is $\lfloor k/2 \rfloor$. A binary tree is called *complete* if this enumeration maps its nodes to a set of consecutive integers. The tree shown in figure B.1 is such a complete binary tree. We use this enumeration to store a complete binary tree in a linear array in computer memory.

In our Monte Carlo simulations, we use a complete binary tree with \mathcal{N} nodes, where \mathcal{N} is the maximum number of events. Each node k is attributed to a specific event. There are three real numbers for each node: $w_k = \rho_k(s)$ is the rate of event k in the current state of the system. l_k is the sum of the rates of all nodes in the left subtree of node k and r_k is the sum of all rates in the right subtree of node k . Using these quantities, the sum of all rates is $R(s) = w_1 + l_1 + r_1$. Formally, we define $w_k = l_k = r_k = 0$ for all $k > \mathcal{N}$. Then, $l_k = w_{2k} + l_{2k} + r_{2k}$ and $r_k = w_{2k+1} + l_{2k+1} + r_{2k+1}$. The following algorithm selects a random event by climbing down the tree. The index k points to the current node.

Algorithm B.2 *Selection of events with probability $\tilde{P}_k(s) = w_k / (w_1 + l_1 + r_1)$*

1. Draw a uniformly distributed random number $\xi \in [0, w_1 + l_1 + r_1[$. Set $k \leftarrow 1$ (Start at the root node).
2. If $\xi < l_k$, then set $k \leftarrow 2k$, i.e. go to the left child. Else, if $\xi < l_k + w_k$ return event k . In this case, the algorithm is done. Else, go to the right child and adjust ξ such that $0 \leq \xi < r_k$: $k \leftarrow 2k + 1$, $\xi \leftarrow \xi - l_k - w_k$.

3. Go to step 2.

The proof that algorithm B.2 is correct is by induction. Whenever the algorithm enters node k in step 2, the actual value of ξ is a uniformly distributed random number $\in [0, w_k + l_k + r_k[$. This is ensured by the initialization in step one and the adjustment in step 2. Therefore, the algorithm terminates with probability $w_k/(w_k + l_k + r_k)$. The probabilities to go to the left and the right child are $l_k/(w_k + l_k + r_k)$ and $r_k/(w_k + l_k + r_k)$, respectively. In particular, the probability to terminate at the root is $w_1/(w_1 + l_1 + r_1)$. This is the basis of induction. Node k is a child of node $m = \lfloor k/2 \rfloor < k$. By induction, the algorithm terminates in node m with the correct probability, which can only be the case if the algorithm enters node m with probability $(w_m + l_m + r_m)/(w_1 + l_1 + r_1)$. The probability to go from node m to node k is $(w_k + l_k + r_k)/(w_m + l_m + r_m)$. Therefore, the probability to terminate in node k is

$$\frac{w_m + l_m + r_m}{w_1 + l_1 + r_1} \cdot \frac{w_k + l_k + r_k}{w_m + l_m + r_m} \cdot \frac{w_k}{w_k + l_k + r_k} = \frac{w_k}{w_1 + l_1 + r_1}. \quad \text{q.e.d.}$$

In each iteration where the algorithm does not terminate, one half of the events in the subtrees of node k are ruled out. Therefore, the average running time of the algorithm is $\mathcal{O}(\log_2 \mathcal{N})$.

In step 2 of algorithm B.1, the tree must be updated to reflect the changes in the $\rho_i(s)$. To do this for one event, we set $w_i = \rho_i(s)$. Then, the l_k and r_k of the parents of node i must be adjusted. This is done by the following algorithm which, on average, requires $\mathcal{O}(\log_2 \mathcal{N})$ iterations.

Algorithm B.3 *Update the rate of event i*

1. Start at node i . Set $k \leftarrow i$, $w_i \leftarrow \rho_i(s)$.
2. If $k = 1$, terminate. Else, go to the parent node by setting $k \leftarrow \lfloor k/2 \rfloor$.
3. Adjust l_k and r_k . Set $l_k \leftarrow w_{2k} + l_{2k} + r_{2k}$ and $r_k \leftarrow w_{2k+1} + l_{2k+1} + r_{2k+1}$.
4. Go to step 2.

If the rates of $\mathcal{O}(1)$ events change in each iteration, the time required for the complete update is $\mathcal{O}(\log_2 \mathcal{N})$.

These algorithms work in the general case where there is a unique rate for every event. However, in many lattice gas models the rate of an event depends only on the local environment of the sites which are modified by the event. Then, the number of different rates \mathcal{M} is independent of the system size and much smaller than the number of events \mathcal{N} . This feature can be exploited to make the running time both of the random selection of events and the update of data structures $\mathcal{O}(1)$. The idea is to keep *lists* of events the rates of which are equal. Consider the case where we have \mathcal{M} lists $\{l_g\}_{g=1}^{\mathcal{M}}$. If the $n_g(s)$ events in list l_g have the rate ρ_g , the total rate of these events is $R_g(s) = n_g(s)\rho_g$. The probability for one member of the list to be selected is

$$\frac{\rho_g}{R(s)} = \frac{R_g(s)}{R(s)} \cdot \frac{1}{n_g(s)}.$$

Consequently, we can perform the selection of events in a two-step process. First, we select a list l_g with probability $R_g(s)/R(s)$. This can be done with a binary tree where each node is attributed to one *list* using algorithm B.2. Then, we select one of the members of l_g randomly

with equal probability for all events. On update, events the rates of which have changed are moved to their new group. Then, the $R_g(s)$ of lists the length of which has changed are updated using algorithm B.3. Since the members of the lists can be accessed in $\mathcal{O}(1)$ time, the running time both for the selection of events and the updates is independent of \mathcal{N} . However, compared to the direct storage of the rates of events in a binary tree, the manipulation of the lists requires some computational overhead. In our experience, in a two-dimensional lattice gas at system sizes of a few hundred lattice constants, this overhead outweighs the gain of speed whenever \mathcal{M} is greater than a few dozen.

B.2 Application to lattice gases in thermal equilibrium

The application to grand-canonical simulations of the lattice gases discussed in chapter 2 is straightforward. In a model where each site is in one of n possible states $\in \{0, \dots, n-1\}$, there are $n-1$ events $m \in \{1, \dots, n-1\}$ per lattice site which change the state of the site: $x_{i,j} \leftarrow (x_{i,j} + m) \bmod n$. This can be done with Metropolis-type rates $r_{s \rightarrow s'} = \min\{1, \exp[-(H(s') - H(s))/(kT)]\}$ or symmetrical rates $r_{s \rightarrow s'} = \exp[-(H(s') - H(s))/(2kT)]$. Both possibilities fulfil the detailed balance condition B.3 and yield identical results.

A canonical simulation requires an algorithm where the number of particles is fixed. In this case, in every event one particle jumps to a different site. We choose a nonlocal dynamics where the range of particle jumps is unlimited. This yields considerably faster equilibration compared to a Kawasaki dynamics with nearest neighbour diffusion only. For simplicity, we permit only jumps to a site where the binding energy of the particle is independent of the state of its initial site, i.e. we forbid jumps to nearest and next nearest neighbour sites. If the particle jumps from site i to site j , the energy difference between the final and the initial state is $\Delta H = \Delta H_j - \Delta H_i$, where ΔH_x is the energy difference of the system with site x occupied and empty. The rates

$$r_{i \rightarrow j} = \exp [(\Delta H_i - \Delta H_j) / (2kT)] \quad (\text{B.10})$$

fulfil the detailed balance condition. Then, the probability for a jump from site i to site j factorizes, i.e.

$$p_{i \rightarrow j} = p_i^- \cdot p_j^+ \quad \text{where} \quad p_x^\pm = \frac{r_x^\pm}{\sum_x r_x^\pm}.$$

Here, we have introduced the rate for deposition of a particle at site x (r_x^+) and for removal of a particle at site x (r_x^-). $r_x^+ = \exp[-\Delta H_x/(2kT)]$ if site x is empty and zero otherwise. Conversely, $r_x^- = \exp[\Delta H_x/(2kT)]$ on occupied sites and zero on empty sites. Due to this factorization property we can proceed in two steps: In the first step, we select the site i from which the particle starts with probability p_i^- . Then, we select the site j where the particle is landing with probability p_j^+ . If the distance between site i and site j is ≥ 2 the particle is moved. Otherwise, the event is rejected and the system remains unchanged. Since the number of rejected events is small on large systems, the loss of speed can be neglected.

In our model of flat CdTe(001) surfaces only the number of Cd atoms is fixed, while the number of Te dimers may change. This requires a more elaborate algorithm which uses both canonical and grand-canonical techniques. A Cd atom may jump to any site which is not occupied by a Cd atom. If the arrival site is occupied by a dimer, the dimer is destroyed. The removal of the Cd atom at the starting site creates a pair of Te atoms. We consider both the case where these Te atoms dimerize immediately and the case where they remain

unbound. Additionally, Te dimers may break up and dimers may be created on empty sites. In the following, these processes will be denoted as “dimer flips”. In each timestep, a random number is drawn to decide whether a Cd jump with immediate formation of a dimer at the starting site, a Cd jump without dimerization or a dimer flip will occur. The probabilities are proportional to the sums of the rates of the processes in each group. A $L \times N$ system contains $\mathcal{O}(LN)$ Cd atoms and Te dimers. Thus, there are $\mathcal{O}(LN)$ dimer flip events. Since there are $\mathcal{O}(LN)$ possible arrival sites for each Cd atom, there are $\mathcal{O}(L^2N^2)$ Cd jump events. To keep the ratio of dimer flips and Cd jumps independent of the system size, the dimer flips have been weighted with a prefactor LN . Then, one event in the selected group is performed. For dimer flips, this is done with the grand-canonical algorithm while Cd jumps are performed by the canonical two-step algorithm.

B.3 Application to kinetical Monte Carlo simulations

In kinetical Monte Carlo simulations of processes like crystal growth, the set of events $i \in \{1, \dots, \mathcal{N}\}$ which can occur in a particular state of the system and their rates ρ_i are determined by the physics of the investigated model. Typically, this set of events includes the deposition of adatoms at the surface, diffusion of particles at the surface and desorption. In all full diffusion Monte Carlo simulations which are presented in this thesis, we assume that the rates of diffusion and desorption are given by the Arrhenius law 1.2. For a physically reasonable choice of the activation energies, the rates for diffusion processes fulfil the detailed balance condition B.3 such that a system where there is neither adsorption nor desorption will finally reach thermal equilibrium.

Bibliography

- [1] M. Ahr, M. Biehl. *Singularity spectra of rough growing surfaces from wavelet analysis*. Phys. Rev. E **62** (2), 1773 (2000)
- [2] M. Ahr, M. Biehl. *Modelling sublimation and atomic layer epitaxy in the presence of competing surface reconstructions*. Surf. Sci. **488** L553 (2001)
- [3] M. Ahr, M. Biehl. *Flat (001) surfaces of II-VI semiconductors: A lattice gas model*. Surf. Sci. In print.
- [4] M. Ahr, M. Biehl, M. Kinne, W. Kinzel. *The influence of the crystal lattice on coarsening in unstable epitaxial growth*. Surf. Sci. **465**, 339 (2000)
- [5] M. Ahr, M. Biehl, T. Volkmann. *Modelling (001) surfaces of II-VI semiconductors*. Comp. Phys. Comm. In print.
- [6] J. G. Amar. *Mechanisms of mound coarsening in unstable epitaxial growth*. Phys. Rev. B **60** (16), R11317 (1999)
- [7] A. Arnéodo, N. Decoster, S. G. Roux. *Intermittency, Log-Normal Statistics, and Multifractal Cascade Process in High-Resolution Satellite Images of Cloud Structure*. Phys. Rev. Lett. **83** (6) 1255 (1999)
- [8] A. Arnéodo, N. Decoster, S. G. Roux. *A Wavelet-based method for multifractal image analysis. I. Methodology and test applications on isotropic and anisotropic random rough surfaces*. Eur. Phys. J. B **15** (3), 567 (2000)
- [9] S. Arrhenius. *Über die Reaktionsgeschwindigkeit bei der Inversion von Rohrzucker durch Säuren*. Zeitschrift für physikalische Chemie **4**, 226 (1889)
- [10] E. Bacry, J. F. Muzy, A. Arnéodo. *Singularity Spectrum of Fractal Signals from Wavelet Analysis: Exact Results*. Journ. Stat. Phys. **70** (3/4) 635 (1993)
- [11] A.-L. Barabási, R. Bourbonnais, M. Jensen, J. Kertész, T. Vicsek, Y.-C. Zhang. *Multifractality of growing surfaces*. Phys. Rev. A **45** (10) R6951, (1992)
- [12] A.-L. Barabási, H. E. Stanley. *Fractal Concepts in Surface Growth*. Cambridge University Press, Cambridge (1995)
- [13] S. A. Barnett, A. Rockett. *Monte Carlo simulations of Si(001) growth and reconstruction during molecular beam epitaxy*. Surf. Sci. **198**, 133 (1988)
- [14] N. C. Bartelt, T.L. Einstein, L.D. Roelofs. *Transfer-matrix approach to estimating coverage discontinuities and multicritical-point positions in two-dimensional lattice-gas phase diagrams*. Phys. Rev. B **34**, 1616 (1986)
- [15] M. Biehl, M. Kinne, W. Kinzel, S. Schinzer. *A simple model of epitaxial growth: the influence of step edge diffusion*. in *Proceedings of the 1998 Conference on Computational Physics*. Comp. Phys. Comm. **121 - 122**, 347 (1999)

- [16] M. Biehl, M. Ahr, W. Kinzel, M. Sokolowski, T. Volkmann. *A lattice gas model of II-VI(001) semiconductor surfaces*. Europhys. Lett. **53** (2), 169 (2001)
- [17] J. L. Blue, I. Beichl, F. Sullivan. *Faster Monte Carlo simulations*. Phys. Rev. E **51** (2), R867 (1995)
- [18] A. B. Bortz, M. H. Kalos, J. L. Lebowitz. *New Algorithm for Monte Carlo Simulation of Ising Spin Systems*. J. Comput. Phys. **17**, 10 (1975)
- [19] W. J. Camp, M. E. Fisher. *Decay of Order in Classical Many-Body Systems. I. Introduction and Formal Theory*. Phys. Rev. B **6** (3), 946 (1972)
- [20] C.-S. Chin, M. den Nijs. *Reconstructed rough growing interfaces: Ridge line trapping of domain walls*. Phys. Rev. E **64**, 031606 (2001)
- [21] J. Cibert, S. Tatarenko. *The Surface Structure of a II-VI Compound: CdTe*. Defect and Diffusion Forum Vols. **150-151**, 1 (1997) and references therein
- [22] H. J. Cornelissen, D. A. Gammack, R. J. Dalby. *Reflection high-energy electron diffraction observations during growth of ZnS_xSe_{1-x} ($0 \leq x \leq 1$) by molecular-beam epitaxy*. J. Vac. Sci. Technol. B **6** (2), 769 (1988)
- [23] S. Das Sarma, C. J. Lanczycki, R. Kotlyar, S. V. Ghaisas. *Scale invariance and dynamical correlations in growth models of molecular beam epitaxy*. Phys. Rev. E **53** (1), 359 (1996)
- [24] S. Das Sarma, P. Punyindu. *Dynamic scaling in a $(2 + 1)$ -dimensional limited mobility model of epitaxial growth*. Phys. Rev. E **55** (5), 5361 (1997).
- [25] S. Das Sarma, P. Punyindu. *A discrete model for non-equilibrium growth under surface diffusion bias*. Surf. Sci. **424** (2-3), L339 (1999)
- [26] C. Dasgupta, J. M. Kim, M. Dutta, S. Das Sarma. *Instability, intermittency, and multi-scaling in discrete growth models of kinetic roughening*. Phys. Rev. E **55** (3), 2235 (1997)
- [27] B. Daudin, D. Brun-Le Cunff, S. Tatarenko. *Stoichiometry determination of the Te-rich (100) CdTe and (100) ZnTe surfaces*. Surf. Sci. **352-354**, 99 (1996)
- [28] B. Daudin, S. Tatarenko, D. Brun-Le Cunff. *Surface stoichiometry determination using reflection high-energy electron diffraction and atomic-layer epitaxy: The case of ZnTe(100)*. Phys. Rev. B **52** (11), 7822 (1995)
- [29] N. Decoster, S. G. Roux, A. Arnéodo. *A Wavelet-based method for multifractal image analysis. II. Applications to synthetic multifractal rough surfaces*. Eur. Phys. J. B **15** (4), 739 (2000)
- [30] M. den Nijs. *Preroughening of Crystal Surfaces and Energy Differences between Inside and Outside Corners*. Phys. Rev. Lett. **64** (4), 435 (1990)
- [31] I. Elkinani, J. Villain. *Growth roughness and instabilities due to the Schwoebel effect: a one-dimensional model*. J. Phys. I France **4**, 949 (1994)
- [32] J. W. Evans. *Factors mediating smoothness in epitaxial thin-film growth*. Phys. Rev. B **43** (5), 3897 (1991)

- [33] J. W. Evans, D. E. Sanders, P. A. Thiel, A. E. DePristo. *Low-temperature epitaxial growth of thin metal films*. Phys. Rev. B **41** (8), 5410 (1990)
- [34] F. Family, T. Vicsek. *Scaling of the active zone in the Eden process on percolation networks and the ballistic deposition model*. J. Phys. A **18**, L75 (1985)
- [35] W. Faschinger, H. Sitter. *Atomic-layer epitaxy of (100) CdTe on GaAs substrates*. Journ. Cryst. Growth **99**, 566 (1990)
- [36] P. J. Feibelman. *Interlayer Self-Diffusion on Stepped Pt(111)*. Phys. Rev. Lett. **81** (1), 168 (1998)
- [37] A. Garcia, J. Northrup. *First-principles study of Zn- and Se-stabilized ZnSe(001) surface reconstructions*. J. Vac. Sci. Technol. B **12**, 2678 (1994)
- [38] C. M. Gilmore, J. A. Sprague. *Molecular-dynamics simulation of the energetic deposition of Ag thin films*. Phys. Rev. B **44** (16), 8950 (1991)
- [39] S. Gundel. *ab initio-Simulationen von II-VI-Halbleitern und ZnSe-Oberflächen*. Diplomarbeit, Universität Würzburg (1997)
- [40] S. Gundel, A. Fleszar, W. Faschinger, W. Hanke. *Atomic and electronic structure of the CdTe(001) surface: LDA and GW calculations*. Phys. Rev. B **59** (23), 15261 (1999)
- [41] C. J. Hamer. *Magnetisations from finite-size scaling*. J. Phys. A **15**, L675 (1982)
- [42] C. J. Hamer. *Latent heats from finite-size scaling*. J. Phys. A **16**, 3085 (1983)
- [43] W. A. Harrison. *Theory of polar semiconductor surfaces*. J. Vac. Sci. Technol. **16** (5), 1492 (1979)
- [44] M. A. Herman, M. Sitter. *Molecular Beam Epitaxy. Fundamentals and Current Status*. 2d ed. Springer-Verlag Berlin Heidelberg New York (1996)
- [45] M. Itoh, G. R. Bell, A. R. Avery, T. S. Jones, B. A. Joyce, D. D. Vvedensky. *Island Nucleation and Growth on Reconstructed GaAs(001) Surfaces*. Phys. Rev. Lett. **81** (3), 633 (1998)
- [46] M. Itoh. *Atomic-scale homoepitaxial growth simulations of reconstructed III-V surfaces*. PhD thesis, Imperial College of Science, London (1999)
- [47] J. Jacobsen, K. W. Jacobsen, P. Stoltze. *Nucleation of the Pt(111) reconstruction: a simulation study*. Surf. Sci. **317**, 8 (1994)
- [48] M. Kalff, P. Šmilauer, G. Comsa, T. Michely. *No coarsening in Pt(111) homoepitaxy*. Surf. Sci. **426**, L447 (1999)
- [49] J. Kertész, D. E. Wolf. *Noise reduction in Eden models: II. Surface structure and intrinsic width*. J. Phys. A: Math. Gen. **21**, 747 (1988)
- [50] M. Kinne. *Computersimulationen von epitaktischen Wachstumsprozessen: Ein einfaches Modell*. Diplomarbeit, Universität Würzburg (1999)

- [51] W. Kinzel, M. Schick. *Extent of exponent variation in a hard-square lattice gas with second-neighbor repulsion*. Phys. Rev. B **24**, 324 (1981)
- [52] W. Kinzel, W. Selke, K. Binder. *Phase transitions on centred rectangular lattice gases: A model for the adsorption of H on Fe(110)* Surf. Sci. **121**, 13 (1982)
- [53] D. E. Knuth. *The Art of Computer Programming*. 2d ed. Addison-Wesley, Reading, Massachusetts (1981)
- [54] P. Kratzer, C. G. Morgan, M. Scheffler. *Model for nucleation in GaAs homoepitaxy derived from first principles*. Phys. Rev. B **59** (23), 15246 (1999)
- [55] P. Kratzer, E. Penev, M. Scheffler. *First-principles studies of kinetics in epitaxial growth of III-V semiconductors*. Preprint, cond-mat/0105430
- [56] P. Kratzer, M. Scheffler. *Reaction-Limited Island Nucleation in Molecular Beam Epitaxy of Compound Semiconductors*. Phys. Rev. Lett. **88** (3), 036102 (2002)
- [57] J. Krug. *Turbulent interfaces*. Phys. Rev. Lett. **72** (18) 2907 (1994)
- [58] J. Krug, M. Schimschak. *Metastability of Step Flow Growth in 1+1 Dimensions*. J. Phys. I (France) **5**, 1065 (1995)
- [59] V. P. LaBella, D. W. Bullock, M. Anser, Z. Ding, C. Emery, L. Bellaiche, P. M. Thibado. *Microscopic View of a Two-Dimensional Lattice-Gas Ising System within the Grand Canonical Ensemble*. Phys. Rev. Lett. **84** (18), 4152 (2000)
- [60] J. M. López. *Scaling Approach to Calculate Critical Exponents in Anomalous Surface Roughening*. Phys. Rev. Lett. **83** (22) 4594 (1999)
- [61] J. M. López, private communication.
- [62] J. M. López, M. A. Rodríguez. *Lack of self-affinity and anomalous roughening in growth processes*. Phys. Rev. E **54** (3) R2189 (1996)
- [63] J. M. López, M. A. Rodríguez, R. Cuerno. *Super-roughening versus intrinsic anomalous scaling of surfaces*. Phys. Rev. E **56** (4) 3993 (1997)
- [64] P. A. Maksym. *Fast Monte Carlo simulation of MBE growth*. Semicond. Sci. Technol. **3**, 594 (1988)
- [65] S. Mallat, W. L. Hwang. *Singularity Detection and Processing with Wavelets*. IEEE Transactions on Information Theory **38** (2), 617 (1992)
- [66] S. Mallat, S. Zhong. *Characterization of Signals from Multiscale Edges*. IEEE Transactions on Pattern Analysis and Machine Intelligence, **14** (7), 710 (1992)
- [67] D. Martrou, J. Eymery, P. Gentile, N. Magnea. *Epitaxial growth of CdTe(001) studied by scanning tunneling microscopy*. Journ. Cryst. Growth **184/185**, 203 (1998)
- [68] D. Martrou, J. Eymery, N. Magnea. *Equilibrium Shape of Steps and Islands on Polar II-VI Semiconductors Surfaces*. Phys. Rev. Lett. **83** (12), 2366 (1999)

- [69] D. Moldovan, L. Golubovic. *Interfacial coarsening dynamics in epitaxial growth with slope selection*. Phys. Rev. E **61** (6), 6190 (2000)
- [70] F. Much. *Strukturbildung in der Heteroepitaxie*. Diplomarbeit, Universität Würzburg (2000)
- [71] F. Much, M. Ahr, M. Biehl, W. Kinzel. *Kinetic Monte Carlo simulations of dislocations in heteroepitaxial growth*. Europhys. Lett. **56** (6), 791 (2001)
- [72] J. F. Muzy, E. Bacry, A. Arnéodo. *Multifractal formalism for fractal signals: The structure-function approach versus the wavelet-transform modulus-maxima method*. Phys. Rev. E **47** (2) 875, (1993)
- [73] H. Neureiter, S. Schinzer, W. Kinzel, S. Tatarenko, M. Sokolowski. *Simultaneous layer-by-layer and step-flow sublimation on the CdTe(001) surface derived from a diffraction analysis*. Phys. Rev. B **61** (8), 5408 (2000)
- [74] H. Neureiter. *Struktur und Kinetik polarer II-VI-Halbleiteroberflächen: Experimentelle Untersuchungen an CdTe(001)*. PhD thesis, Universität Würzburg (1998)
- [75] H. Neureiter, S. Tatarenko, S. Spranger, M. Sokolowski. *Domain wall formation at the $c(2 \times 2)$ - (2×1) phase transition of the CdTe(001) surface*. Phys. Rev. B. **62** (4), 2542 (2000)
- [76] M. E. J. Newman, G. T. Barkema. *Monte Carlo Methods in Statistical Physics*. Clarendon Press, Oxford (1999)
- [77] P. Nightingale. *Finite-size scaling and phenomenological renormalization*. J. Appl. Phys. **53** (11), 7927 (1982)
- [78] M. P. Nightingale. *Phenomenological Renormalization Group Theory*. PhD Thesis, University of Amsterdam (1978)
- [79] C. H. Park, D. J. Chadi. *First-principles study of the atomic reconstructions of ZnSe(100) surfaces*. Phys. Rev. B **49**, 16467 (1994)
- [80] M. D. Pashley. *Electron counting model and its application to island structures on molecular-beam epitaxy grown GaAs(001) and ZnSe(001)*. Phys. Rev. B **40**, 10481 (1989)
- [81] P. Peyla, A. Pimpinelli, J. Cibert, S. Tatarenko. *Deposition and growth with desorption for CdTe molecular beam epitaxy*. Journ. Cryst. Growth **184/185**, 75 (1998)
- [82] A. Pimpinelli, J. Villain. *Physics of Crystal Growth*. Cambridge University Press, Cambridge (1998)
- [83] A. Pimpinelli, J. Villain. *What does an evaporating surface look like?* Physica A **204**, 521 (1994)
- [84] M. Plischke, M. Siegert, J. Krug. *Surface diffusion currents and the universality classes of growth*. Phys. Rev. Lett. **70** (21), 3271 (1993)
- [85] P. Politi. *Different Regimes in the Ehrlich-Schwoebel Instability*. J. Phys. I France **7**, 797 (1997)

- [86] P. Politi, G. Grenet, A. Marty, A. Ponchet, J. Villain. *Instabilities in crystal growth by atomic or molecular beams*. Phys. Rep. **324**, 271 (2000)
- [87] P. Politi, J. Villain. *Ehrlich-Schwoebel instability in molecular-beam epitaxy: A minimal model*. Phys. Rev. B **54** (7), 5114 (1996)
- [88] V. Pontikis. *Thermally Activated Processes in Solids*. in A. L. Laskar (ed.) *Diffusion in Materials*, Kluwer (1990)
- [89] V. Privman, M. E. Fisher. *Finite-Size Effects at First-Order Transitions*. Journ. Stat. Phys. **33** (2), 385 (1983)
- [90] V. Privman, L. S. Schulman. *Analytic Continuation at First-Order Phase Transitions*. Journ. Stat. Phys. **29** (2), 205 (1982)
- [91] J. J. Ramasco, J. M. López, M. A. Rodriguez. *Generic Dynamic Scaling in Kinetic Roughening*. Phys. Rev. Lett. **84** (10), 2199 (2000)
- [92] F. Reif. *Statistische Physik und Theorie der Wärme*. de Gruyter, Berlin, New York (1987)
- [93] P. A. Rikvold, W. Kinzel, J. D. Gunton, K. Kaski. *Finite-size-scaling study of a two-dimensional lattice-gas model with a tricritical point*. Phys. Rev. B **28** (5), 2686 (1983)
- [94] A. Rockett. *The influence of surface structure on growth of Si(001) 2×1 from the vapor phase*. Surf. Sci. **227**, 208 (1990)
- [95] M. Rost, J. Krug. *Coarsening of Surface Structures in Unstable Epitaxial Growth*. Phys. Rev. E **55** (4), 3952 (1997)
- [96] S. G. Roux, A. Arnéodo, N. Decoster. *A Wavelet based method for multifractal image analysis. III. Application to high-resolution satellite images of cloud structure*. Eur. Phys. J. B **15** (4), 765 (2000)
- [97] M. A. Salmi, M. Alatalo, T. Ala-Nissila, R. M. Nieminen. *Energetics and diffusion paths of gallium and arsenic adatoms on flat and stepped GaAs(001) surfaces*. Surf. Sci. **425**, 31 (1999)
- [98] M. Schick. in *Phase Transitions in Surface Films*. by J. G. Dash and J. Ruvalds (eds.) Plenum Press, New York (1980)
- [99] A. Schindler. *Theoretical aspects of growth on one and two dimensional strained crystal surfaces*. PhD thesis, Gerhard-Mercator-Universität Duisburg (1999)
- [100] S. Schinzer. *Kinetic Monte-Carlo Simulations of Crystal Surfaces: Applications to II-VI Semiconductors*. PhD thesis, Universität Würzburg (1999)
- [101] S. Schinzer, M. Kinne, M. Biehl, W. Kinzel. *The role of step edge diffusion in epitaxial crystal growth*. Surf. Sci. **439**, 191 (1999)
- [102] S. Schinzer, W. Kinzel. *Modeling sublimation by computer simulation: morphology-dependent effective energies*. Surf. Sci. **401** (1), 96 (1998)

- [103] S. Schinzer, S. Köhler, G. Reents. *Ehrlich-Schwoebel barrier controlled slope selection in epitaxial growth*. Eur. Phys. J. B **15**, 161 (2000)
- [104] S. Schinzer, M. Sokolowski, M. Biehl, W. Kinzel. *Unconventional MBE strategies from computer simulations for optimized growth conditions*. Phys. Rev. B **60**, 2893 (1999)
- [105] M. Schroeder. *Fractals, Chaos, Power Laws: Minutes from an Infinite Paradise*. Freeman, New York (1990)
- [106] R. L. Schwoebel. *Step Motion on Crystal Surfaces. II*. Journ. Appl. Phys. **40** (2), 614 (1969)
- [107] R. L. Schwoebel, E. J. Shipsey. *Step Motion on Crystal Surfaces*. Journ. Appl. Phys. **37** (10), 3682 (1966)
- [108] L. Seehover, G. Falkenberg, R. L. Johnson, V. H. Etgens, S. Tatarenko, D. Brun, B. Daudin. *Scanning tunneling microscopy study of CdTe(001)*. Appl. Phys. Lett. **67** (12), 1680 (1995)
- [109] W. Selke, K. Binder, W. Kinzel. *Lattice gas models with competing interactions*. Surf. Sci. **125**, 74 (1983)
- [110] M. Siegert. *Coarsening Dynamics of Crystalline Thin Films*. Phys. Rev. Lett. **81** (25), 5481 (1998)
- [111] M. Siegert, M. Plischke, R. K. P. Zia. *Contrasts between coarsening and relaxational dynamics of surfaces*. Phys. Rev. Lett. **78** (19), 3705 (1997)
- [112] J. Singh, K. K. Bajaj. *Theoretical studies of the intrinsic quality of GaAs/AlGaAs interfaces grown by MBE: Role of kinetic processes*. J. Vac. Sci. Technol. B **3** (2), 520 (1985)
- [113] J. Singh, A. Madhukar. *Prediction of Kinetically Controlled Surface Roughening: A Monte Carlo Computer-Simulation Study*. Phys. Rev. Lett. **51** (9), 794 (1983)
- [114] J. Stoer, R. Bulirsch. *Introduction to numerical analysis*. Springer-Verlag, New York (1993)
- [115] R. Stumpf, M. Scheffler. *Theory of Self-Diffusion at and Growth of Al(111)*. Phys. Rev. Lett. **72** (2), 254 (1994)
- [116] I. Suemune, A. Ishibashi (eds.). *Proceedings of the Ninth International Conference on II-VI Compounds, Kyoto 1999*. J. Cryst. Growth **214-215** (2000)
- [117] L.-H. Tang. *Unstable Growth and Coarsening in Molecular-Beam Epitaxy*. Physica A **254**, 135 (1998)
- [118] L.-H. Tang, P. Šmilauer, D. D. Vvedensky. *Noise-assisted mound coarsening in epitaxial growth*. Eur. J. Phys. B **2**, 409 (1998)
- [119] S. Tatarenko, B. Daudin, D. Brun, V. H. Etgens, M. B. Veron. *Cd and Te desorption from (001), (111)B, and (110) CdTe surfaces*. Phys. Rev. B **50** (24), 18479 (1994)

- [120] J. M. Thijssen. *Computational Physics*. Cambridge University Press, Cambridge (1999)
- [121] J. C. Van Den Berg. *Wavelets in Physics*. Cambridge University Press, Cambridge (1999)
- [122] J. A. Venables, G. D. T. Spiller, M. Hanbücken. *Nucleation and growth of thin films*. Rep. Prog. Phys. **47**, 399 (1984)
- [123] M. B. Veron, A. Arnoult, B. Daudin, S. Tatarenko. *Reversibility of the elementary mechanisms of atomic-layer epitaxy and sublimation of (001) CdTe*. Phys. Rev. B **54** (8), R5267 (1996)
- [124] J. Villain, A. Pimpinelli, L. Tang, D. Wolf. *Terrace sizes in molecular beam epitaxy*. J. Phys. I (France) **2**, 2107 (1992)
- [125] T. Vicsek. *Fractal Growth Phenomena*. World Scientific, Singapore (1992)
- [126] T. Volkmann. *Anisotropie-Effekte an Halbleiteroberflächen*. Diplomarbeit, Universität Würzburg (2000)
- [127] J. Wang, A. Rockett. *Simulating diffusion on Si(001) 2×1 surfaces using a modified interatomic potential*. Phys. Rev. B **43** (15), 12571 (1991)
- [128] D. E. Wolf. *Computer simulation of molecular beam epitaxy*. In M. Droz, A. J. McKane, J. Vannimenus, D. E. Wolf (eds.) *Scale Invariance, Interfaces, and Non-Equilibrium Dynamics*. NATO-ASI Series, Plenum Press, New York (1994)
- [129] D. Wolframm, D. A. Evans, D.I. Westwood, J. Riley. *A detailed surface phase diagram for ZnSe MBE growth and ZnSe/GaAs(001) interface studies*. Journ. Cryst. Growth **216**, 119 (2000)
- [130] Y. Yue, Y. K. Ho, Z. Y. Pan. *Molecular-dynamics study of transient-diffusion mechanisms in low-temperature epitaxial growth*. Phys. Rev. B **57** (11), 6685 (1998)

Danksagung

Ich möchte allen, die zum Gelingen dieser Arbeit beigetragen haben, herzlich danken, insbesondere

- Dr. Michael Biehl, der diese Arbeit betreut hat und sich immer Zeit nahm, auf meine Fragen einzugehen und über meine Ideen zu diskutieren.
- Prof. Dr. Wolfgang Kinzel, an dessen Lehrstuhl ich diese Arbeit anfertigen durfte.
- Dr. Michael Biehl, Martin Kinne, Prof. Dr. Wolfgang Kinzel, Florian Much, Dr. Stefan Schinzer, Prof. Dr. Moritz Sokolowski und Thorsten Volkmann für die fruchtbare Zusammenarbeit, deren Ergebnisse wir gemeinsam veröffentlicht haben.
- Prof. Dr. Joachim Krug und seiner Arbeitsgruppe für die Gastfreundschaft an der Universität Essen.
- Florian Much und Thorsten Volkmann für das gründliche Korrekturlesen dieser Arbeit.
- Ansgar Freking und allen anderen Systembetreuern für den guten Zustand unserer Computer.
- allen Mitgliedern unserer Arbeitsgruppe für das freundliche und kreative Arbeitsklima.
- der Deutschen Forschungsgemeinschaft, die diese Arbeit finanziert hat.